BULETINUL INSTITUTULUI POLITEHNIC DIN IAŞI

Tomul LVI (LX)

Fasc. 4

ŞTIINȚA ŞI INGINERIA MATERIALELOR

2010 **Editura POLITEHNIUM**

BULETINUL INSTITUTULUI POLITEHNIC DIN IAŞI
PUBLISHED BY
„GHEORGHE ASACHI" TECHNICAL UNIVERSITY OF IAŞI
Editorial Office: Bd. D. Mangeron 63, 700050, Iaşi, ROMANIA
Tel. 40-232-278683; Fax: 40-232 237666; e-mail: polytech@mail.tuiasi.ro

Editorial Board

President : Prof.dr.eng. **Ion Giurma**, Member of the Academy of Agricultural Sciences and Forest, *Rector* of the "Gheorghe Asachi" Technical University" of Iaşi

Editor-in -Chief : Prof.dr.eng. **Carmen Teodosiu**, *Vice-Rector* of the "Gheorghe Asachi" Technical University of Iaşi

Honorary Editors of the Bulletin: Prof.dr.eng. **Alfred Braier**
Prof.dr.eng. **Hugo Rosman**
Prof.dr.eng. **Mihail Voicu**, Corresponding Member of the Romanian Academy, *President* of the "Gheorghe Asachi" Technical University of Iaşi

Editors in Chief of the **MATERIALS SCIENCE AND ENGINEERING** ***Section***
Assoc. prof. dr. eng. **Iulian Ioniță**
Assoc. prof. dr. eng. **Gheorghe Bădărău**
Prof. dr. eng. **Petrică Vizureanu**

Honorary Editors: Prof. dr. eng. **Dan Gelu Găluşcă**
Prof. dr. eng. **Adrian Dima**

Associated Editor: Assoc. prof. dr. eng. **Ioan Rusu**

Editorial Advisory Board

Prof.dr.eng. **Agustin Santana Lopez,** La Palmas de Gran Canaria University (Spain)

Prof.dr.eng. **Julia Mirza Rosca**, La Palmas de Gran Canaria University (Spain)

Prof.dr.eng. **Roy Buchan**, Colorado State University (U.S.A.)

Prof.dr.eng. **Yuri A. Burennikov**, Vinnitsya National Technical University (Ukraine)

Prof.dr.hab. **Zbigniew Gronostajski**, Technical University of Wroclaw (Poland)

Prof. dr. **Oronzio Manca**, Seconda Università degli Studi di Napoli (Italy)

Assoc. prof. **Shizutoshi Ando**, Tokyo University of Sciences (Japan)

Dr. **Koichi Tsuchiya**, National Institute for Materials Science (Japan)

Dr.eng. **Burak Özkal**, Istanbul Technical University (Turkey)

Prof. dr. eng. **Vasile Cojocaru-Filipiuc**, "Gheorghe Asachi" Technical University of Iaşi (Romania)

Prof. dr. eng. **Constantin Baciu**, "Gheorghe Asachi" Technical University of Iaşi (Romania)

Prof. dr. **Viorel Păun**, University "Politehnica" Bucharest (Romania)

BULETINUL INSTITUTULUI POLITEHNIC DIN IAŞI
BULLETIN OF THE POLYTECHNIC INSTITUTE OF IAŞI
Tomul LVI (LX), Fasc. 4 2010

ŞTIINŢA ŞI INGINERIA MATERIALELOR

SUMAR

Pag.

ANCA ALUCULESEI, CONSTANTIN BACIU, MARICEL AGOP şi ALINA ALUCULESEI, Caracterizarea unei structuri magnetice: zeolit nanoporos cu carbon (engl. rez. rom.). 9

RAMONA HANU CIMPOEŞU, CONSTANTIN BACIU şi MARICEL AGOP, Conductivitate termică colectivă la scală mesoscopică (engl. rez. rom.). . 17

ALINA COSTAN, O conexiune între fenomenul de transport şi dimensiuni spaţiu-timp (engl. rez. rom.) 25

BOGDAN LUCIAN GAVRILĂ, MIHAI SUSAN, ELENA CHIRILĂ, DRAGOŞ CRISTIAN ACHIŢEI şi BRIAN-TUDOR LANDKAMER, Poziţionarea reflectoarelor de energie ultrasonică la tragerea metalelor în câmp ultrasonor (engl. rez. rom.). 35

BRIAN-TUDOR LANDKAMMER, CONSTANTIN BACIU, MIHAI SUSAN şi BOGDAN LUCIAN GAVRILĂ, Construcţia şi dimensionarea elementelor sistemului oscilator utilizat în operaţiile de finisare şi durificare cu ultrasunete (engl. rez. rom.). 45

ANCA ELENA LĂRGEANU, Straturi subţiri obţinute prin metoda PLD (engl. rez. rom.) 51

RÂZVAN IULIAN LIŢOIU, Transferul de căldură la scară mesoscopică (engl. rez. rom.) 61

BOGDAN PRICOP, NICOLETA MONICA LOHA şi LEANDRU-GHEORGHE BUJOREANU, Efectele ciclării termice într-un aliaj Cu-Zn-Al cu memoria formei (engl. rez. rom.). 65

ŞTEFAN RUSU şi DAN GELU GĂLUŞCA, Marcarea laser a materialelor I. Principii şi procese (engl. rez. rom.). 71

ŞTEFAN RUSU şi IOAN RUSU, Marcarea laser a materialelor. II. Tehnologii şi aplicatii (engl. rez. rom.) 85

ANDREI VICTOR SANDU şi COSTICĂ BEJINARIU, Noi straturi fosfatate pe suport de fier cu proprietăţi lubrifiante (engl. rez. rom.) 97

BULETINUL INSTITUTULUI POLITEHNIC DIN IAŞI
BULLETIN OF THE POLYTECHNIC INSTITUTE OF IAŞI
Tomul LVI (LX), Fasc. 4 2010

MATERIALS SCIENCE AND ENGINEERING

CONTENTS

Pp.

ANCA ALUCULESEI, CONSTANTIN BACIU, MARICEL AGOP and ALINA ALUCULESEI, Characterisation of Magnetic Structure-Nanoporus Zeolite Templated Carbon (English, Romanian summary) 9

RAMONA HANU CIMPOEŞU, CONSTANTIN BACIU and MARICEL AGOP, Collective Thermal Conductivity at Mesoscopic Scale (English, Romanian summary). 17

ALINA COSTAN, A Connection Between the Transport Phenomena and the Fractal Space-Time (English, Romanian summary). 25

BOGDAN LUCIAN GAVRILĂ, MIHAI SUSAN, ELENA CHIRILĂ, DRAGOS CRISTIAN ACHIŢEI and BRIAN-TUDOR LANDKAMER, About the Positioning of the Ultrasonic Energy Reflectors at the Metals Drawing in Ultrasound Field (English, Romanian summary) 35

BRIAN-TUDOR LANDKAMMER, CONSTANTIN BACIU, MIHAI SUSAN and BOGDAN LUCIAN GAVRILĂ, Construction and Dimensioning Elements of the Oscillator System Used in the Hardening and Finishing Operations in Ultrasound Field (English, Romanian summary) 45

ANCA ELENA LĂRGEANU, Thin Layers Obtain by PLD Method (English, Romanian summary). 51

RĂZVAN IULIAN LIŢOIU, On the Heat Transfer at Mesoscopic Scale (English, Romanian Summary). 61

BOGDAN PRICOP, NICOLETA MONICA LOHAN and LEANDRU-GHEORGHE BUJOREANU, Thermal Cycling Effects In Cu-Zn-Al Shape Memory Alloys (English, Romanian summary). 65

ŞTEFAN RUSU and DAN-GELU GĂLUŞCĂ, Laser Marking of Materials: Principles and Processes (English, Romanian summary). 71

ŞTEFAN RUSU and IOAN RUSU, Laser Technology for Applications In Marking (English, Romanian summary). 85

ANDREI VICTOR SANDU and COSTICĂ BEJINARIU, New Phosphated Layers on Iron Support With Lubricant Properties (English, Romanian summary) 97

BULETINUL INSTITUTULUI POLITEHNIC DIN IAŞI
Publicat de
Universitatea Tehnică „Gheorghe Asachi" din Iaşi
Tomul LVI (LX), Fasc. 4, 2010
Secţia
ŞTIINŢA ŞI INGINERIA MATERIALELOR

CHARACTERISATION OF MAGNETIC STRUCTURE-NANOPORUS ZEOLITE TEMPLATED CARBON

BY

ANCA ALUCULESEI, CONSTANTIN BACIU, MARICEL AGOP and *ALINA ALUCULESEI

Abstract. The effects of heat-treatment and guest adsorption on the structure and electronic/magnetic properties were investigated for zeolite template carbon (ZTC) by using potassium, bromine, and helium as guest species. ZTC consists of a curved graphene network, wich has regularly arranged nanopores with a periodicity of 1.4nm. X-ray diffraction and Raman spectra reveal that the regular nanopore structure is preserved during vacuum heat-treatment(<380 ^{0}C) and potassium adsorption process. On the other hand, bromine adsorption is found to destroy the nanopore structure.

Key words: nanostructures, vapor deposition, X-ray diffraction.

1. Introduction

Nanoporous systems have attracted much interest as host materials in view of materials designing with the employement of nanospace in creating unconventional electronic and magnetic structures, wich cannot be build from bulk systems. Among these, nanographene-based nanoporous carbon such as activated carbon fibers (ACFs) is a unique host, since magnetic nonbonding π-state (edge-state) participates in the interaction. Actually, the adsorption of helium, wich is the most inert chemical species results in the significant enhancement in the spin-lattice relaxation of the of the edge-state spins in ACFs without charge transfer interaction. Here, the presence of the ultramicropore in ACFs, to with only smallest-diameter helium molecules can have access, plays an important role. Moreover, the nanospace in ACFs works as reaction pot in creating magnetic postassium clusters, which are

magnetically interacting with the edge-state spins of nanographene host with charge transfer interaction being ineffective. Here, the disordered structure of ACFs is unfortunately disadvantageous in stabilizing the magnetism of the potassium cluster, whereas the regular nanospace structure allows us to desing intentionally the nano-architecture of the guest materials accommodated in the nanospace and their functions. Then, it is natural to reach the idea that template material with a regularly arrayed nanospace can be utilized to create grapheme-based regular nanospace arrangement, which hosts guest materials in a desirable manner. Zeolite has been one of the most important template materials with regularly arranged nanospace in template-based material designing. Zeolite template carbon (ZTC) is prepared by transcribing the regular nanospace structure of zeolite using CVD. Here, the demerit caused by the disorder appearing in ACFs can be overcome [3].

ZTC has a three-dimensional (3D) network of graphene sheet forming a periodic surface with negative curvatures. The structure is described roughly as a 3D array of fullerene-like cages connected with each other by carbon nanotube channels, where the cage and the channel correspond to the super-cage and the channel part of the zeolite template, respectively. The presence of pentagons and higher polygons such as heptagon embedded in the hexagonal p-electron network is responsible curvature at connecting parts between a cage and a channel, respectively, in the ZTC graphene network. In the magnetism point of view, the graphene network of ZTC with negative curvature gives another interesting feature. Recent spin density functional calculations for the tetrapod motif, which is considered as the fundamental unit of ZTC with zeolite Y template, indicate the presence of radical spins at the saddle part having a negatively curved graphene surface. This magnetic behavior originates from undercoordinated carbon atoms, which are introduced as a part of higher polygons into the aromatic system of hexagons. It is sterically stabilized by the p-orbitals of the surrounding sp2 carbon atoms, which extend over the undercoordinated site in the saddle parts of graphene tetrapod motif. According to the calculation results, the spin polarization spreads over the whole tetrapod to a large extent.

This implies the significant overlap between the wavefunctions of the radicals at the adjacent negative curvature sites [5].

Meanwhile, a recent experimental study suggests ferromag-netic behavior for ZTC prepared by the furfuryl alcohol-CVD. However, the experimental details such as pre-treatment condition and the correlation between the magnetism and structure are not well understood there. In order to extract the intrinsic magnetism of the ZTC itself, and also ZTC-based host-guest system, we should care about the characterizations of the host material such as the structural change by heat-treatment and guest adsorption or the effect of the adsorption of the atmospheric gases during the measurement, and so on.

In this study, the structure and electronic/magnetic properties of ZTC were investigated in terms of heat-treatment effect and for the positive curvature at cage parts, and negative guest adsorption effect through the measurement of X-ray diffraction (XRD), Raman spectroscopy, and electron spin resonance (ESR). As guest materials, three guests are examined: potassium, bromine, and helium, which are typically used as guest material for donor, acceptor, and thermal exchanger for low temperature measurement, respectively [2].

2. Experimental

Acetylene CVD with zeolite Y as a template and subsequent dissolution of the template by acid were applied for the fabrication of ZTC, where the nanospace network composed of curved graphene sheet with a periodicity of 1.4 nm was formed [1]. Prior to the guest adsorption and electronic/magnetic properties measurements, the ZTC sample was evacuated to 1 x10~6Torr at room temperature and 380-780°C for 10 h in order to remove contaminants adsorbed in the nanopores, and then it was vacuum-sealed in a Pyrex glass tube. Hereafter, the as-prepared sample and the samples pre-heat-treated at XXX°C are denoted as non-HT and HTTXXX, respectively. Guest adsorption was performed by using HTT380, which was referred as ‘‘non-adsorbed ZTC’’ with respect to the guest adsorbed ZTC. Potassium and bromine were absorbed by vapor transfer method in Pyrex tubes. CuKa source was used for XRD. Raman spectroscopy measurements were performed using Jobin-Yvon T64000 instruments with an argon-ion laser operated at 514.5 nm. ESR spectra were measured with an ESR X-band spectrometer (JEOL JES-TE200).

3. Results and Discussion

In the ambient condition, the ZTC sample contains a large concentration of foreign chemical species, which modify significantly its magnetic properties because of its huge specific surface area. Thus, such chemical species should be removed from the sample prior to measurements by degassing them at high temperature in vacuum. However, there is a possibility that the heat-treatment in vacuum at high temperature damages the structure of ZTC. Guest adsorption process is also harmful for the host ZTC structure. In order to investigate the details of the host-guest interaction, careful evaluation of the stability of the host material structure is an important requisite. Thus, the stability of pre-treated and guest adsorbed ZTC sample was investigated by means of structural analysis at first. Then, its magnetism was investigated next.

Structure

The XRD profiles commonly exhibit a sharp peak around 6°. It is worth to mention that there is no peak around 25° for all the samples, at which the strong (0 0 2) peak assigned to the stacking periodicity of graphene layers appears in graphite. The sharp peaks around 6° appearing in the XRD profiles for the non-HT and HTT380 correspond the presence of the periodic structure with the periodicity of 1.4 nm, which is inherited to the structure of the zeolite Y template. This evidences that the periodic structure of arrayed nanopores is preserved even by the heat-treatment up to 380°C in ZTC. The presence of curved graphene structure in ZTC is proved by Raman spectra. The Raman spectra for the guest adsorbed ZTC samples are summarized in Fig. 2 with those for non-HT, ZTC380 and ZTC780. As typically observed in graphitic materials, the G-band for bending sp2-bonded carbons and D-band for breathing aromatic rings are observed. The features of the G- and D-band peaks are almost the same to each other irrespective of the heat-treatment for non-HT and HTT380, with the G (D) peak position of 1610 cm-1 (1354 cm^{-1}) and the G (D) peak line width of 27 cm^{-1} (80 cm^{-1}). On the other hand, the line shape of HTT780 is obviously different from that of the others, where the G (D) peak position and the G (D) peak line width are 1596 cm^{-1}, (1340 cm^{-1}) and 37 cm-1, (75 cm^{-1}), respectively, around 1600 and 1350 cm^{-1} for all the ZTC samples, respectively.

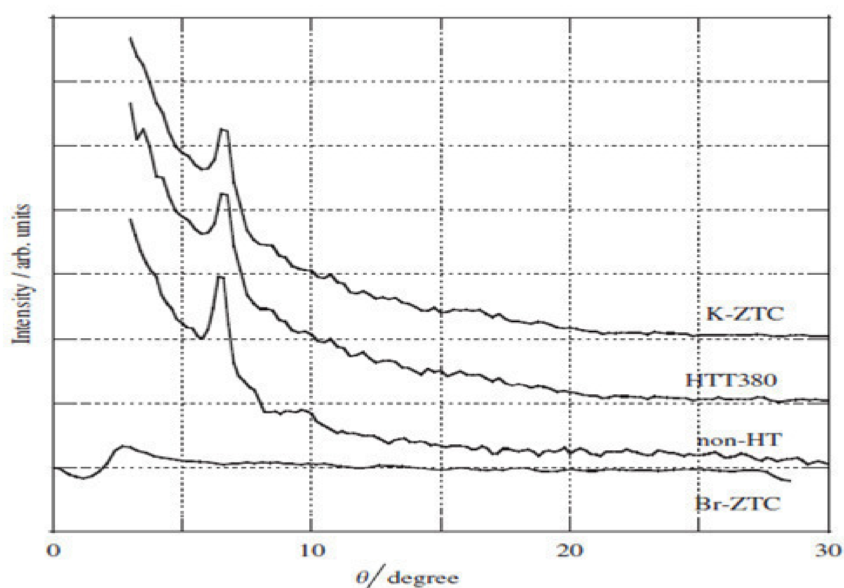

Fig. 1 – XRD profiles for the vacuum heat- treated and the guest adsorbed ZTCs.

These findings suggest a significant upshift of the G-band for non-HT and HTT380 ZTCs from that of graphene (1582 cm^{-1}). Recent theoretical study reveals the hardening of the G-mode for single walled nanotube (SWNT), when the graphene structure is curved along the zigzag direction through the enhancement of the electron-phonon coupling. Thus, the observed upshift of G-band for HTT380 and non-HT indicates the presence of the curved graphene sheet in the ZTC structure. In contrast, the line shape for HTT780 is obviously different from those for HTT380 and non-HT. The increase in the line width and downshift of the G-peak position of HTT780 from HTT380 indicate the destruction of the ZTC curved graphene backbone. Indeed, the G-band peak position for HTT780 is much closer to that of graphite, suggesting that the curved graphene structure relaxes into a flat graphene structure, which is thermodynamically stable. Namely, it is found that the periodic nanopore array and the curved graphene nature in the ZTC structure are preserved during the heat-treatment only up to 380°C [7].

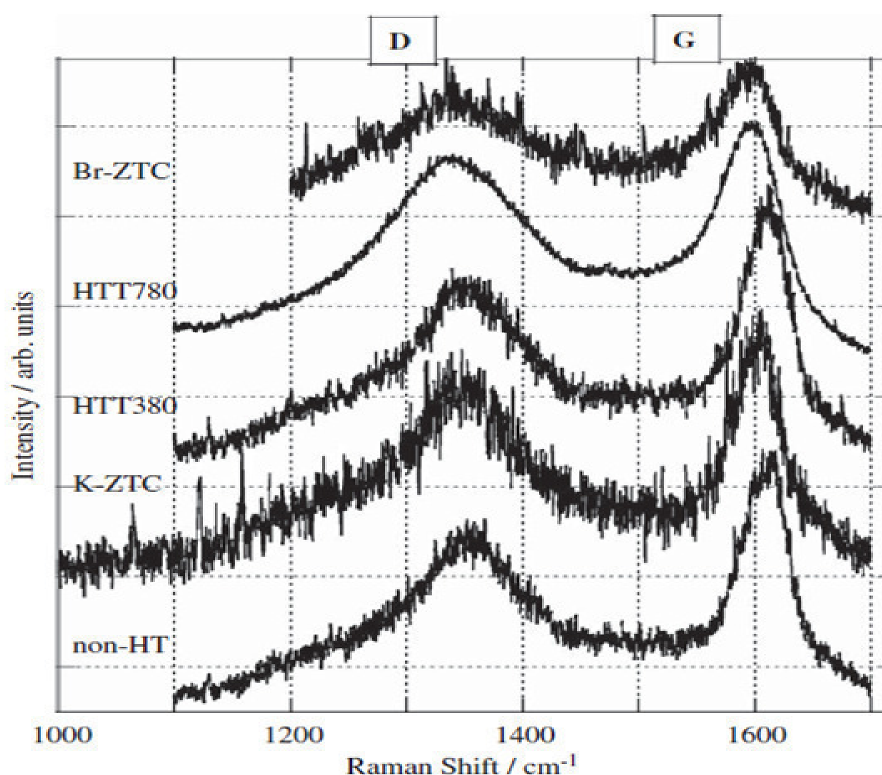

Fig. 2 – Raman spectra for the vacuum heat-treated and guest adsorbed ZTCs.

Next the effect of the guest adsorption on the ZTC structure is discussed. As shown in Fig. 1, the peak around 6° corresponding to 3D

nanopore network of ZTC is preserved during the potassium adsorption. Taking the strong electron-donating nature of potassium into consideration, the downshift of the G-band is reasonable. Usually in the Next, the effect of the guest adsorption on the ZTC structure is discussed. As shown in Fig. 1, the peak around 6° corresponding to the 3D nanopore network of ZTC is preserved during potassium adsorption process. The Raman spectrum for K-ZTC shown in Fig. 2 also resembles that for the HTT380 in its line shape except for the downshift in the G-band peak (1601 cm^{-1}). The resembled line shape of the Raman spectrum for the K-ZTC suggests that the ZTC backbone structure does not collapse during potassium adsorption process. This is also evidenced by XRD results, where the peak graphene structure, the G-band position is related to the 7i-band filling through strong electron-phonon coupling, where electrons (holes) partially occupying the bottom (top) of the anti-bonding 7i*- (bonding n-) band cause softening (hardening) of the C-C bonds. Empirically, the doping-induced peak shift A of the G-band position (k/cm^{-1}) in graphene is related to the charge transfer rate fc per carbon atom from graphene to guest species by the following relation:
–1.63 x 10~6zl2=0.157/c+0.146/c/ 2+0.236/2. From the above relation with A = =1601–1610, charge transfer rate for K-ZTC is estimated as /c= ~1x10~3. The obtained charge transfer rate is found to be two orders magnitude smaller than that for graphite intercalation compounds (fc=0.075 for KC8), where potassium guests are accommodated in the gallery of the stacked graphene sheets. Taking it in consideration that the arrayed nanopore structure of ZTC is formed by single curved graphene without stacking, potassium atoms in K–ZTC are physisorbed in the nanopore formed by curved graphene wall as potassium nanocluster. This is justified by the extremely smaller charge transfer rate even in the adsorption of potassium having strong donor activity. In view of the electronic structure, the curved nature of the ZTC graphene network also explains the extremely small charge transfer rate between the potassium guest and host ZTC. The presence of the curvature in the graphene network causes the mixing of sp3 character with the n-electron system, resulting in lowering the density of states or the presence of a gap at the Fermi energy in the host electronic structure. This is much disadvantage for the charge transfer interaction. Here, it should be noted that the line width of G-band for K-ZTC is reduced with respect to that for HTT380. In general, the broad–ening of the G-band line width appears in the electron doped systems because of the random potential introduced by dopants. Meanwhile, it is known that the G-band shift induced by charge transfer in the curved graphene is accompanied with the line width narrowing. Thus, the reduction in the line width for K-ZTC proves that the downshift of the G-band does neither the collapse of the curved graphene structure nor the random potential by the dopant.

In contrast with K-ZTC, the ZTC structure is drastically modified in the case of bromine adsorption. The Raman spectrum for the Br-ZTC is modified

from that for HTT380, or rather it resembles that for HTT780, where the ZTC backbone structure is destroyed. Especially, the downshift of the G-band position (1593 cm^{-1}), which contradicts the usual trend of upshift for acceptor dopants, suggests that the curved graphene network of ZTC is completely destroyed. The harmful effect of bromine on the ZTC structure appears more obviously in the XRD results. As shown in Fig. 1, the peak corresponding to the arrayed nanopore structure completely vanishes, although the peak around 6° is confirmed for the non-adsorbed ZTC before bromine adsorption. This is a common feature with the XRD results for the HTT780, where the ZTC backbone structure is decomposed and relaxed into flat graphene flakes. Consequently, both vacuum degassing up to 380°C and potassium adsorption are surely safe for the ZTC structure.

Received: August 31, 2010

"Gheorghe Asachi" Technical University of Iaşi,
**Instituto Superior Tecnico, Faculty of Physics Lisboa, Portugal*
e-mail: aluculesei_anca@yahoo.com

R E F E R E N C E S

1. Maxwell J.C., *A Treatise on Electricity and Magnetism.* 3rd Ed., **1**, Dover, New York, 435, 1954.
2. El Naschie M.S., Rosier O.E., Prigogine I. (Eds.), *Quantum Mechanics, Diffusion and Chaotic Fractals*. Elsevier, Oxford, 1991.
3. Cresson J., Int. J. of Geometric Meth. In Mod. Phys., *3*, 1395 (2006).
4. Cresson J., J. Math. Anal. AppL, *307*, 48 (2005).
5. Mandelbrot B.B., *The Fractal Geometry of Nature.* W.H. Freeman, San Francisco 1983.
6. Farhat H., Son H., Samsonidze Ge.G., Reich S., Dresselhaus M.S., Kong J., Phys. Rev. Lett., 99 (2007).
7. Mackay A.L., Terrones H., *Nature.* 352 (1991).
8. Ddresselhaus M.S., Dresselhaus G., Eklund P.C., *Science of Fullerences and Carbon Nanotubes*. Acad. Press, San Diego, 1996.
9. Enoki T., Suzuki M., Endo M., *Graphite Intercalation Compounds and Applications*. Oxford Univ. Press, New York, 2003.

CARACTERIZAREA UNEI STRUCTURI MAGNETICE: ZEOLIT NANOPOROS CU CARBON

(Rezumat)

Un zeolit şablonat de carbon (ZTC) cu matricea aliniată regulat a structurilor nanoporoase este cercetat în vedere structurii şi magnetismului, şi efectul său de adsorbţie guest. Structura ZTC este păstrată în timpul atât tratamentului termic în vid

de până la 3800°C şi adsorbției de potasiu, în ciuda efectului distructiv de adsorbție a bromului. Magnetismului ZTC este sensibil la adsorbție guest, în cazul în care chiar şi adsorbția gazului inert heliu afectează semnificativ procesul spin – de relaxare.

BULETINUL INSTITUTULUI POLITEHNIC DIN IAŞI
Publicat de
Universitatea Tehnică „Gheorghe Asachi” din Iaşi
Tomul LVI (LX), Fasc. 4, 2010
Secţia
ŞTIINŢA ŞI INGINERIA MATERIALELOR

COLLECTIVE THERMAL CONDUCTIVITY AT MESOSCOPIC SCALE

BY

RAMONA HANU CIMPOEŞU, CONSTANTIN BACIU and MARICEL AGOP

Abstract. Using a nonlinear equation for thermal transfer at mesoscopic scale two conduction regimes are distinguished: non- autonomous regime and the quasi-autonomous one. This two regimes are separated by a 0.7 structure. Moreover, the collective behavior of the thermal conductivity is established.

Key words: thermal transfer, conduction regimes.

1. Introduction

In a recent paper [1] we show that the thermal transfer at mesoscopic scale is given by the equation

$$\frac{\hat{\partial}\mathbf{V}}{\partial t} = \frac{\partial \mathbf{V}}{\partial t} + \mathbf{V}.\nabla\mathbf{V} + \frac{\hbar^2}{4cm^2}\nabla^3\mathbf{V} = 0 \tag{1}$$

where **V** is a complex speed field, $\hbar$ is the reduced Plank`s constant, c the speed of light on the vacuum, m is the rest mass of the test particle and ∇^3 the operator

$$\nabla^3 = \frac{\partial^3}{\partial X^3} + \frac{\partial^3}{\partial Y^3} + \frac{\partial^3}{\partial Z^3} \tag{2}$$

with X, Y, Z the fractal spatial coordinates [2].

In the present paper using the equation (1) for the complex speed field and a connection between the speed and temperature fields the thermal conductivity at mesoscopic scale is analyzed.

2. Mathematic Model

Let us consider the complex speed field in the form:

$$\boldsymbol{V} = \boldsymbol{v} + i\boldsymbol{u} \tag{3}$$

According to [3], [4], $\boldsymbol{v}$ will correspond to the classical speed given by the differential part of $\boldsymbol{V}$, and $\boldsymbol{u}$ will correspond to the fractal speed given by the non-differential part of $\boldsymbol{V}$. By replacing (3) in Eq. (1) and separating the real part from the imaginary one, we obtain the following system:

$$\begin{aligned} &\frac{\partial \boldsymbol{v}}{\partial \boldsymbol{t}} + \boldsymbol{v}\nabla\boldsymbol{v} - \boldsymbol{u}\nabla\boldsymbol{u} + \frac{h^2}{4cm^2}\nabla^3\boldsymbol{v} = \boldsymbol{0} \\ &\frac{\partial \boldsymbol{u}}{\partial \boldsymbol{t}} + \boldsymbol{v}\nabla\boldsymbol{u} + \boldsymbol{u}\nabla\boldsymbol{v} + \frac{h^2}{4cm^2}\nabla^3\boldsymbol{u} = \boldsymbol{0} \end{aligned} \tag{4a,b}$$

In the differentiable case, *i.e.* $\boldsymbol{u} = 0$, the system (4*a*, *b*) becomes:

$$\frac{\partial \boldsymbol{v}}{\partial \boldsymbol{t}} + \boldsymbol{v}\nabla\boldsymbol{v} + \frac{h^2}{4cm^2}\nabla^3\boldsymbol{v} = \boldsymbol{0} \tag{5}$$

Considering that the heat transfer process at mesoscopic scale is one-dimensional, Eq. (5) takes the standard form of the KdV equation [1], [2]:

$$\frac{\partial v}{\partial t} + v\frac{\partial v}{\partial x} + \frac{\hbar^2}{4cm^2}\frac{\partial^3 v}{\partial x^3} = 0 \tag{6}$$

Using the dimensionless parameters $\phi = (v / v_0) = \sqrt{T/T_0}$, $\tau = \omega_0 t$, $\xi = k_0 x$ and the normalizing conditions [5] $k_0 v_0 = \hbar^2 k_0^3 / 4cm^2 = 6\omega_0$, Eq. (6) becomes:

$$\partial_\tau \phi + 6\phi\partial_\xi \phi + \partial_{\xi\xi\xi}\phi = 0 \tag{7}$$

where T/T_0 defines the normalized temperature field.

Through the substitutions $w(\theta)=\phi(\xi,\tau),\ \ \theta=\xi\text{-}u\tau$, where (ω_0,k_0,v_0) are parameters characterizing the critical temperature field at mesoscopic scale [1],…,[3], the Eq. (7), by double integration, becomes:

$$\frac{1}{2}\left(\frac{dw}{d\theta}\right)^2=F(w)=-(w^3-\frac{u}{2}w^2-gw-h) \tag{8}$$

with g, h two integration constants. If $F(w)$ has real roots, they are of the form [6]

$$e_3=2a\left[\frac{E(s)}{K(s)}-\frac{1}{s^2}\right] \tag{9a,c}$$

with

$$a=\frac{e_1-e_2}{2},\ s^2=\frac{e_1-e_2}{e_1-e_3},\ K(s)=\int_0^{\pi/2}(1-s^2\sin^2\varphi)^{-1/2}d\varphi$$

$$E(s)=\int_0^{\pi/2}(1-s^2\sin^2\varphi)^{1/2}d\varphi \tag{10a-d}$$

and where $K(s)$ and $E(s)$ are the complete elliptic integrals [6]. Then, the solution of Eq. (7) has the expression

$$\begin{aligned}\varphi(\xi,\tau)&=2a\left(\frac{E(s)}{K(s)}-1\right)+\\&+2acn^2\left\{\sqrt{a}s^{-1}\left[\xi-2a\left(\frac{3E(s)}{K(s)}-\frac{1+s^2}{s^2}\right)\tau+\xi_0\right];s\right\}\end{aligned} \tag{11}$$

where cn is the Jacobi's elliptic function of s modulus [6] and ξ_0 constant of integration. As a result, the heat transfer at mesoscopic scale is achieved by one-dimensional cnoidal oscillation modes of the normalized temperature field. This process is characterized through the normalized wave length,

$$\lambda_1=\frac{2sK(s)}{\sqrt{a}} \tag{12}$$

- see Fig. 1,

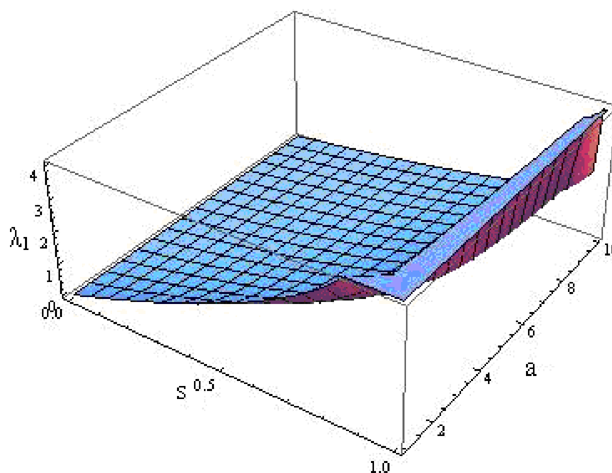

Fig. 1 – The dependence of the normalized wave length λ_1 with s and a.

and through the normalized phase speed,

$$u_1 = 4a\left[3\frac{E(s)}{K(s)} - \frac{1+s^2}{s^2}\right] \quad (13)$$

- see Fig 2.

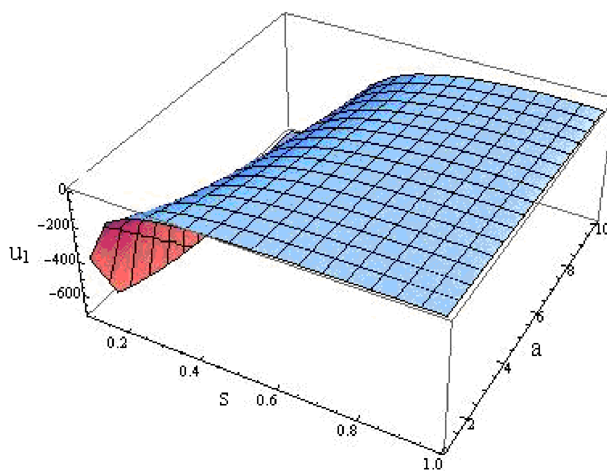

Fig. 2 – The dependence of the normalized phase speed u_1 with s and a.

In such a conjecture, it results that:

i) By eliminating the parameter *a* from relations (12) and (13), one obtains the dispersion relation:

$$u_1 = k_1^2 A(s) \tag{14}$$

with

$$k_1 = \frac{2\pi}{\lambda_1},\ A(s) = \frac{4}{\pi^2}\left[3s^2 E(s)K(s) - (1+s^2)K^2(s)\right] \tag{15}$$

The quantity A(s) is numerically evaluated. Thus, for $s = 0 \div 0.7$, $A(s) \approx$ const. – see Fig. 3,

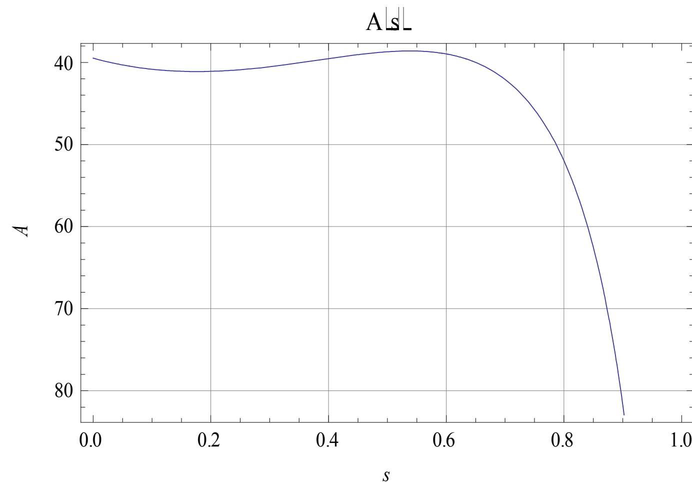

Fig. 3 – The dependence $A = A(s)$.

and the Eq. (14) takes the form,

$$u_1 = const. \cdot k_1^2 \tag{16}$$

ii) Through the $\hbar/2m$ scale coefficient [2-4], the parameter s becomes a measure of the heat transfer at mesoscopic scale. Thus, for a decrease of the heat transfer, *i.e.* $s \to 0$, the normalized speed (u_1) and the normalized wave length (λ_1) are small – see Figs 1 and 2, while, for an increase of the heat transfer, *i.e.* $s \to 1$, u_1 and λ_1 are high – see Figs. 1 and 2.

iii) the one-dimensional cnoidal temperature oscillation modes contain as subsequences for $s=0$ the one-dimensional temperature harmonic waves and for $s \to 0$ the one-dimensional temperature waves packet. These subsequences describe the heat transfer at mesoscopic scale in a non-autonomous regime [5], [6]. For $s=1$, the solution (11), with the substitutions $\phi_0 = e_3$ and $k^2 = (e_1 - e_3)/2$, becomes the one-dimensional normalized temperature soliton

$$\phi(\xi,\tau) = \phi_0 + 2k^2 \sec h^2\left[k\left(\xi - \left(4k^2 + 3\phi_0\right)\tau + \xi_0\right)\right] \tag{17}$$

of amplitude $2k^2$, width k^{-1} and phase velocity $u = 4k^2 + 3\phi_0$, while for $s \to 1$ we obtain the one dimensional normalized temperature solitons packet. These subsequences describe the heat transfer at mesoscopic scale in a quasi-autonomous regime.

Therefore, these two conduction regimes (non-autonomous and quasi-autonomous, respectively) are separated by the 0.7 structure, a value according to [7].

3. Conclusions

The main conclusions of the present paper are the following:

i) through the scale relativity theory in the fractal dimension $D_F = 3$, in the differentiable case the heat transport at mesoscopic scale is achieved by cnoidal oscillation modes of the normalized temperature field (see the expression of the heat "current");

ii) for different degrees of the heat transfer at mesoscopic scale, the one-dimensional cnoidal normalized temperature oscillation modes contain the one-dimensional normalized temperature harmonic waves, the one-dimensional temperature waves packet, the one dimensional normalized temperature solitons packet and the one dimensional normalized temperature soliton. The first two subsequences describe the heat transfer at mesoscopic scale in the non-autonomous regime, while the last two ones describe the heat transfer at mesoscopic scale in the quasi-autonomous regime;

iii) a dispersion relation is also obtained;

iv) non-autonomous regime and autonomous regime are separated by a 0.7 structure, a result in accordance with [7].

Received: September 1, 2010

"Gheorghe Asachi"Technical University of Iaşi,
e-mail: ramonahanu@yahoo.com

R E F E R E N C E S

1. Gottlieb I., Agop M., Ciobanu G., Stroe A., *El Naschie's E-infinity Space-Time and New Results in Scale Relativity Theories.* Chaos Solitons & Fractals **30**, 380-398 (2006).
2. Buzea C.Gh., Agop M., Găluşcă G., Vizureanu P., Ioniță I., *El Naschie's Superconductivity in the Time Dependent Ginzburg -Landau Model*. Chaos Solitons & Fractals, CHAOS 03122, 1-15 (2006).
3. Agop M., Ioannou P.D., Nica P., Găluşcă G., Ştefan M., *El Naschie's Coherence on the Subquantum Medium*. Chaos Soliton & Fractals, **23**, *5*, 1497-1509 (2005).
4. Gottlieb I., Agop M., Buzdugan M., Craciun P., *El Naschie's Cantorian Frames, Gravitation and Quantum Mechanics.* Chaos Soliton & Fractals, **24**, 391-405 (2005).
5. Gurlui S., Agop M., Strat M., Strat G., Bacaita S., *Experimental and Theoretical Investigations of Anode Double Layer.* Jpn. J. Appl. Phys., **44**, *5A*, 15-21 (2005).
6. Agop M., Alexandroaie D., Cerepaniuc A., Bacaita S., *El Naschie's E-Infinity Space-Time and Patterns in Plasma Discharge.* Chaos Solitons & Fractals, **30**, 470-489 (2006).
7. Stan C., Cristescu C.P., Agop M., *Golden Mean Relevance for Chaos Inhibition in a System of two Coupled Modified van der Pol Oscillators*. Chaos Solitons & Fractals, **31**, *4*, 1035-1040 (2007).

CONDUCTIVITATE TERMICĂ COLECTIVĂ LA SCALA MESOSCOPICĂ

(Rezumat)

Folosind o ecuație nonlineară pentru transferul termic la scala mesoscopică sunt distinse două regimuri de curgere: regimul dependent şi cel semiautonom. Aceste două regimuri sunt separate de o structură în proporție de 0,7. Mai mult este stabilit şi comportarea colectivă a conductivității termice.

BULETINUL INSTITUTULUI POLITEHNIC DIN IAŞI
Publicat de
Universitatea Tehnică „Gheorghe Asachi” din Iaşi
Tomul LVI (LX), Fasc. 4, 2010
Secţia
ŞTIINŢA ŞI INGINERIA MATERIALELOR

A CONECTION BETWEEN THE TRANSPORT PHENOMENA AND THE FRACTAL SPACE-TIME

BY

ALINA COSTAN

Abstract. Using a nonlinear equation for transport phenomena at mesoscopic scale, a possible connection with a fractal space-time manifold is established.

Key words: fractal space-time, transport phenomena.

1. Introduction

The scale relativity theory (SRT) [1],…,[5] “is a new approach to understand quantum mechanics, and moreover physical domains involving scale laws, such as chaotic systems. It is based on a generalization of Einstein’s principle of relativity to scale transformations. Namely, one redefines space-time resolutions as characterizing the state of scale of reference systems, in the same way as velocity characterizes their state of motion. Then one requires that the laws of physics apply whatever the state of the reference system, of motion (principle of motion-relativity) and of scale (principle of scale-relativity). The principle of scale-relativity is mathematically achieved by the principle of scale-covariance, requiring that the equations of physics keep their simplest form under transformations of resolution”. In such conjecture, considering that the motion of micro-particles take place on continuous but non-differentiable curves (fractal curves), it was demonstrated that, in the topological dimension [6] D_T=2, the geodesics of the space-time are given by a Schrödinger’s type equation.

In the present paper we obtain a connection between a nonlinear equation for transport phenomena at mesoscopic scale in non-relativistic approach and non-differentiable space-time.

2. Mathematical Model

In the weak-field approach (WFA) of the relativistic nonlinear transport phenomena (RNTP) at mesoscopic scale, the connection between the geometry and dynamics of the microparticles is given by the equation [7]

$$\Box\psi - \frac{1}{6}R\psi - \frac{1}{3}\Lambda\left|\psi\right|^2\psi = 0 \tag{1}$$

where R and Λ are two constants and ψ is simultaneously a scalar field and wave function.

For more details (the WKA method, the physical significations of R, Λ constants and ψ variable etc.) see reference [7]. In such a conjecture, equation (1) with $\psi = Ae^{(iS/\hbar)}$ becomes

$$\begin{gathered}\partial_\nu\left(A^2\partial_\nu S\right) = 0\\ \partial_\nu S\partial_\nu S + \frac{\hbar^2}{6}\left(R + 2\Lambda A^2\right) - \hbar^2\left(\frac{\Box A}{A}\right) = 0,\ \nu = \overline{1,4}\end{gathered} \tag{2a, b}$$

with A and S the amplitude and the phase of the wave function, respectively, and $\hbar$ the reduced Planck's constant.

The correspondence with the non-relativistic hydrodynamic model is accomplished for $S = S' - m_0c^2t$, where S' is the classical action and m_0 the rest mass of the test particle. It results:

$$\begin{gathered}\partial_t\left(m_0A^2\right) + \nabla\left(A^2\nabla S'\right) = 0\\ 2m_0\partial_t S' + \left(\nabla S'\right)^2 - m_0^2c^2 + \frac{\hbar^2}{6}\left(R + 2\Lambda A^2\right) - \hbar^2\left(\Delta A/A\right) = 0\end{gathered} \tag{3a, b}$$

or, through the speed fields

$$\boldsymbol{v} = m_0^{-1}\nabla S';\quad \boldsymbol{u} = -\left(\hbar/2m_0\right)\nabla\ln\rho,\quad \rho = A^2 \tag{4a-c}$$

and the application of ∇ operator to equation (3*b*),

$$m_0(\partial_t\boldsymbol{v} + \boldsymbol{v}\cdot\nabla\boldsymbol{v}) = -\nabla(U + Q),\ \ \partial_t\rho + \nabla\cdot\left(\rho\boldsymbol{v}\right) = 0 \tag{5a, b}$$

with

(6*a*-*c*)
$$U = \frac{\Lambda\hbar^2}{6m_0}\rho + U_0, U_0 = \frac{1}{2m_0}\left(\frac{R\hbar^2}{6} - m_0^2c^2\right) = const.;$$
$$Q = -\frac{\hbar^2}{2m_0}\frac{\Delta\rho^{1/2}}{\rho^{1/2}} = -\left(h/2m_0\right)\nabla\cdot\mathrm{u} - \left(m_0\mathrm{u}^2/2\right)$$

The following conclusions can now be drawn: i) Any particle is in a permanent interaction with the 'subquantum level' through the quantum potential Q; ii) The 'subquantum level' is identified with a non-relativistic quantum fluid (non-relativistic fluid) described by the hydrodynamic equations (5*a*, *b*); iii) The quantum potential depends only by the imaginary part of the complex velocity,

$$\boldsymbol{V} = -\frac{i\hbar}{m_0}\nabla(\ln\psi) = \boldsymbol{v} + i\boldsymbol{u}. \tag{7}$$

iv) The wave function of $\psi(\mathbf{r}, t)$ is invariant when its phase changes by an integer multiple of 2π. Indeed, equation (4*a*) gives:

$$\oint m_0\boldsymbol{v}d\boldsymbol{r} = \oint dS' = \hbar\oint ds' = nh, \quad n = 1, 2, ... \tag{8}$$

a condition of compatibility between the non-relativistic hydrodynamic model and the wave mechanics (WM); v) On the vacuum states, *i.e.* for the quantum numbers $n = 1$, $l = m = 0$, the state density is [8]

$$\rho(r) = \frac{1}{\pi r_0^3}e^{-\frac{2r}{r_0}} \tag{9}$$

Substituting (9) in the quantum potential expression (6*c*), *i.e.*

$$Q(r) = -\frac{\hbar^2}{2m_0\sqrt{\rho}}\left(\frac{d^2\sqrt{\rho}}{dr^2} + \frac{2}{r}\frac{d\sqrt{\rho}}{dr}\right) = -\frac{\hbar^2}{2m_0r_0}\left(\frac{1}{r_0} - \frac{2}{r}\right), \tag{10}$$

we obtain the attractive force,

$$F(r) = -\frac{\partial Q}{\partial r} = -\frac{\hbar^2}{m_0r_0}\frac{1}{r^2} \tag{11}$$

This result is according to opinion given in [9].

3. The Connection with the Fractal Space-Time

According to [1],...,[6] and our (5*a*, *b*) and (7) relations, it results a possible connection with the motions of microparticles on continuous but non-differentiable curves i.e. on fractals. Indeed, let $P\left(x^1, x^2\right)$ be a point of the fractal curve and let us consider a line which starts from this point and let *Q* be the first intersection of this line with the fractal curve. We denote by $x^1 + dX^1$, $x^2 + dX^2$ the coordinates of *Q*, thus ***PQ*** is a vector of components dX^1, dX^2. We denote by dX_+^i the components of the vector ***PQ*** for which $dX^1 > 0$, hence they are at the right of the line (d) and by dX_-^i the case when $dX^1 < 0$, such as is the case for the vector ***PQ'*** – see Fig. 1. Considering all the lines (segments) which start from *P*, we denote the average of these vectors by $dx_\pm^i$ *i.e.*

(12) $$\left\langle dX_\pm^i \right\rangle = dx_\pm^i \qquad \left(i = 1, 2\right).$$

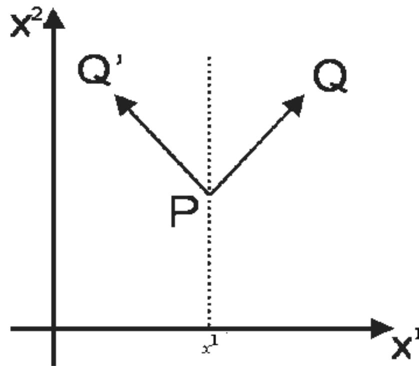

Fig. 1 – The continuous curves which are not fractals but have points where they are not differentiable.

Therefore we can write

(13) $$dX_\pm^i = dx_\pm^i + d\xi_\pm^i,$$

where

(14) $$\left\langle d\xi_\pm^i \right\rangle = 0.$$

Details on the average process are given in [4]. Here $dx_{\pm}^{i}$ are the left and right differentials of the classical variables, and $d\xi_{\pm}^{i}$ describe the fractal characteristic. From (13) we obtain the speed field:

$$\frac{d\boldsymbol{X}_{\pm}}{dt}=\frac{d\boldsymbol{x}_{\pm}}{dt}+\frac{d\boldsymbol{\xi}_{\pm}}{dt} \tag{15}$$

We denoted by $(d\boldsymbol{x}_{+}/dt)=\boldsymbol{v}_{+}$ the "forward" speed and by $(d\boldsymbol{x}_{-}/dt)=\boldsymbol{v}_{-}$ the "backward" speed.

We have no way to favor $\boldsymbol{v}_{+}$ rather than $\boldsymbol{v}_{-}$. Both choices are equally qualified for the description of the laws on nature. The only solution to this problem is to consider both the forward ($dt>0$) and backward ($dt<0$) processes together. So, we can introduce the complex speed [1],…,[6]:

$$\boldsymbol{V}=\frac{\boldsymbol{v}_{+}+\boldsymbol{v}_{-}}{2}-i\frac{\boldsymbol{v}_{+}-\boldsymbol{v}_{-}}{2}=\frac{d\boldsymbol{x}_{+}+d\boldsymbol{x}_{-}}{2dt}-i\frac{d\boldsymbol{x}_{+}-d\boldsymbol{x}_{-}}{2dt} \tag{16}$$

where $(\boldsymbol{v}_{+}+\boldsymbol{v}_{-})/2$ may be considered as classical speed, the difference between them, *i.e.* $(\boldsymbol{v}_{+}-\boldsymbol{v}_{-})/2$ is the fractal speed.

Let us assume now that the fractal curve is immersed in a 3-dimensional space, and $\boldsymbol{X}$ of components X^{i} (i=$\overline{1,3}$) is the position vector of a point on the curve. Let us consider also a function $f(X,t)$ and the following Taylor series expansion up to the second order:

$$\begin{aligned} df=f(X^{i}+dX^{i},t+dt)-f(X^{i},dt)=\left(\frac{\partial}{\partial X^{i}}dX^{i}+\frac{\partial}{\partial t}dt\right)f(X^{i},t)+\\ +\frac{1}{2}\left(\frac{\partial}{\partial X^{i}}dX^{i}+\frac{\partial}{\partial t}dt\right)^{2}f(X^{i},t). \end{aligned} \tag{17}$$

From here, the forward and backward average values of this relation using notations $dX_{\pm}{}^{i}=d_{\pm}X^{i}$ take the form (for details on the method see [4], [5]):

$$\begin{aligned} \langle d_{\pm}f\rangle=\left\langle\frac{\partial f}{\partial t}dt\right\rangle+\langle\nabla f\cdot d_{\pm}\mathrm{X}\rangle+\frac{1}{2}\left\langle\frac{\partial^{2}f}{\partial t^{2}}(dt)^{2}\right\rangle+\left\langle\frac{\partial^{2}f}{\partial X^{i}\partial t}d_{\pm}X^{i}dt\right\rangle+\\ +\frac{1}{2}\left\langle\frac{\partial^{2}f}{\partial X^{i}\partial X^{l}}d_{\pm}X^{i}d_{\pm}X^{l}\right\rangle \end{aligned} \tag{18}$$

We make the following stipulations: the mean values of the function f and its derivates coincide with themselves, and the differentials $d_{\pm}X^i$ and dt are independent, therefore the averages of their products coincide with the product of average (for other details see [4], [5]). Then (18) becomes:

$$d_{\pm}f = \frac{\partial f}{\partial t}dt + \nabla f\left\langle d_{\pm}\mathrm{X}\right\rangle + \frac{1}{2}\frac{\partial^2 f}{\partial t^2}\left\langle (dt)^2\right\rangle + \frac{\partial^2 f}{\partial X^i \partial t}\left\langle d_{\pm}X^i dt\right\rangle + \\ + \frac{1}{2}\frac{\partial^2 f}{\partial X^i \partial X^l}\left\langle d_{\pm}X^i d_{\pm}X^l\right\rangle \tag{19}$$

or, using (13) in the form (12)

$$d_{\pm}f = \frac{\partial f}{\partial t}dt + \nabla f d_{\pm}\mathrm{x} + \frac{1}{2}\frac{\partial^2 f}{\partial t^2}(dt)^2 + \frac{\partial^2 f}{\partial X^i \partial t}d_{\pm}x^i dt + \\ + \frac{1}{2}\frac{\partial^2 f}{\partial X^i \partial X^l}\left(d_{\pm}x^i d_{\pm}x^l + \left\langle d\xi_{\pm}^i d\xi_{\pm}^l\right\rangle\right) \tag{20}$$

Since $d\xi_{\pm}^i$ describes the non-differentiability of the curve trajectory with the topological dimension D_T (for details see [6]), it is natural to impose $(d\xi_{\pm}^i)^{D_T}$ to be proportional with dt, *i.e.*

$$(d\xi_{\pm}^i)^{D_T} = \frac{\hbar}{m_0}dt \tag{21}$$

Let us focus now on the mean $\left\langle d\xi_{\pm}^i d\xi_{\pm}^l\right\rangle$. If $i \neq l$ this average is zero due the independence of $d\xi^i$ and $d\xi^l$. So, using (21) we can write:

$$\left\langle d\xi_{\pm}^i d\xi_{\pm}^l\right\rangle = \delta^{il}\left(\frac{\hbar}{m_0}dt\right)^{2/D_F} \tag{22}$$

with

$$\delta^{il} = \begin{cases} 1, & if \quad i = l \\ 0, & if \quad i \neq l \end{cases}$$

Through of a Peano type curves, which covers a two-dimensional surface, *i.e.* $D_T \to 2$, (22) becomes:

(23)
$$\left\langle d\xi_{\pm}^{i} d\xi_{\pm}^{l} \right\rangle = \pm \frac{\hbar \delta^{il}}{m_0} dt$$

where we had considered that:

$$\begin{cases} \left\langle d\xi_{+}^{i} d\xi_{+}^{l} \right\rangle > 0 \ and \ dt > 0 \\ \left\langle d\xi_{-}^{i} d\xi_{-}^{l} \right\rangle > 0 \ and \ dt < 0 \end{cases}$$

Then (20) may be written under the form:

(24)
$$d_{\pm} f = \frac{\partial f}{\partial t} dt + \nabla f d_{\pm}\mathrm{x} + \frac{1}{2}\frac{\partial^2 f}{\partial t^2}(dt)^2 + \frac{\partial^2 f}{\partial X^i \partial t} d_{\pm}x^i dt + \frac{1}{2}\frac{\partial^2 f}{\partial X^i \partial X^l} d_{\pm}x^i d_{\pm}x^l + \\ + \frac{1}{2}\frac{\partial^2 f}{\partial X^i \partial X^l}\delta^{il}\frac{\hbar}{m_0}dt$$

If we divide by dt and neglect the terms which contain differential factors (for details on the method see [4], [5]), (24) is reduced to:

(25)
$$\frac{d_{\pm} f}{dt} = \frac{\partial f}{\partial t} + \mathbf{v}_{\pm}\nabla f_{\pm} \pm \frac{\hbar}{2m_0}\Delta f$$

Let us calculate, under the circumstances *($\delta f/dt$)*. Taking into account (25), we have:

(26)
$$\frac{\delta f}{dt} = \frac{1}{2}\left[\frac{d_+ f}{dt} + \frac{d_- f}{dt} - i\left(\frac{d_+ f}{dt} - \frac{d_- f}{dt}\right)\right] = \\ = \frac{1}{2}\left(\frac{\partial f}{\partial t} + \mathrm{v}_+\nabla f + \frac{\hbar}{2m_0}\Delta f\right) + \frac{1}{2}\left(\frac{\partial f}{\partial t} + \mathrm{v}_-\nabla f - \frac{\hbar}{2m_0}\Delta f\right) - \\ - \frac{i}{2}\left[\left(\frac{\partial f}{\partial t} + \mathrm{v}_+\nabla f + \frac{\hbar}{2m_0}\Delta f\right) - \left(\frac{\partial f}{\partial t} + \mathrm{v}_-\nabla f - \frac{\hbar}{2m_0}\Delta f\right)\right] = \\ = \frac{\partial f}{\partial t} + \left(\frac{\mathrm{v}_+ + \mathrm{v}_-}{2} - i\frac{\mathrm{v}_+ - \mathrm{v}_-}{2}\right)\nabla f - i\frac{\hbar}{2m_0}\Delta f$$

or using (16):

(27*a*, *b*)
$$\frac{\delta f}{dt}=\frac{\partial f}{\partial t}+\boldsymbol{V}\cdot\nabla f-i\frac{\hbar}{2m_0}\Delta f\ ,$$

This relation also allows us to give the definition of the fractal operator:

(28)
$$\frac{\delta}{dt}=\frac{\partial}{\partial t}+\boldsymbol{V}\cdot\nabla-i\frac{\hbar}{2m_0}\Delta$$

We now apply the principle of scale covariance, and postulate that the passage from classical (differentiable) mechanics to the non-differentiable mechanics that is considered here can be implemented by replacing the standard time derivative *d/dt* by the new complex operator δ/dt (for details see [4], [5]). As a consequence, we are now able to write the Newton's equation in its covariant form:

(29)
$$\frac{\delta \boldsymbol{V}}{dt}=\frac{\partial \boldsymbol{V}}{\partial t}+\boldsymbol{V}\cdot\nabla\boldsymbol{V}-i\frac{\hbar}{2m_0}\Delta\boldsymbol{V}=-\nabla\left(\frac{U}{m_0}\right)$$

where U is given by the relation (6*a*, *b*). In a special topology, $\Lambda=0$ a generalized **Navier**-Stokes type equation having the imaginary viscosity coefficient $\eta=i\hbar/2m_0$ is obtained.

If the motion of microparticles is irrotational, *i.e.* $\boldsymbol{\Omega}=\nabla\times\boldsymbol{V}=0$ we can choose $\boldsymbol{V}$ of the form (7), so that the Eq. (29) becomes:

(30)
$$\frac{\delta \boldsymbol{V}}{dt}=\frac{\partial \boldsymbol{V}}{\partial t}+\nabla\left(\frac{\boldsymbol{V}^2}{2}\right)-i\frac{\hbar}{2m_0}\Delta\boldsymbol{V}=-\nabla\left(\frac{U}{m_0}\right)$$

Substituting (7) in (30) and using the method given in [4], [5], up to an arbitrary phase factor which may be set to zero by a suitable choice of the phase of ψ, by integration, it results a nonlinear type equation in the non-differentiable space-time,

(31)
$$i\hbar\partial_t\psi=-\frac{\hbar^2}{2m_0}\Delta\psi+\frac{\Lambda\hbar^2}{6m_0}|\psi|^2\psi+\frac{1}{2m_0}\left(\frac{R\hbar^2}{6}-m_0^2c^2\right)\psi$$

In the general case, the equation (31) has the same form as a Ginzburg-

Landau type equation (for details see [7]). In a special topology, Λ=0, the equation (31) take the standard form of the Schrödinger equation for $U_0 = const.$

4. Conclusion

A non-relativistic hydrodynamic model for a nonlinear equation for the transport phenomena is given. It results:

i) any particle is in a permanent interaction with the 'subquantum level' through the quantum potential (6*c*);

ii) the 'subquantum level' is identified with a non-relativistic quantum fluid described by the hydrodynamic equations (5*a*, *b*);

iii) the quantum potential depends only by the imaginary part of the complex velocity (7);

iv) the compatibility between the non-relativistic hydrodynamic model and WM implies the quantification condition (8);

v) through the vacuum states, the attractive force (11) is generated;

vi) considering that the motions of microparticles take place on continuous but non-differentiable curves *i.e.* on fractals, a nonlinear type equation (31) for the transport phenomena is obtained. In the general case, this equation has the same form as a Ginzburg-Landau type equation and, in a special topology, the standard form of the Schrödinger equation.

Received: 30 August, 2010

"Gheorghe Asachi" Technical University of Iaşi,
Department of Material Engineering
e-mail: alina0384@yaho.com

REFERENCES

1. Nottale L., Schneider J., J. Math. Phys., **25**, 1296 (1984).
2. Ord G., J. Phys. Math. *Gen*., **16**, 1869 (1983).
3. Nottale L., Int. J. Mod. Phys., **4**, 5047, (1989).
4. Nottale L., *Fractal Space-Time and Microphysics, Towards a Theory of Scale Relativity.* World Sci., Singapore, 1992.
5. Nottale L., *Chaos, Solitons and Fractals*. **7**, 877 (1996).
6. Madelbrot B., *The Fractal Geometry of Nature.* Freeman, San Francisco, 1982.
7. Jackson E.A., *Perspectives of Non-linear Dinamics.* Cambridge Univ. Press, Cambridge, 1991.
8. Titeica S., *Quantum mechanics.* Romanian Acad. Press, Bucharest, 1984.
9. Bohm D., Phys. Rev., **85,** 166 (1951).

O CONEXIUNE ÎNTRE FENOMENUL DE TRANSPORT ŞI DIMENSIUNI SPAȚIU-TIMP

(Rezumat)

Folosind o ecuație nonliniară pentru fenomenele de trasport la scală microscopică, se obține o conexiune pozitivă cu o varietate de dimensiuni spațiu-timp.

BULETINUL INSTITUTULUI POLITEHNIC DIN IAŞI
Publicat de
Universitatea Tehnică „Gheorghe Asachi” din Iaşi
Tomul LVI (LX), Fasc. 4, 2010
Secţia
ŞTIINŢA ŞI INGINERIA MATERIALELOR

ABOUT THE POSITIONING OF THE ULTRASONIC ENERGY REFLECTORS AT THE METALS DRAWING IN ULTRASOUND FIELD

BY

BOGDAN LUCIAN GAVRILĂ, MIHAI SUSAN, ELENA CHIRILĂ, DRAGOS CRISTIAN ACHIŢEI and BRIAN-TUDOR LANDKAMER

Abstract. The positioning distances of the ultrasonic energy reflectors/presser rolls, for a higher efficiency, at the metals drawing in ultrasound field/UVD system, when the plastic deforming tool, (the die or the mould), is placed in the maximum point of the waves oscillation and it is activated along the drawing direction, will be determined considering the condition which generates a stable system of standing waves into the semi-product.

Key words: metals drawing, ultrasonic energy reflectors, stable system of standing waves, ultrasound field and technological efficiency.

1. Introduction

The technologies of the metals drawing in ultrasound field are up-to-date technologies, „ultrasonic vibration drawing/UVD”, in comparison with the classical once–TC and they are applied especially to reduce the contact friction between the metal and the tool and so, to reduce the hardening phenomenon, [1],…,[3]. Ultrasounds are a variety of elastic waves which have a frequency whose values are between 16000 Hz and 10^{10} Hz. The elastic medium area, being in a vibratory state, which is the placement of the ultrasonic waves, is called ***ultrasonic field***.

The expected effect of the ultrasonic energy action, during the plastic deformation process by drawing, will be obtained when it will use ultrasounds with high energies – ultrasonic longitudinal waves as standing waves, which have vertexes and antinodes (minimum and maximum points of

the wave oscillation – Fig. 1).

As a matter of fact, depending on the placement of the deformation focus/the drawing tool – minimum or maximum points of the waves oscillation – it will obtain a softening effect which is a effect of the metal-tool contact friction reducing, this effect being called “the ultrasounds surface effect”, because it takes place at the interface between the metal and the tool, [1], [2], [4], [6], [7].

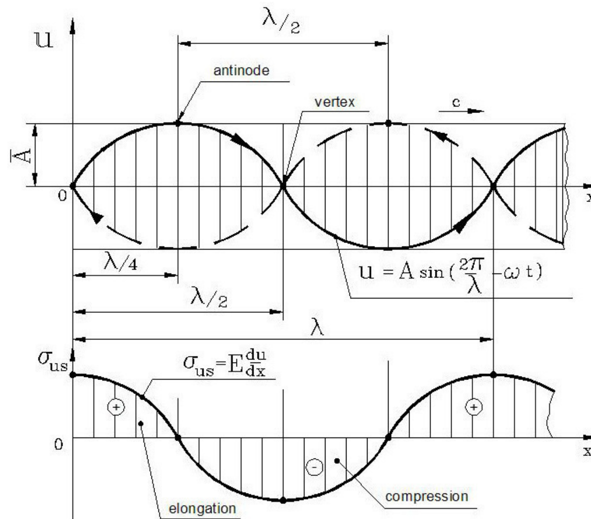

Fig. 1 – Standing waves system, [2]: *a* – waves motion (u)/sinusoidal variation; *b* – variation of the co sinusoidal ultrasonic stress (σ_{us}): *c* – ultrasounds wave velocity; λ – wavelength ($\lambda = c / f$, *f* – resonant frequency); $\overline{A}$ - oscillation amplitude of the wave / maximum value: ——— running wave; ------regressive wave.

The ultrasonic softening effect, obtained when the deforming focus is placed in the vertex of the wave oscillation, is explained considering the mechanism of the stresses overlapping, (over the static drawing stress is overlapped the ultrasonic stress) [2], [3].

The ultrasonic stress is determined using the relation (1):

$$\sigma_{us} = \frac{2\pi}{\lambda} \cdot E \cdot A , \tag{1}$$

where: λ – wavelength; A - oscillation amplitude of the wave; E – longitudinal modulus.

When the plastic deforming tool, (for ex. the mould/the die), is placed in the antinode of the wave oscillation and it is activated along the drawing direction, it will obtain the ultrasounds surface effect; this means that the metal-

tool contact friction will be reduced.

The reducing coefficient of the metal-tool mean contact friction, (φ), is determined using the relation (2), [1], [2], [7]:

$$\varphi = \frac{\pi}{2} \cdot \frac{v_{tr} \dfrac{\lambda_i \cdot \cos\alpha + 1}{2\lambda_i \cdot \cos\alpha}}{\overline{v}_v}, \tag{2}$$

where: λ_i – elongation (for pass „i”); α – angular aperture of the die or of the mould; v_{tr} – rate of drawing; $\overline{v}_v$ - vibratory rate of the deforming tool, $(\overline{v}_v = 2\pi \cdot f \cdot A)$.

The reduction of the metal-tool contact friction is explained considering the SEVERDENKO model, [1].

From the practical/marketing point of view, it is very important to apply the ultrasounds surface effect in the case of the drawing technologies of the metals which have a strong hardenability by plastic cold deformation.

The technological efficiency of the metal drawing process which uses the activation of the deforming tool along the drawing direction, the so called „ultrasonic vibration drawing – UVD”, can be expressed with the relation (3):

$$\Delta F = \frac{F^{TC} - F^{UVD}}{F^{TC}} \cdot 100 \quad [\%], \tag{3}$$

Considering the GAVRILENKO relation for the force calculation in the metal drawing technologies, it will use the relation (4):

$$F^{TC} = F_d + F_f = F_d(1 + \mu \cdot ctg\alpha), \tag{4}$$

where: F_d – proper deforming force; F_f – friction force / COULOMB type friction; α – angular aperture of the die or of the mould.

Considering the process of the metals drawing in ultrasound field, the relation (4) becomes:

$$F^{UVD} = F_d\left(1 + \frac{\mu \cdot ctg\alpha}{\phi}\right) \tag{5}$$

2. Positioning of the Ultrasonic Energy Reflectors at the Metals Drawing in Ultrasound Field

Following an ultrasonic energy distribution on well defined distances, when the plastic deforming tool is activated along the drawing direction, it will

use ultrasonic energy “reflectors”, [1],…,[4]. As a matter of fact, the ultrasonic energy reflectors are presser rolls which are placed at well defined distances; these distances result considering the condition of a standing waves system generation into the drawing semi-product (Fig. 2), [1], [2].

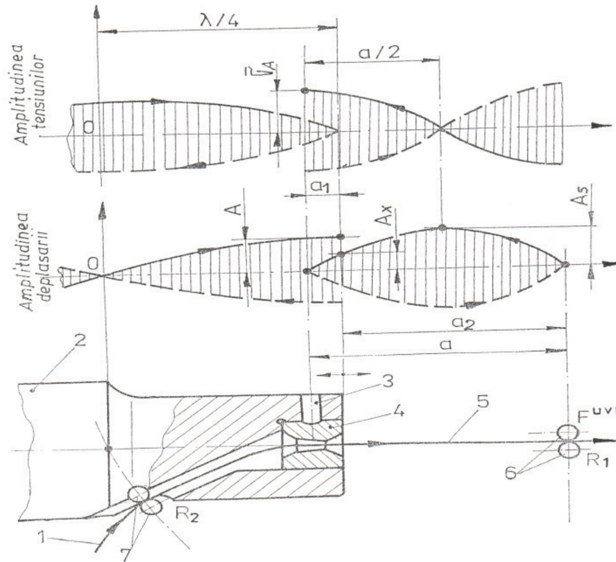

Fig. 2 – Scheme of a standing waves system generation into the drawing semi-product, [2]: 1 – semi-product; 2 – graded cylindrical concentrator; 3 – locating pin of the deforming tool; 4 – die or mould; 5 – product processed by drawing; 6, 7 – ultrasonic energy reflectors, (R_1, R_2 – presser rolls).

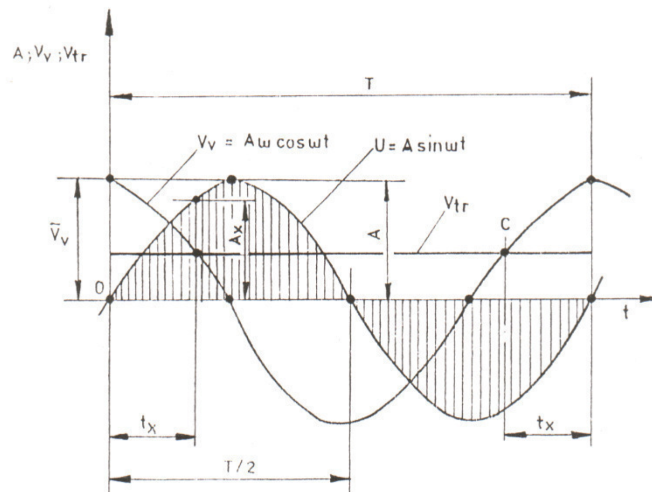

Fig. 3 – Variation of the amplitude, (A), vibratory rate, (V_v), and rate of drawing, (V_{tr}), during one complete oscillation period, [2],…,[5].

Considering the kinematics of the plastic deformation process, in the case of the UVD system processing, it will determine the positioning distances, a_1 and a_2, of the reflector R_1, (Fig. 2). The discussion begins at the moment when the vibratory rate of the die, (V_v), increases, becomes equal to the rate of drawing in point C, (V_{tr}) and goes on to increase-it takes place “the unloading” of the deforming tool from here, in the drawing processed product, to the reflector R_1, when the compression wave is propagated (Fig. 3).

This process takes place during a time whose value is given by relation (6):

$$t' = 2t_x = \frac{T}{\pi}\arccos\frac{v_{tr}}{\bar{v}_v}, \tag{6}$$

where $\left|v_{tr}/\bar{v}_v\right| \le 1.0$, to the end of the time $T/2$, when $\left|v_v\right| < v_{tr}$ and the straining wave is propagated from the reflector R_1, into the semi-product which is processed by drawing.

The reflector R_1 may be placed at a certain distance, (a_1), so that, at the beginning moment of the straining wave introducing into the semi-product, the reflected wave (the regressive wave) achieves on the frontal plane of the graded cylindrical concentrator. So, into the semi-product processed by drawing, a standing wave stable system will be generated, whose maximum oscillation amplitude will be on the frontal plane of the graded cylindrical concentrator.

The oscillation amplitude into the semi-product, (increased by the deforming tool), in the exit area, out of the deforming focus, in a plane which is normal on its axes, depends on the value of the rate of drawing, (v_{tr}), and on the oscillation amplitude of the die, as the relation (7) shows :

$$2A_x = A \cdot \sin\omega t_x - v_{tr} \cdot t'. \tag{7}$$

Introducing t’ and t_x into the relation (7), after a few operations will be obtained the relation (8):

$$A_x = A\sqrt{1-\left(\frac{v_{tr}}{\bar{v}_v}\right)} - A\frac{v_{tr}}{\bar{v}_v}\arccos\frac{v_{tr}}{\bar{v}_v} \tag{8}$$

where : $\left|v_{tr}/\bar{v}_v\right| \le 1.0$.

For the distance a_1 determining, it will consider that the semi-product belongs to the oscillator system/UVD system. If the semi-product would be

rigid tight, at the level of the drawing tool, (v_{tr} = 0), then, the oscillation amplitude, generated in its inside, would be equal to the amplitude of the die or of the mould oscillation and the reflector R_1 would be placed at the distance a_1 = λ/4, in one condition: the reflected wave (the regressive wave) must overlap on the straining wave (the induced wave). The semi-product has a motion whose speed is v_{tr}, (v_{tr} = ct.) and oscillation amplitude, A_x, ($A_x < A$).

Knowing that the semi-product is an integral part of the oscillator system/UVD technology, in which there is generated a standing wave stable system with a maximum amplitude A, it will determine the distance, a_1, considering the condition $A_x = A$.

In a standing wave stable system, it takes place the equation:

$$A_x = A \cdot \sin\frac{2\pi a_1}{\lambda}, \tag{9}$$

determining :

$$a_1 = \frac{\lambda}{2\pi}\arcsin\frac{A_x}{A}, \tag{10}$$

replacing the value A_x, (relation 9), it will obtain, for a_1, the next expression:

$$a_1 = \frac{\lambda}{2\pi}\left\{\arcsin\left[\sqrt{1-\left(\frac{v_{tr}}{\bar{v}_v}\right)} - \frac{v_{tr}}{\bar{v}_v}\arccos\frac{v_{tr}}{\bar{v}_v}\right]\right\}, \tag{11}$$

with: $\left| v_{tr} / \bar{v}_v \right| \le 1.0$.

When the reflector R_1 is placed at the distance a_2 from the frontal plane of the working concentrator, it will obtain, into the processed semi-product, stationary waves which have maximum amplitude, (A_s); these waves are generated by the interference between the reflected compression wave and the induced straining wave.

The oscillations frequencies of the compression wave and of the straining wave are given by the relations (12):

$$f_1 = \frac{1}{t'} \quad \text{and} \quad f_2 = \frac{1}{t_s - t'}, \tag{12}$$

where: t_s - induced time of the compression and of the straining stresses.

The amplitude of the resultant oscillation, (A_s), is given by the relation (13):

$$A_s = 2A_x \cdot \cos\frac{\omega_1 - \omega_2}{2} \cdot t = 2A_x \cdot \cos\frac{\pi(2t' - t)}{t'(t_s - t')} \tag{13}$$

For the small values of the ratio v_{tr}/v_v, $t_s \approx 2\ t'$, it results that $\omega_1 = \omega_2$ and $A_s = 2 \cdot A_x$

For the big values of the ratio v_{tr}/v_v, it results that $A_s < 2A_x$. Because in the frontal plane of the working tool, at the semi-product bulging out of the deforming area, the oscillation amplitude has the value A_x and in the antinode, it has the value A_s, considering the working concentrator and the processed semi-product as integral parts of the oscillator system in which is generated a standing wave stable system having the maximum amplitude A_s, it will determine the distance x, as it follows: considering the condition given by the equation (14):

$$A_x = 2A_x \sin\frac{2\pi x}{\lambda} = A_s \sin\frac{2\pi x}{\lambda}, \tag{14}$$

it results $x = 0.083 \cdot \lambda$.

So, the distance a_2 from the frontal plane of the working concentrator, where the reflector R_1 will be placed, (when it is the possibility for a maximum reducing of the drawing force used in the processing by UVD system), will be determined using the relation (15):

$$a_2 = \frac{\lambda}{2} - x = 0.417\lambda, \tag{15}$$

The same effects up to the size of the medium drawing force will be obtained when the reflector R_1 is placed at the distance $a_2 + n \cdot \lambda/2$, from the frontal plane of the working concentrator, where n – integer number, (n =1, 2, 3, ...).

The technological system UVD closes with the reflector R_2 which must be placed in one of the vertexes of the semi-product oscillation (Fig. 2) or at the distance $(2n+1)\cdot\lambda/4$ from the frontal plane of the graded cylindrical concentrator.

Fig. 4 presents the image of the equipment used for the metals drawing in ultrasound field/UVD system, equipment which is placed in the

Plastic Deformation Research Laboratory of the Faculty of the Materials Science and Engineering; it can observe the ultrasonic energy reflectors, which have a particular construction consists of the presser rolls, magnetic tighten on the frame of the drawing bench.

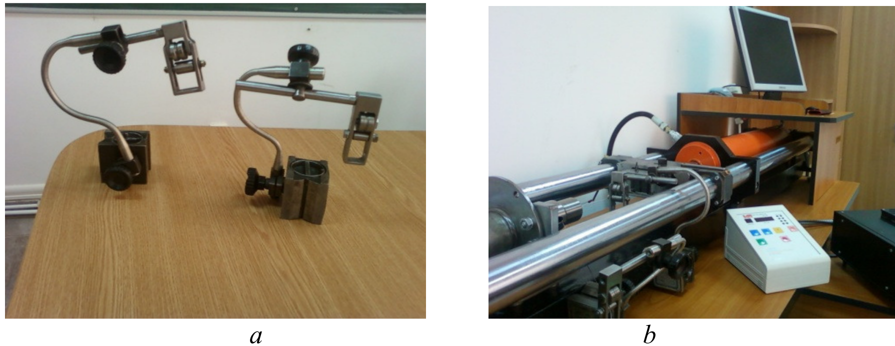

a *b*

Fig. 4 – Photo image of the equipment used for the metals drawing in ultrasound field / UVD system, pointing the ultrasonic energy reflectors: *a* – ultrasonic energy reflectors, *b* – equipment used for the metals drawing.

3. Conclusion

The work gives information about the importance of the ultrasonic energy reflectors/presser rolls, in the processing by drawing of the metals in ultrasound field/UVD system, when the deforming tool, (the die or the mould), is placed in the maximum point of the oscillation/antinode and it is ultrasonic activated along the drawing direction.

The positioning distances of the ultrasonic energy reflectors may be determined using the forming condition of a standing wave stable system, with vertexes and antinodes, into the semi-product which is processed by drawing.

As a matter of fact, the using of the ultrasonic energy reflectors means the distribution of the ultrasonic energy along very well defined distances, going to a higher economical efficiency of the processing by drawing in ultrasound field / UVD system.

A c k n o w l e d g e m e n t. This paper was realized with the support of EURODOC "Doctoral Scholarships for research performance at European level" Project, financed by the European Social Found and Romanian Government.

Received: August 31, 2010

"Gheorghe Asachi" Technical University of Iaşi,
Faculty of Material Science and Engineering
e-mail: bgdnlcn@yahoo.com

R E F E R E N C E S

1. Severdenko V.P., *Prokatka i volocenie ulitrazvukom Nauka i Tehnika.* Minsk, 2000.
2. Susan M., *Tragerea metalelor cu vibraţii ultrasonice*. Edit. Cermi, Iaşi, 2007.
3. Brown B., Goodman I.E., *High-Intensity Ultrasonic.* Ind.l Appl., Hilfe Books, London, 2002.
4. Drăgan Ov. *et al*., *Ultrasunete de mari energii*. Edit. Academiei, Bucureşti, 1983.
5. *** Grant CNCSIS tip A, contract nr. GR 80 / 2007, tema 51, director de proiect Susan Mihai.
6. Susan M., Bujoreanu L.G., *The Metal-Tool Contact Friction at the Ultrasonic Vibration Drawing of Ball – Bearing Steel Wires*. Rev. de Metalurgia, Madrid/Rev. Metal Madrid, **35**, *6*, 379-383 (1999).
7. Jong-Chung Hung, Yu-Chung Tsai, Chinghua Hung, *Frictional Effect of Ultrasonic Vibration on Upsetting*. Mater. Technol., **141**, *3*, 75-80 (2007).

POZIŢIONAREA REFLECTOARELOR DE ENERGIE ULTRASONICĂ LA TRAGEREA METALELOR ÎN CÂMP ULTRASONOR

(Rezumat)

Distanţele de poziţionare a reflectoarelor de energie ultrasonică/rolelor de presare, pentru o eficienţă ridicată, la o sculă de deformare plastică, la tragerea metalelor în câmp ultrasonor, sunt amplasate la punctul maxim de oscilaţie al undelor şi este activat de-a lungul direcţiei de tragere. Acesta este determinat considerând condiţiile ce generează un sistem stabil a undelor în semiprodus.

BULETINUL INSTITUTULUI POLITEHNIC DIN IAŞI
Publicat de
Universitatea Tehnică „Gheorghe Asachi” din Iaşi
Tomul LVI (LX), Fasc. 4, 2010
Secţia
ŞTIINŢA ŞI INGINERIA MATERIALELOR

CONSTRUCTION AND DIMENSIONING ELEMENTS OF THE OSCILLATOR SYSTEM USED IN THE HARDENING AND FINISHING OPERATIONS IN ULTRASOUND FIELD

BY

BRIAN-TUDOR LANDKAMMER, CONSTANTIN BACIU,
MIHAI SUSAN and BOGDAN LUCIAN GAVRILĂ

Abstract. The paper presents the construction and the dimensioning of the oscillator systems which have magnetostriction transducers, the resonant frequency trimming and the materials which are recommended for the realizing of the working graded cylindrical concentrator.

Key words: ultrasounds, oscillator system, standing waves, magnetic transducer, graded cylindrical concentrator, resonant frequency trimming.

1. Introduction

The hardening and finishing process, in ultrasound field or using ultrasonic vibrations, applied to the working part (the ball or the roll), in the case of the plane or cylindrical metals surfaces, is a part of the mechanical treatments [1]. The hardening and finishing of the superficial layer by metals cold plastic deformation with ultrasonic vibrations – DPS, go to the changing of the structure and of the physical and mechanical proprieties of the so-processed products, and, in the same time, to the improving of the surface quality [1], [5].

The success of the hardening and finishing process with ultrasonic vibration depends on the intensity and the quantity of the energy induced into the metal mass. The ultrasonic energy must be high, enough to produce the changing of the propagating medium structure [4].

The ultrasounds which have high energies go to the interaction with the crystal lattice and to the lattice defects, meaning, for the metals which are plastic

processed in ultrasound field, different dying-outs of the elastic oscillations.

The efficiency of the ultrasonic energy in the processes of the metals plastic deformation, depends on the type of the used elastic oscillations, on their intensity, on the possibility of leading, with a high efficiency, of the energetic flow in the area of the deformation focus and on its positioning place, at the level of the oscillator system (maximum of the motion or of the stress).

The ultrasound or ultrasonic waves are different kinds of elastic waves which have the values of the frequency between 16.000 Hz and 10^{10} Hz.

The area of the elastic medium, which is in a vibratory state and which is the place of the ultrasound waves, is called the ultrasound or ultrasonic field. The scheme of the equipment for the hardening and finishing process in ultrasound field is presented in Fig.1, [2].

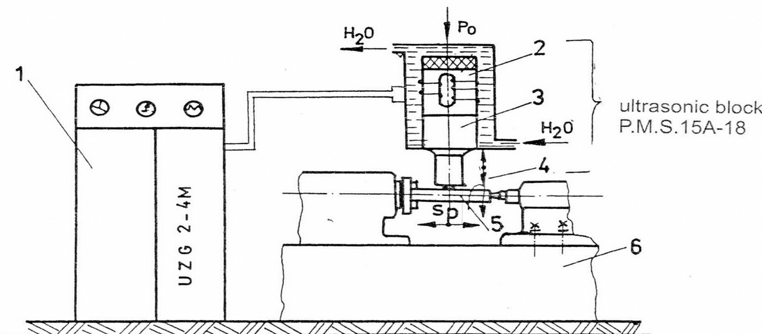

Fig.1 – Principle scheme of the equipment for the hardening and finishing process, in ultrasound field, [2]: *1* – ultrasound generator; *2*– magnetostriction transducer, PMS 15A type – 18; *3* – working graded cylindrical concentrator; *4* – steel balll/RUL1N; *5* – test bar; *6* – universal lathe.

The positions *2* and *3* are the components of the proper oscillator system and represent the most important constructive-functional elements of the equipment for the hardening and finishing process in ultrasound field.

2. Elements of the Oscillator System Construction and Dimensioning for the Hardening and Finishing Process in Ultrasound Field

As a source of primary energy, used for the ultrasound field equipments, are the ultrasound generators with a continuous running; so, the given ultrasound energy consists in a continuous wave.

The construction of the oscillator systems includes, as a rule, the magnetostriction transducer and the ultrasound energy concentrator which has, as an attachment, the tool used for the plastic deformation process; the assembly is braced at the resistance structure of the machine tool, in one of the nodal surface of the wave oscillation, using mechanical shims-nodal flanges.

The working part of the oscillator system is the magnetostriction transducer which changes, with a certain efficiency, based on a specific effect, the electrical oscillations from the source of primary energy, (the ultrasound energy generator), in elastic once. These are sent, concentrated and focused in the plastic deformation area, through the ultrasound energy concentrator.
At the present moment, the magnetostriction electromechanical transducers are the most used. There is a great variety of transducers realized in large ranges of powers and own resonant frequencies, which are adapted with the working bound with the ultrasound generators, as the designs, the dimensions and the cooling conditions, and which must correspond with the technological application, for a certain plastic deformation process.

So, for the efficient working of the oscillator system, its dimensioning must be realized based on the resonant frequency principle. The concentrator of the oscillator system must abbey the following conditions:

- Ultrasound energy sending and concentrating in the deforming focus area;
- Amplification of the particles rate with the increasing of the oscillation amplitude;
- Adequate efficiencies of the plastic deformation processes.

For a good efficiency obtaining, during the ultrasound activated processes of the metals, the concentrators must be trim, with differences consists in only a few periods, to the resonant frequency of the transducer.

The oscillator systems used in the ultrasound activated hardening and finishing processes must work in a resonant running, generating the standing waves which allow a correct dimensioning, a simple construction and a good reinforcing (without energy loses) at the resistance structure of the machine tool, component of the ultrasound processed equipment.

When the oscillator system works in a standing waves running, at the level of the ultrasound energy concentrator, will be generated two characteristic sections: the maximum (antinode) of the waves' oscillation (vertex of the stresses) and the maximum of the stresses (vertex of the oscillations), Fig. 2.

The success of the hardening and finishing process in ultrasound field means the positioning of the working part (the ball or the roll) in the antinode or the maximum of the waves' oscillation.

The dimensioning of the oscillator system is realized in $n \cdot \lambda / 2$, where n is the number of the vertexes and λ is the wavelength.

The working graded cylindrical concentrator having the length $\lambda / 2$ ends the oscillator system on its length.

As a rule, in the construction of the oscillator systems, will be adopted the constructive variant "graded cylindrical" for the working concentrator, especially because of the big value of the amplitude multiplication factor (N), as a ratio between R_0 and RL (R_0 and RL – the radiuses of the two diameters, Fig.3.)

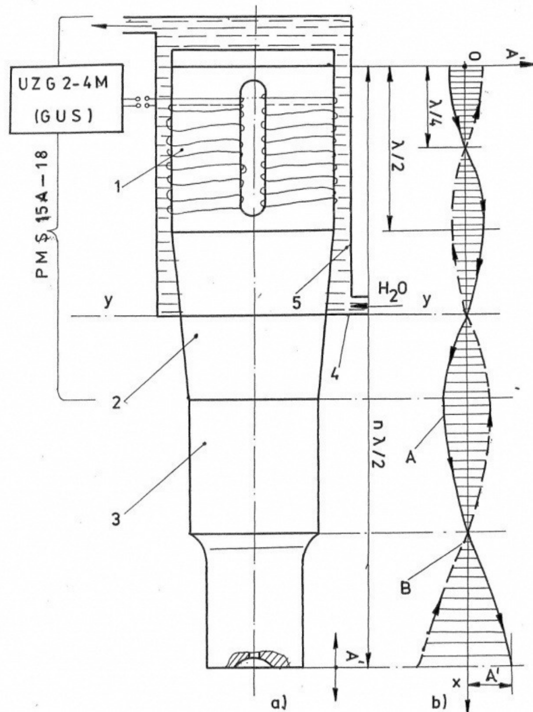

Fig. 2 – Construction and dimensioning elements of the oscillator system:
a – proper construction;
b – waves' oscillation: A – running wave; B – regressive wave;
A' – amplitude of the oscillation:
1 – magnetostriction transducer;
2 – conical concentrator;
3 – graded cylindrical concentrator.

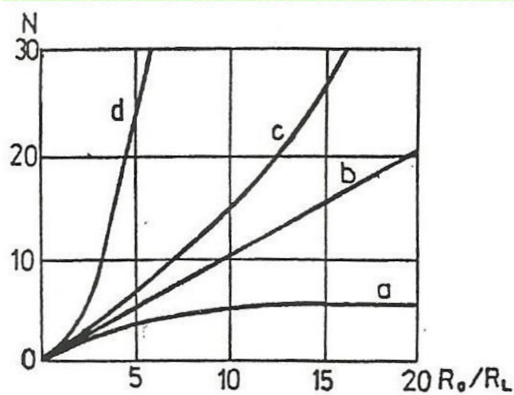

Fig. 3 – Variation curves of the multiplication focus (N) depending on the ratio between the radiuses Ro and RL, [4 and5]:
a – conical; b – exponential; c – graded cylindrical.

Because of the pressure forces during the hardening and finishing process in ultrasound field, as a rule, the resonant frequency has a different value then the calculated one, and it determines the dimensions of the working graded cylindrical concentrator.

This is the reason because it will make a dimensional adjustment of the working concentrators length (both lateral sides turning – symmetrical confronted by the nodal plane), Fig. 4.

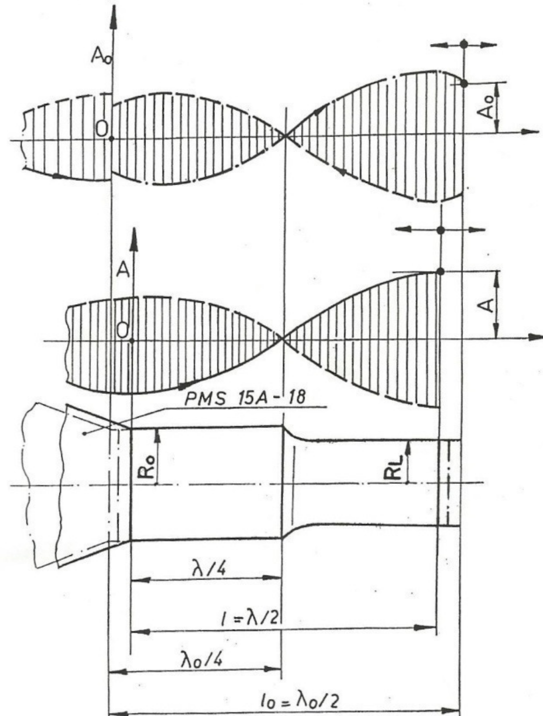

Fig. 4 – Dimensional testing and adjusting of the working graded cylindrical concentrator length by using the resonant method.

It was noted *lo* – initial length of the concentrator:
$lo = \lambda o / 2 = c_o / f_o$, where c_e is the ultrasound wave velocity into the metallic material of the concentrator and f_0 is the initial resonant frequency, without pressure force action.

As a matter of fact, this means that a precise determination of the concentrator length will be made knowing the transducer resonant frequency, the trimming being made by using the relation (1):

$$L=\lambda/2 = c/f, \quad (1)$$

where: *f*- resonant frequency of the oscillator system in a working regime; l-real length of the working graded cylindrical concentrator.

It is recommended a working graded cylindrical concentrator making based on the titanium alloys which have ultrasonic high fatigue endurance.

3. Conclusions

The paper presents the constructional and dimensional elements of the oscillator systems which have magnetostriction transducers, recommended for the hardening and finishing process in ultrasound field.

For a good efficiency of the two operations realizing, it must use ultrasounds with high energies in a standing wave regime which generate vertexes and antinodes of the wave oscillation.

The dimensioning of the oscillator system will be made in $n \cdot \lambda / 2$ .The oscillator system is ended with graded cylindrical concentrator made, as a rule, from alloys based on titanium, which have ultrasonic high fatigue endurance.

The real frequency trimming, in usage, of the working graded cylindrical concentrator will be made using the resonant frequency method.

A c k n o w l e d g e m e n t. This paper was realized with the support of EURODOC "Doctoral Scholarships for research performance at European level" Project, financed by the European Social Found and Romanian Government.

Received: August 25, 2010

Technical University "Gheorghe Asachi" of Iaşi,
Faculty of Material Science and Engineering
e-mail: Tudor_brian@yahoo.com

R E F E R E N C E S

1. Lupescu O., *Netezirea suprafeţelor prin deformare plastică.* Edit. Tehnică – INFO, 1999.
2. *** Contract nr. *4009*/1995 încheiat între Univ. Tehn. "Gheorghe Asachi" din Iaşi şi S.C. Fortus S.A. Iaşi.
3. Marinescu N.İ., *Prelucrări cu ultrasunete*. Edit. Tehnică, Bucureşti, 1986.
4. Drăgan Ov., *Ultrasunete de mari energii.* Edit. Academiei, Bucureşti, 1983.
5. İung – Chung Hung., Yu-diung Tsai., Ching –Hua Hung., *Simulation of Ultrasonic – Vibration Drawing Using the Finite Element Method (FEM).* J. of Mater. Proc. Technol., *140*, 30-35 (2003).

CONSTRUCŢIA ŞI DIMENSIONAREA ELEMENTELOR SISTEMULUI OSCILATOR UTILIZAT ÎN OPERAŢIILE DE FINISARE ŞI DURIFICARE CU ULTRASUNETE

(Rezumat)

Lucrarea prezintă construirea şi dimensionarea sistemelor oscilatorii cu traductori magneto-strictivi, frecvenţă rezonantă de curăţare şi materialele ce sunt recomandate pentru obţinerea concentratorului cilindric de acţionare.

BULETINUL INSTITUTULUI POLITEHNIC DIN IAŞI
Publicat de
Universitatea Tehnică „Gheorghe Asachi” din Iaşi
Tomul LVI (LX), Fasc. 4, 2010
Secţia
ŞTIINŢA ŞI INGINERIA MATERIALELOR

THIN LAYERS OBTAIN BY PLD METHOD

BY

ANCA ELENA LĂRGEANU

Abstract. A new depositing method appears based on laser action named pulsed laser deposition with nice properties of the layers obtained and quite easy to use. The aim of this paper is to present some important informations about this technique, an assembly of equipments used for pulsed laser deposition and few experimental results. A nickel layer deposition on a cast iron substrate was analyzed with a scanning electrons microscope and EDAX equipment.

Key words: pulsed laser deposition, thin layers.

1. Introduction

Nowadays thin films represent a very important area of interest in the material sciences field, mainly because they allow to achieve easily integration criteria. Moreover, they are suitable for preparation of heterostructures and devices with quite reduced size. As a consequence, many preparation methods of thin films are available and well developed. These methods are divided in two main groups: physical methods, such as Pulsed Laser Deposition (PLD) [1] or Sputtering [2], and chemical methods, such as sol–gel [3].

In general, physical methods lead to very good results, giving access to in situ crystallization by heating the substrate during deposition, however, these methods require the use of special equipment, as vacuum chamber, what means a higher cost.

PLD technique [4], [6] is a film preparation method based on irradiation of a target by high energy pulsed laser. This process produces a plasma of the material, which is deposited onto a chosen substrate. The history of laser-assisted film growth started soon after the technical realization of the first laser in 1960 by Maiman. Smith and Turner utilized a ruby laser to deposit the first

thin films in 1965, three years after Breech and Cross studied the laser-vaporization and excitation of atoms from solid surfaces. However, the deposited films were still inferior to those obtained by other techniques such as chemical vapor deposition and molecular beam epitaxy. In the early 1980's, a few research groups (mainly in the former USSR) achieved remarkable results on manufacturing of thin film structures utilizing laser technology.

The breakthrough came in 1987 when Dijkkamp and Venkatesan were able to laser deposit a thin film of YBa2Cu3O7, a high temperature superconductive material, which was of more superior quality than films deposited with alternative techniques. Since then, the technique of Pulsed Laser Deposition has been utilized to fabricate high quality crystalline films. The deposition of ceramic oxides, nitride films, metallic multilayers and various superlattices has been demonstrated. In the 1990's the development of new laser technology, such as lasers with high repetition rate and short pulse durations, made PLD a very competitive tool for the growth of thin, well defined films with complex stoichiometry.

Pulsed laser deposition (PLD) represent a thin film deposition (specifically a physical vapor deposition, PVD) technique where a high power pulsed laser beam is focused inside a vacuum chamber to strike a target of the material that is to be deposited.

This material is vaporized from the target (in a plasma plume) which deposits it as a thin film on a substrate (such as a silicon wafer facing the target). This process can occur in ultra high vacuum or in the presence of a background gas, such as oxygen which is commonly used when depositing oxides to fully oxygenate the deposited films.

While the basic-setup is simple relative to many other deposition techniques, the physical phenomena of laser-target interaction and film growth are quite complex (see Process below). When the laser pulse is absorbed by the target, energy is first converted to electronic excitation and then into thermal, chemical and mechanical energy resulting in evaporation, ablation, plasma formation and even exfoliation [7]. The ejected species expand into the surrounding vacuum in the form of a plume containing many energetic species including atoms, molecules, electrons, ions, clusters, particulates and molten globules, before depositing on the typically hot substrate.

The detailed mechanisms of PLD are very complex including the ablation process of the target material by the laser irradiation, the development of a plasma plume with high energetic ions, electrons as well as neutrals and the crystalline growth of the film itself on the heated substrate. The process of PLD can generally be divided into four stages:

a) Laser ablation of the target material and creation of a plasma;
b) Dynamic of the plasma;
c) Deposition of the ablation material on the substrate;
d) Nucleation and growth of the film on the substrate surface.

Each of these steps is crucial for the crystallinity, uniformity and stoichiometry of the resulting film.

The ablation of the target material upon laser irradiation and the creation of plasma are very complex processes. The removal of atoms from the bulk material is done by vaporization of the bulk at the surface region in a state of non-equilibrium and is caused by a Coulomb explosion. In this the incident laser pulse penetrates into the surface of the material within the penetration depth. This dimension is dependent on the laser wavelength and the index of refraction of the target material at the applied laser wavelength and is typically in the region of 10 nm for most materials. The strong electrical field generated by the laser light is sufficiently strong to remove the electrons from the bulk material of the penetrated volume.

This process occurs within 10 ps of a ns laser pulse and is caused by non-linear processes such as multiphoton ionization which are enhanced by microscopic cracks at the surface, voids, and nodules, which increase the electric field.

The free electrons oscillate within the electromagnetic field of the laser light and can collide with the atoms of the bulk material thus transferring some of their energy to the lattice of the target material within the surface region. The surface of the target is then heated up and the material is vaporized.

In the second stage the material expands in a plasma parallel to the normal vector of the target surface towards the substrate due to Coulomb repulsion and recoil from the target surface. The spatial distribution of the plume is dependent on the background pressure inside the PLD chamber. The density of the plume can be described by a cosn(x) law with a shape similar to a Gaussian curve. The dependency of the plume shape on the pressure can be described in three stages:

a) The vacuum stage, where the plume is very narrow and forward directed; almost no scattering occurs with the background gases.

b) The intermediate region where a splitting of the high energetic ions from the less energetic species can be observed. The time-of-flight (TOF) data can be fitted to a shock wave model; however, other models could also be possible.

c) High pressure region where we find a more diffusion-like expansion of the ablated material. Naturally this scattering is also dependent on the mass of the background gas and can influence the stoichiometry of the deposited film.

The most important consequence of increasing the background pressure is the slowing down of the high energetic species in the expanding plasma plume. It has been shown that particles with kinetic energies around 50 eV can resputter the film already deposited on the substrate.

This results in a lower deposition rate and can furthermore result in a change in the stoichiometry of the film.

The third stage is important to determine the quality of the deposited films. The high energetic species ablated from the target are bombarding the substrate surface and may cause damage to the surface by sputtering off atoms from the

surface but also by causing defect formation in the deposited film. The sputtered species from the substrate and the particles emitted from the target form a collision region, which serves as a source for condensation of particles. When the condensation rate is high enough, a thermal equilibrium can be reached and the film grows on the substrate surface at the expense of the direct flow of ablation particles and the thermal equilibrium obtained.

The nucleation process and growth kinetics of the film depend on several growth parameters including:

a) Laser parameters – several factors such as the laser fluence [Joule/cm^2], laser energy, and ionization degree of the ablated material will affect the film quality, the stoichiometry [8], and the deposition flux. Generally, the nucleation density increases when the deposition flux is increased.

b) Surface temperature – The surface temperature has a large affect on the nucleation density. Generally, the nucleation density decreases as the temperature is increased [9].

c) Substrate surface – The nucleation and growth can be affected by the surface preparation (such as chemical etching [10]), the miscut of the substrate, as well as the roughness of the substrate.

d) Background pressure – Common in oxide deposition, an oxygen background is needed to ensure stoichiometric transfer from the target to the film. If, for example, the oxygen background is too low, the film will grow off stoichiometry which will affect the nucleation density and film quality [11].

In PLD, a large supersaturation occurs on the substrate during the pulse duration. The pulse lasts around 10–40 microseconds [6] depending on the laser parameters. This high supersaturation causes a very large nucleation density on the surface as compared to Molecular Beam Epitaxy or Sputtering Deposition. This nucleation density increases the smoothness of the deposited film.

In PLD, [depending on the deposition parameters above] three growth modes are possible:

1. Step-flow growth – All substrates have a miscut associated with the crystal. These miscuts give rise to atomic steps on the surface. In step-flow growth, atoms land on the surface and diffuse to a step edge before they have a chance to nucleated a surface island. The growing surface is viewed as steps traveling across the surface. This growth mode is obtained by deposition on a high miscut substrate, or depositing at elevated temperatures [7].

2. Layer-by-layer growth – In this growth mode, islands nucleate on the surface until a critical island density is reached. As more material is added, the islands continue to grow until the islands begin to run into each other. This is know a coalescence. Once coalescence is reached, the surface has a large density of pits. When additional material is added to the surface the atoms diffuse into these pits to complete the layer. This process is repeated for each subsequent layer.

3. 3D growth – This mode is similar to the layer-by-layer growth, except that once an island is formed an additional island will nucleate on top of the 1st island. Therefore the growth does not persist in a layer by layer fashion, and the surface roughens each time material is added.

There are many different arrangements to build a deposition chamber for PLD. The target material which is evaporated by the laser is normally found as a rotating disc attached to a support. However, it can also be sintered into a cylindrical rod with rotational motion and a translational up and down movement along its axis.

This special configuration allows not only the utilization of a synchronized reactive gas pulse but also of a multicomponent target rod with which films of different multilayers can be created. Some factors that influence deposition thickness: target material; pulse energy of laser; distance from target to substrate; type of gas and pressure in chamber (oxygen, argon, etc.).

This study presents deposition equipment for PLD method using an Nd: Yag laser, lens systems for wavelength dimension and a vacuum chamber also few results from nickel deposition on a cast iron substrate in 30 minutes process and a 25 mm distance between target and substrate.

2. Experimental Details

For PLD experiments, nickel thin films were deposited from home made targets, which were of 99.7 % Ni purity under wires shape [6].

This process results in dense targets, of which the surface was polished before use in the PLD chamber. The substrate used was a cast iron material with surface polished mechanically until 1000 μm paper quality.

Thin films were grown by PLD in a stainless steel chamber with a substrate—target distance fixed at 25 mm. A Nd: Yag exciter laser (Continuum Surelite brand, 10 ns pulses, λ = 266 nm), presented in Fig. 1 and schematically in Fig. 2, with a focused energy density of almost 1.5 J/cm^2 operating at 2 Hz was used.

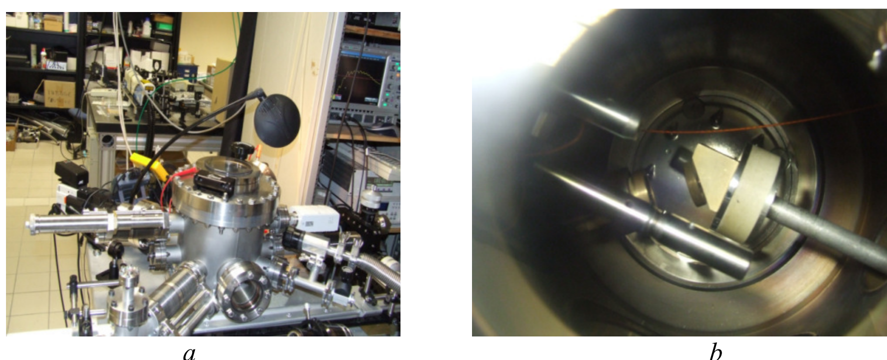

a *b*

Fig. 1 – Pulsed laser deposition chamber: *a* – generally image; *b* – inside detail.

The equipment is based on a laser beam effect on a target, the material that is necessary to be deposited, that create a plasma call plume activated with a high speed, between one and few kilometers per second, by the laser impact with material.

The entire process take place in a vacuum chamber equipped with vacuum windows one of them door type, two catching systems, Fig. 2 *b*), for target and substrate, with a heating system for substrate if necessary, with movement and control possibility and a vacuum system, all of them represented schematically in Fig. 2 as well.

The thin films were grown in 30 min under an oxygen pressure of 0.3 mbar on the substrates heated in the temperature range of 350-400°C.
The estimated spot diameter at the impact point has been 700 μm. The laser beam energy has been continuously monitored by an OPHIR joule meter.

Using a lens system the laser beam is coordinated from laser source to process chamber and establishing the beam length in the same time, in this case being worked with a 266 nm wavelength.

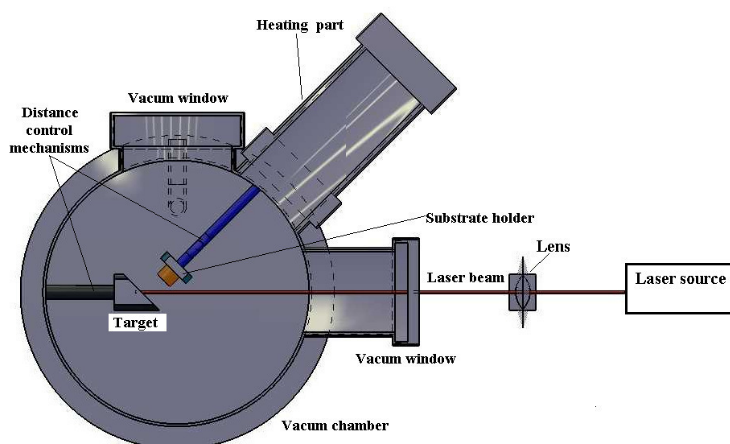

Fig. 2 – Pulsed laser deposition process functional schemes.

Changing the distance between the target and the substrate the properties of the thin layers obtained can be modify by new impact energy between plume and support implications.

The layers quality and properties is influence by the process time in this case being analyzed a sample with a nickel layer growth on 30 minutes period, with continuous movement of target, and with heating of substrate to 400°C.

Experimental Results

Using the PLD method a nickel thin layer were obtain on a cast iron

substrate the SEM (scanning electrons microscope) images being presented in Fig. 3.

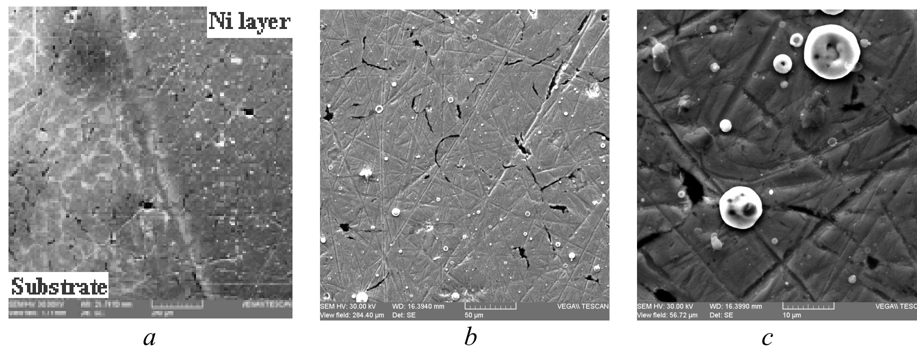

Fig. 3 – SEM images of nickel deposited thin layer on a cast iron substrate by PLD method: *a* – 250 x; *b* – 1000x; *c* – 5000 x.

In Fig. 3*a* with a 250x amplification power is represented the border between substrate, in the left side, and the nickel layer on the right side and increasing the amplification in Fig. 3*b* are observed the big particles of nickel around 1 μm with round shape and in Fig. 3*c* using a higher amplification power are better observed the big particles and also the small ones between 0.1-0.3 μm which is considered very thin comparing with other deposition method [14].

In Fig. 4 is presented the distribution of nickel on a 550 μm distance, surface selected from Fig. 3*a* image. On the left side the substrate is characterize by few carbon compounds shown some peaks and iron in the rest and a very low signal of nickel, chemical element that is not present on the cast iron composition.

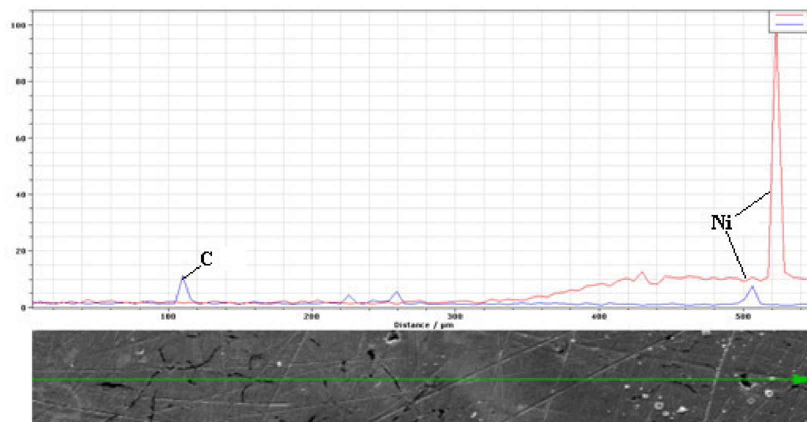

Fig. 4 – Nickel and carbon chemical elements distributions.

Concerning the right side of the diagram presented in Fig. 4 the nickel signal increase on the layer part showing homogeneity of the signal, presenting a very smooth layer, with a high peak on a big nickel particle.

The situation can be explained by the EDAX equipment function, so very tiny layers the substrate elements gives a high signal as well, the case of the layer obtained being between 50 and 150 nm thick but in case of nickel big particles from the deposited layer with concentration near to 100%, peak presented in diagram from Fig. 4 in the very right side, the other chemical elements energy are masked.

In Fig. 5 the nickel element distribution on different areas and amplification powers are presented.

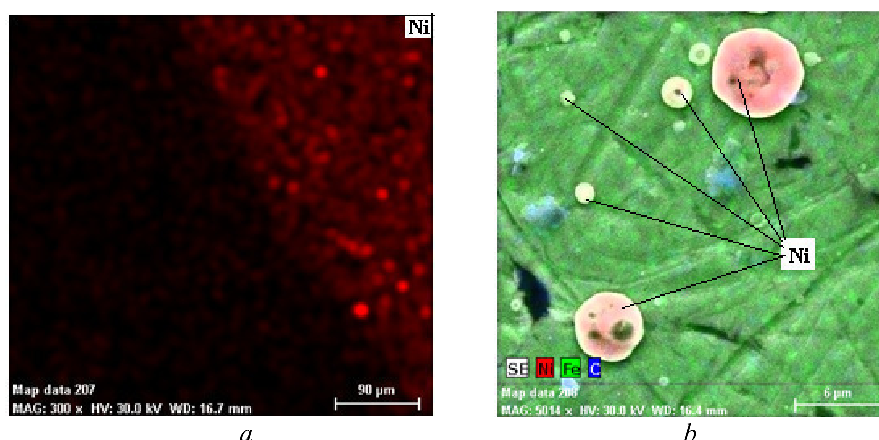

Fig. 5 – Ni chemical element distribution: *a* – 400 µm^2 area; *b* – 25 µm^2 area.

In Fig. 5 *a* is represented the nickel distribution, on a selected area from Fig. 3 *a*, putting in evidence the nickel presence and homogeneity on a 400 µm^2 area. In Fig. 5 *b* are selected the big nickel particles on the nickel layer deposited on cast iron substrate by PLD technique.

3. Conclusion

PLD represent a new, with many advantages, method to obtain metallic or non metallic layers with thickness between 50 and 150 nm.

The deposition equipment is compound from a laser source, a lens systems and a vacuum chamber all connected to obtain a plasma plume from target (the material to be deposited).

The results present a smooth nickel layer with two kinds of particles different between by them dimensions, some of them big with diameter around 1 or 2 µm and most of them of 0.1-0.2 µm.

Received: February 14, 2008

"Gheorghe Asachi" Technical University of Iaşi,

R E F E R E N C E S

1. Willmot P.R., Progr. Surf. Sci., *76,* 163 (2004).
2. Musil J., Baroch P., Vlcek J., Nam K.H., Han J.G., Thin Solid Films, *475*, 208 (2005).
3. Brinker C.J., Hurd A.J., Schunk P.R., Frye C.G., Ashley C.S., J. Non Crystalline Solids, *147*, 424 (1992).
4. Kakihana M., Yoshiura M., Bull. Chem. Soc. Japan, *72*, 1427 (1999).
5. Afonso C.N., Gonzalo J., Nuclear Instrum. Methods Phys. Res., **B 116**, 404 (1996).
6. Weber I.T., Rousseau A., Guilloux-Viry M., Bouquet V., Perrin A., *Microstructure Comparison Between Knbo3 Thin Films Grown by Polymeric Precursors and Pld Methods Solid State Scientific*, *7*, 1317–1323 (2005).
7. Chrisey D.B., Hubler G.K., *Pulsed Laser Deposition of Thin Films*. John Wiley & Sons, 1994.
8. Ohnishi Tsuyoshi, Shibuya Keisuke, Yamamoto Takahisa, Lippmaa Mikk, *Defects and Transport in Complex Oxide Thin Films*. J. l of Appl. Phys. 103: 103703. 2: 10.1063/1.2921972 (2008).
9. Ferguson J.D., Arikan G., Dale D.S., Woll A.R., Brock J. D., *Measurements of Surface Diffusivity and Coarsening During Pulsed Laser Deposition*. Phys. Rev. Let. 103 (25): 256103. 2: 10.1103/Physrevlett.103.256103. Pmid 20366266, 2009.
10. Koster Gertjan, Kropman Boike L., Rijnders Guus J.H.M., Blank Dave H.A., Rogalla Horst, *Quasi-Ideal Strontium Titanate Crystal Surfaces Through Formation of Strontium Hydroxide*. Appl. Phys. Let., 73: 2920. 2: 10.1063 /1.122630 (1998).
11. Ohtomo A., Hwang H.Y., *Growth Mode Control of the Free Carrier Density in Srtio* [*Sub 3−Δ*] *Films.* J. of Appl. Phys., 102: 083704. 2: 10.1063/1.2798385 (2007).
12. Granozio F.M. *et al*., *In-Situ Investigation of Surface Oxygen Vacancies in Perovskites*. Mat. Res. Soc. Proc. 967e (2006).
13. Lippmaa M., Nakagawa N., Kawasaki, M., Ohashi S., Koinuma H., *Growth Mode Mapping of Srtio*[*Sub 3*] *Epitaxy.* Appl. Phys. Let., 76: 2439. 2: 10.1063 /1.126369 (2000).
14. Perju M.C., Găluşcă D.G., Nejneru C., Lărgeanu A.E., *Research Regarding Morphology of Heterogeneous Multiple Coating Layers on Ferrite Perlitic Support Using Vibrating Electrode Method*. Metalurgia Internat., **Xv**, *11*, 41-46 (2010).

STRATURI SUBȚIRI OBȚINUTE PRIN METODA PLD

(Rezumat)

O metodă nouă de depunere a apărut pe baza acțiunii unui fascicol laser denumită depunere cu laser pulsatoriu prezentând bune proprietăți ale straturilor depuse

şi uşor de realizat. Scopul acestui articol este de a prezenta câteva informaţii importante cu privire la această tehnică, un ansamblu de echipamente folosite pentru depunerea cu laser pulsatoriu cât şi câteva rezultate experimentale. Un strat de nichel pe un substrat de fontă a fost analizat cu un microscop cu scanare de electroni şi un echipament EDAX.

BULETINUL INSTITUTULUI POLITEHNIC DIN IAŞI
Publicat de
Universitatea Tehnică „Gheorghe Asachi” din Iaşi
Tomul LVI (LX), Fasc. 4, 2010
Secţia
ŞTIINŢA ŞI INGINERIA MATERIALELOR

ON THE HEAT TRANSFER AT MESOSCOPIC SCALE

BY

RĂZVAN IULIAN LIŢOIU

Abstract. Considering that the microparticle movements take place on fractal curves, a nonlinear equation for the heat transfer at mesoscopic scale is obtained. Moreover, a correspondence with a nonlinear Schrodinger equation is given.

Key words: heat transfer, mesoscopic scale.

1. Introduction

Recent results on the transport and turbulence phenomena at mesoscopic scale [1],…,[5] require the development of a new “scale” physical theories, *i.e.* theories of fractal space-time type (for example the scale relativity theory (SRT)[6-10]) or theories of transfinite physics [11], in which the macroscopic scale specific to the classical quantities coexists and is compatible, simultaneously, with the microscopic “scale” specific to the quantum quantities.

In the present paper we establish a theoretical approach of the heat transfer in nanostructures, using the SRT at Compton scale in fractal dimension $DF = 3$. Moreover a correspondence with a nonlinear Schrodinger equation is given.

2. Mathematical Model

A non-differentiable continuum is necessarily fractal and the trajectories in such a space (or space-time) own (at least) the following properties [6-10]: i) the test particle can follow an infinity of potential trajectories: this leads one to use a fluid-like description; ii) the geometry of each trajectory is fractal (of dimension 3 – for other details on the fractal dimension see [12]). Each elementary displacement is then described in terms of the sum, $d\mathbf{X} = d\mathbf{x} + d\boldsymbol{\xi}$, of a mean classical displacement $d\mathbf{x} = \mathbf{v}dt$ and of a fractal fluctuation $d\boldsymbol{\xi}$,

whose behavior satisfies the principle of SRT (in its simplest Galilean version). It is such that $\langle d\xi \rangle = 0$ and $\langle d\xi^3 \rangle = \left(3\hbar^2/2cm^2\right)dt$ where $\hbar/2m$ defines the fractal/non-fractal transition, *i.e.* the transition from the explicit scale dependence to scale independence, $\hbar$ is the Plank's reduced constant, m is the rest-mass of test particle and c is the light speed in vacuum. The existence of this fluctuation implies introducing new third order terms in the differential equation of motion; iii) time reversibility is broken at the infinitesimal level: this can be described in terms of the two values of the velocity vector for which we use a complex representation, $\boldsymbol{V} = (\boldsymbol{v}_+ + \boldsymbol{v}_-)/2 - i(\boldsymbol{v}_+ - \boldsymbol{v}_-)/2$. We denoted by $\boldsymbol{v}_+$ the "forward" speed and by $\boldsymbol{v}_-$ the "backward" speed.

These "effects" can be combined to construct a complex time-derivative operator [13]

$$\frac{\delta}{dt} = \frac{\partial}{\partial t} + \boldsymbol{V}\cdot\nabla + \frac{\hbar^2}{4cm^2}\nabla^3 \tag{1}$$

Now, the first Newton's principle in its covariant form $\delta\boldsymbol{V}/dt = 0$, becomes [13]

$$\frac{\delta\boldsymbol{V}}{dt} = \frac{\partial\boldsymbol{V}}{\partial t} + \boldsymbol{V}\cdot\nabla\boldsymbol{V} + \frac{\hbar^2}{4cm^2}\nabla^3\boldsymbol{V} = 0 \tag{2}$$

i.e. a Korteweg – de Vries (KdV) type equation in a fractal space-time. This means that, both on the differential scale and on the fractal one, the complex acceleration field, $\delta\boldsymbol{V}/dt$, depends on the local time dependence, $\partial_t\boldsymbol{V}$, on the non-linearity (convective) term, $\boldsymbol{V}\cdot\nabla\boldsymbol{V}$, and on the dispersive one, $\nabla^3\boldsymbol{V}$. Moreover, the behavior of a "non-differentiable fluid" is of viscoelastic or of hysteretic type. Such a result is in agreement with the opinion given in [14, 15]: the non-differentiable fluid can be described by Kelvin-Voight or Maxwell rheological model with the aid of complex quantities e.g. the complex speed field, the complex acceleration field etc. We note that from (2) a nonlinear equation for the heat transfer at mesoscopic scale is obtained

$$\frac{\delta T}{dt} = \frac{\partial T}{\partial t} + \boldsymbol{V}\cdot\nabla T + \frac{\hbar^2}{4cm^2}\nabla^3 T \tag{3}$$

with the temperature field.

Also from Eq. (2) and through the operational relation $\boldsymbol{V}\cdot\nabla\boldsymbol{V} = \nabla(\boldsymbol{V}^2/2) - \boldsymbol{V}\times(\nabla\times\boldsymbol{V})$ we obtain the equation:

(4) $$\frac{\delta \boldsymbol{V}}{dt}=\frac{\partial \boldsymbol{V}}{\partial t}+\nabla\left(\frac{\boldsymbol{V}^2}{2}\right)-\boldsymbol{V}\times(\nabla\times\boldsymbol{V})+\frac{\hbar^2}{4cm^2}\nabla^3\boldsymbol{V}=0$$

If the motions of the "non-differentiable fluid" are irrotational, *i.e.* $\boldsymbol{\Omega}=\nabla\times\boldsymbol{V}=0$ we can **V** choose of the form:

(5) $$\mathrm{V}=\nabla\phi$$

with ϕ a complex speed potential. Then, equation Eq.(4) becomes:

(6) $$\frac{\delta \boldsymbol{V}}{dt}=\frac{\partial \boldsymbol{V}}{\partial t}+\nabla\left(\frac{\boldsymbol{V}^2}{2}\right)+\frac{\hbar^2}{4cm^2}\nabla^3\boldsymbol{V}=0$$

and more, by substituting Eq. (5) in Eq. (6) , we have

(7) $$\nabla\left(\frac{\partial\phi}{\partial t}+\frac{1}{2}(\nabla\phi)^2+\frac{\hbar^2}{4cm^2}\nabla^3\phi\right)=0$$

These yields:

(8) $$\frac{\partial\phi}{\partial t}+\frac{1}{2}(\nabla\phi)^2+\frac{\hbar^2}{4cm^2}\nabla^3\phi=F(t)$$

with $F(t)$ being a function of time only. We realize that Eq. (6) has been reduced to a single scalar relation (8), *i.e.* a Bernoulli-type equation.

If ϕ simultaneously becomes complex speed potential and wave-function, *i.e.* $\phi=-(i\hbar/m)\ln\psi$, the Eq.(8), up to an arbitrary phase factor which may be set to zero by a suitable choice of the phase of ψ *i.e.* $F(t)\equiv 0$, implies the non-linear Schrödinger equation:

(9) $$(\hbar^2/2m)\Delta\psi+i\hbar\partial_t\psi-U\psi=0$$

where

(10) $$U=-\left(\hbar^2/m\right)\Delta\ln\psi-\left(i\hbar^6/4m^2c\right)\nabla^3\ln\psi\ .$$

3. Conclusions

Using the SR model a nonlinear equation for the heat transfer at mesoscopic scale is obtained. Moreover, for an irrotational motion of a fractal

field at Campton' scales and in fractal dimension DF=3, *i.e.* on Peano's type curves, a nonlinear Schrodinger equation is given.

Received: August 31, 2010

"Gheorghe Asachi" Technical University of Iaşi,
Faculty of Material Science and Engineering

R E F E R E N C E S

1. Bourgade J.P., *On Spherical Harmonics Expansion type Models for Electron-Phonon Collisions*. Math. Methods Appl. Sci. **26**, 247-271 (2003).
2. Degond P., Latocha V., Guarrigues L., Boeuf J.P., *Electron Transport in Stationary Plasma Thrusters.* Transp. Theory and Stat. Phys. **27**, 203-221 (1998).
3. Degond P., Méhats F., Ringhofer C., *On Quantum Energy Transport and Quantum Drift-Diffusion Models*. J. Stat. Phys. **118**, 625-665 (2005).
4. Kluksdahl, N.C. Kriman A.M., Ferry D.J., Ringhofer C., *Self-Consistent Study of the Resonant-Tunelling Diode*. Phys. Rev. B. **39**, 7720-7728 (1989).
5. Mounaix P., Vanbésien O., Lippens D., *Effect of Cathode Spacer Layer on the Current Voltage Characteristics of Resonant Tunneling Diodes*. Appl. Phys. Lett. **57**, 1517-1519 (1990).
6. Nottalle L., *Fractal Space-Time and Microphysics. Towards a Theory of Scale Relativity*. World Scientific, 1993.
7. Chaline J., Nottale L., Grou P., *Des fleurs pour Scrödinger: La relativite d'echelle et ses applications*. Ed. Ellipses Marketing, 2009.
8. Noattale L., Chaline J., Grou P., *Les arbres de l'evolution: Univers, Vie, Societes*. Edition Hachette, 2000.
9. Nottale L., Chaos Solitons and Fractals **25**, 797-803 (2005).
10. Nottale L., Célérier M.N., J. Phys. A: Math. Theor. **40**, 14471-14498 (2007).
11. El Naschie M.S., Rösler O.E., Prigogine I., *Quantum Mechanics, Diffusion and Chaotic Fractals*, Oxford: Elsevier, 1995.
12. Madelbrot B., *The Fractal Geometry of Nature*. Freeman, San Francisco, 1982.
13. Agop M., Radu C., Bontas T., *El Naschie's* $\varepsilon^{(\infty)}$ *Space Time and Scale Relativity Theory in the Topological Dimension D=3, Chaos, Solitons and Fractals*. **38** (5), 1243-1253 (2008).
14. Ferry D.K., Goodnick S.M., *Transport in Nanostructures*. Cambridge Univ. Press, 1997.
15. Imry Y., *Introduction to mesoscopic physics*. Oxford Univ. Press, 2002.

TRANSFERUL DE CĂLDURĂ LA SCARĂ MESOSCOPICĂ

(Rezumat)

Considerând că mişcarea microparticulelor au loc pe curba fractalică s-a obţinut o ecuaţie nonlineară pentru transferul de căldură la scară mesoscopică. Este dată şi o corespondenţă cu ecuaţia nonlineară a lui Schrödinger.

BULETINUL INSTITUTULUI POLITEHNIC DIN IAŞI
Publicat de
Universitatea Tehnică „Gheorghe Asachi” din Iaşi
Tomul LVI (LX), Fasc. 4, 2010
Secţia
ŞTIINŢA ŞI INGINERIA MATERIALELOR

THERMAL CYCLING EFFECTS IN Cu-Zn-Al SHAPE MEMORY ALLOYS

BY

BOGDAN PRICOP, NICOLETA MONICA LOHAN and LEANDRU-GHEORGHE BUJOREANU

Abstract. Three fragments of $Cu_{73}Zn_{14}Al_{13}$ shape memory alloy (SMA) were subjected to five cycles comprising controlled heating and free-air cooling, performed on a differential scanning calorimeter (DSC), up to three maximum temperatures, respectively. During the cycles, the variation of specific enthalpy, critical transformation temperatures for reverse martensitic transformation and maximum transformation rate were analyzed as a function of maximum applied temperature. Although the SMA under study generally showed a stabilized behavior, slight variation tendencies were noticed in the variations of above parameters. These evolutions were corroborated with microstructural changes revealed by scanning electron microscopy.

Key words: shape memory alloy, DSC, thermal cycling, critical transformation temperature.

1. Introduction

In spite of the promising development perspectives as constrained-recovery or work-generating applications, the use Cu-Zn-Al SMAs has been hindered by a series of drawbacks caused by metallurgical processing [1], [2], training [3] and cycling [4]. Thermal fatigue was reported to be the primary cause for the change of critical temperatures for reverse martensitic transformation accompanied by the alteration of thermal hysteresis and the formation of oriented equilibrium phases [5],…,[7], as an effect of diffusion. As a result, the degradation of shape memory effect (SME) was noticed in Cu-Zn-Al which was ascribed to the high temperature stabilization of martensite

[7] or to the formation of rhombohedral martensite plates which were irreversibly broken up by twinning.

It is generally considered that thermal cycling causes in Cu-Zn-Al shape memory alloys (SMAs) a decrease of thermal hysteresis and a marked hardening effect. The direct and reverse martensitic transformations occur in different ways and often even the thermal cycling range is varied, a gradual depreciation of thermal memory behavior is expected to occur [8]. Therefore, the present paper aims to monitor the evolution of a Cu-Zn-Al SMA during series of five thermal cycles comprising controlled heating and free-air cooling performed on a differential scanning calorimeter (DSC) up to three maximum temperatures.

2. Experimental Procedure

A $Cu_{73}Zn_{14}Al_{13}$ alloy was cast in an induction furnace then hot rolled and water quenched. Three small fragments were cut and, after mechanical removal of any superficial corrosion they were subjected to three series comprising five cycles up to 453K, 463K and 473K, respectively. For this purpose a NETZSCH differential scanning calorimeter type DSC 200 F3 Maya was used, with sensitivity: < 1μW, temperature accuracy: 0.1 K and enthalpy accuracy: generally < 1%. The device was calibrated with Bi, In, Sn and Zn standards. Each thermal cycle comprised: (i) heating, with 1.67×10^{-1} K·sec^{-1} ; (ii) isothermal maintaining for 180 sec and (iii) cooling to 300 K with a cooling rate of 8.33×10^{-2} K·sec^{-1}.

After the thermal cycling was complete the DSC charts were analyzed and SEM micrographs were taken. The SEM used was a VEGA II LSH TESCAN microscope, coupled with an EDX – QUANTAX QX2 ROENTEC detector.

3. Results and Discussion

Fig. 1 shows the DSC curves of the samples during heating corresponding to the 1st and last cycles of each series up to the maximum temperatures used, 453K, 463K and 473K. As it can be seen in Fig. 1 the peak in all three cases as well as the hysteresis varied from the first to the fifth heating, meaning that a different amount of thermally induced martensite was formed during the previously applied treatment. Also the heat evolution of the transition does not follow the same endothermic path. Small fluctuations of the peak maximum position can be observed. As the number of cycle increased the critical transformation temperatures changed differently, the A_s and A_f droped in temperature while peak maximum position shifted to higher temperatures.

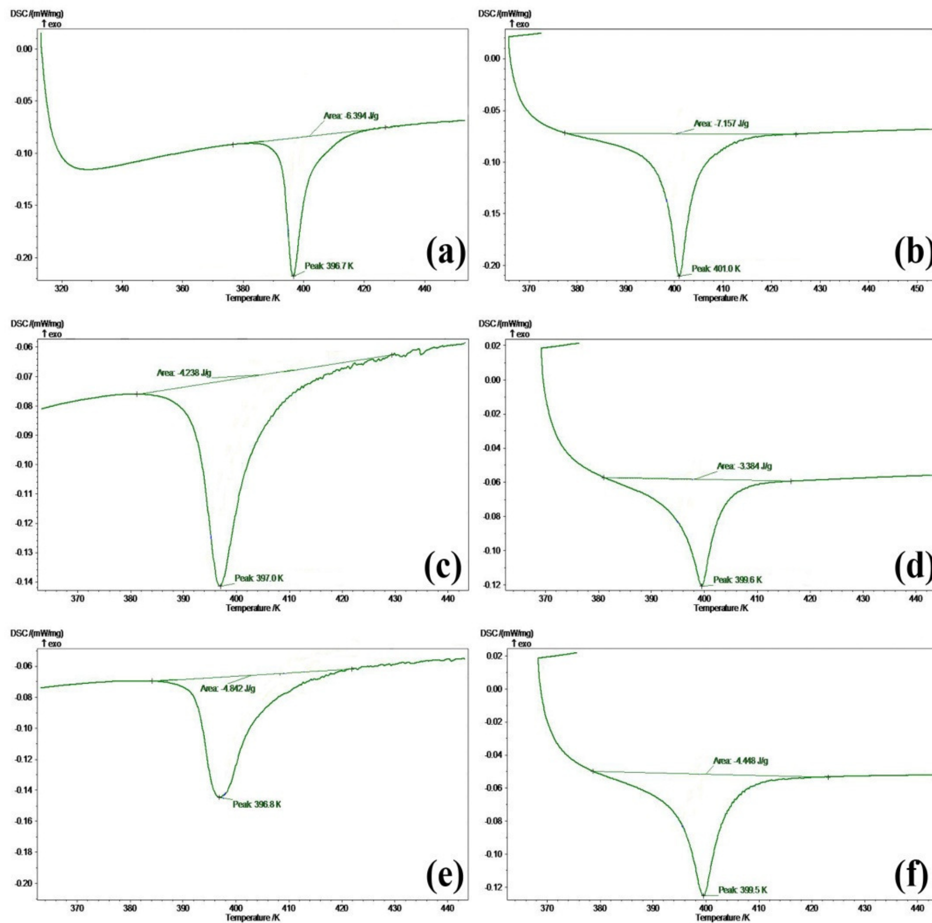

Fig. 1 – Representative DSC charts: *a* – the 1st cycle of heating to 453K; *b* – the 5th cycle of heating to 453K; *c* – the 1st cycle of heating to 463K; *d* – the 5th cycle of heating to 463K; *e* – the 1st cycle of heating to 473K; *f* – the 5th cycle of heating to 473K.

Considering that the initial structure of the specimen is martensitic, during first controlled heating the reversion to parent phase (austenite) occurred, accompanied by the first endothermic peak, as seen in Fig. 1. During cooling, direct martensitic transformation occurred in such a way that thermally induced martensite formed again and reverted back to austenite in the second heating cycle. However, with increasing maximum temperature with 10 K in every next cycling series, Fig.1 showed that reverse martensitic transformation became more stable. When considering this variation tendency, one should take into account that the critical temperatures for this alloy, determined on the electrical resistance vs. temperature curve, have been M_f = 350 K, M_s = 381 K, A_s = 378 K and A_f = 404 K [8] and that these values are lower that those of A_s and A_f,

determined by DSC, due to the delay of the calorimetric signal [9].

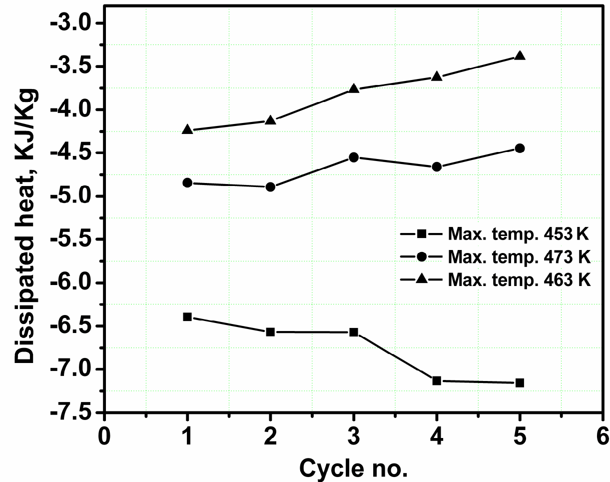

Fig. 2 – Dissipated heat dependences of number of cycles.

In Fig. 2 is illustrated the dependence of dissipated heat with the number of cycles. It can be seen that the sample that undergoes a heating to 453K presents the largest change of hysteresis while the others suffer smaller variation.

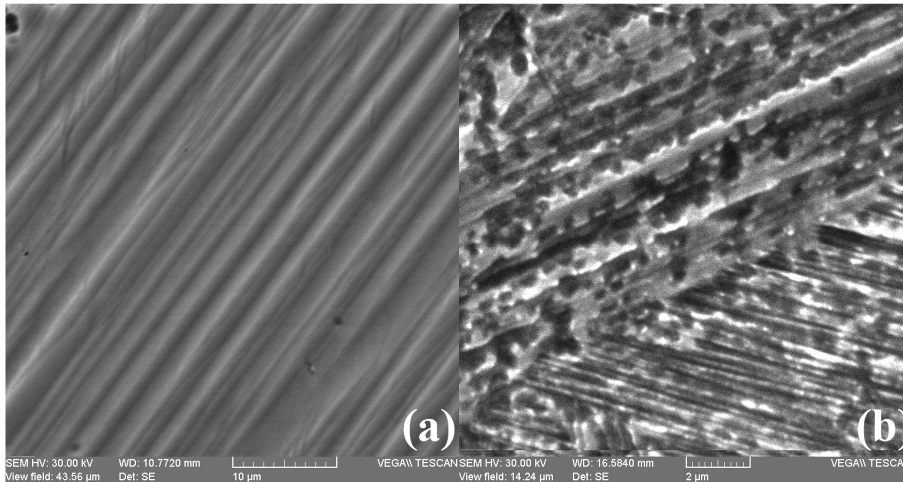

Fig. 3 – SEM micrographs of Cu-15 Zn-6 Al (mass. %) SMA specimen:
a – before; *b* – after thermal cycling.

SEM micrographs were recorded, in Fig. 3, in order to correlate DSC curves with microstructural effects. The micrograph in Fig. 3*a* shows broad

martensite plates with marked relief inside them, suggesting the presence of sub-plates. Their typical widths and depths are 2 μm and 1 μm, respectively. Fig. 3*b* shows martensite plates and differently oriented needles of lath martensite formed after the completion of the cycling.

3. Conclusion

A hot-rolled water quenched Cu-15 Zn-6 Al (mass. %) SMA, with self-accommodated thermoelastic martensite structure, experienced cyclic reversion to austenite during five series of consecutive thermal cycles up to three different temperatures, 453K, 463K and 473K, with a heating rate 1.67×10-1 $K\cdot s^{-1}$ isothermal maintaining for 180 s and a cooling rate of 8.33×10^{-2} $K\cdot s^{-1}$.

The following variation tendencies were noted, with increasing the number of cycles: (i) the process was shifted to lower temperatures and became more stable; (ii) the entire process became slower in such a way that the absolute values of the transformation rates decreased at the end of martensite reversion; (iii) the gradual loss of thermal memory was ascribed to the formation of lath-martensite under the form of stabilized interlocking needles.

A c k n o w l e d g e m e n t. *This paper was realized with the support of EURODOC "Doctoral Scholarships for research performance at European level" Project, financed by the European Social Found and Romanian Government.*

Received: August 26, 2010

"Gheorghe Asachi" Technical University of Iaşi,
Faculty of Material Science and Engineering
*e-mail:*pricopbogdan@ymail.com

R E F E R E N C E S

1. Sampath V., *Effect of Thermal Processing on Microstructure and Shape-Memory Characteristics of a Copper-Zinc-Aluminum Shape Memory Alloy*. Mater. Manuf. Process., *22*, 9-14 (2007).
2. Franz M., Hornbogen E., *Martensitic Transformation of a CuZnAl-Shape Memory Alloy Strengthened by Hot-Rolling*. Mater. Sci. Engng., **A**, *252*, 157–165 (1999).
3. Lovey F.C., Torra V., *Shape Memory in Cu-Based Alloys: Phenomenological Behavior at the Mesocale Level and Interaction of Martensitic Transformation with Structural Defects in Cu-Zn-Al*. Prog. Mater. Sci., *44*, 189-289 (1999).
4. Sade M., Damiani C., Gastien R., Lovey F.C., Malaria J., Yawni A., *Fatigue and Martensitic Transitions in Cu-Zn-Al and Cu-Al-Ni Single Crystals: Mechanical Behaviour, Defects and Diffusive Phenomena*. Smart Mater. Struct., *16*, S126-S136, 2007.
5. Bujoreanu L.G., Craus M.L., Rusu I., Stanciu S., Sutiman D., *On the β2 to α-Phase Transformation in a Cu–Zn–Al-Based Shape Memory Alloy*. J. Alloys Compd., *278*, 190-193 (1998).

6. Bujoreanu L.G., Craus M.L., Stanciu S., Dia V., *Thermally and Stress Induced Changes in Three Phase Structure of Cu-Zn-Al-Fe Shape Memory Alloy*. Mater. Sci. Technol., *16*, 612-616 (2000).
7. Bhuniya A.K., Chattopadhyay P.P., S. data and M. K. Banerjee, *On the Degradation of Shape Memory Effect in Trace Ti-Added Cu-Zn-Al Alloy*. Mater. Sci. Engng., **A**, *393*, 125- 132 (2005).
8. Bujoreanu L.G., Lohan N.M., Pricop B., N. Cimpoeşu, *Thermal Memory Degradation in a Cu-Zn-Al Shape Memory Alloy During Thermal Cycling with Free Air Cooling*. J. Mater. Engng. Perform., 2: 10.1007/s11665-010-9702-5 (in press).
9. Bujoreanu L.G., *On the Influence of Austenitization on the Morphology of α-phase in Tempered Cu-Zn-Al Shape Memory Alloys*. Mater. Sci. Engng., **A**, 481-482, 395-403 (2008).
10. Pelegrina J.L., Torra V., *Comment on "Effects of Heat-Flux Features on the Differential Scanning Calorimetry Curve of a Thermoelastic Martensitic Transformation" by Benke et al.* Mater. Sci. Engng., **A**, 481–482 (2008) 522, Mater. Sci. Engng., **A**, 2. 10.1016/j.msea.2009.06.053, 2009.

EFECTELE CICLĂRII TERMICE ÎNTR-UN ALIAJ Cu-Zn-Al CU MEMORIA FORMEI

(Rezumat)

Trei fragmente din aliaj cu memoria formei $Cu_{73}Zn_{14}Al_{13}$ au fost supuse la o serie de cinci cicluri de încălzire controlată, cu răcire în aer, într-un calorimetru DSC F3 Maia, la trei temperaturi diferite. În timpul ciclarii au fost analizate variațiile entalpiei specifice, temperaturile critice de transformare a reversiei martensitei, în funcție de temperatura maximă aplicată. Cu toate că AMF-ul studiat a prezentat în general un comportament stabil, au fost observate mici variații ale parametrilor sus menționați. Aceste evoluții au fost colaborate cu modificări ale microstructurii puse în evidență de un microscop cu scanare diferențială.

BULETINUL INSTITUTULUI POLITEHNIC DIN IAŞI
Publicat de
Universitatea Tehnică „Gheorghe Asachi” din Iaşi
Tomul LVI (LX), Fasc. 4, 2010
Secţia
ŞTIINŢA ŞI INGINERIA MATERIALELOR

LASER MARKING OF MATERIALS: PRINCIPLES AND PROCESSES

BY

ŞTEFAN RUSU and DAN-GELU GĂLUŞCĂ

Abstract. Preventing and reducing the impact of counterfeiting activities are among the most important preoccupations for modern companies to preserve and protect the value of their work. Laser marking has known a broadening interest in the past decade because of its wide use in industrial applications [1]. The present paper comprises the complete range of laser marking principles, processes and parameters.

Key words: laser, marking, principles, process, parameters**.**

1. Introduction

Laser marking is a rapid, non-contact means of producing permanent high resolution images on the surface of most engineering materials. The most popular sources are pulsed CO_2, Nd:YAG and excimer lasers, with average power levels of several tens of watts. The beam may be scanned or rastered over the material using computer-controlled mirrors, oscillating along orthogonal axes, or projected through a mask or stencil to generate the image [2]. Scanning provides flexibility in character generation, and allows the entire source output to be used. Mask marking is a more rapid method of producing a series of identical marks since the complete image is produced by a single pulse, at the expense of quality and versatility. Dot matrix marking, in which the beam is formed into a matrix of dots that can be turned on or off, allows characters to be generated ‘on-the-fly’.

Since various thermal mechanisms are utilized, marking cannot be categorized as a process that depends purely on heating, melting or vaporization; all three mechanisms may be used in some applications. Laser

marking has little in common with conventional methods of labeling, except for the practical techniques that are used to manipulate the beam into the desired marking pattern. The advantages of laser marking lie in the range of materials that can be marked, the ease with which markings may be changed through changes in software, the speed of the process, the quality of the mark produced, and the low environmental impact.

2. Principles

Five principal mechanisms of marking are used in practical applications, each associated with a particular group of materials and the wavelength of the laser beam. The key to selecting the most appropriate method is to match the material with a laser beam wavelength that will be absorbed only in surface regions [5].

When a laser beam is focused on the surface of a target material, many phenomena may occur as shown in Fig. 1.

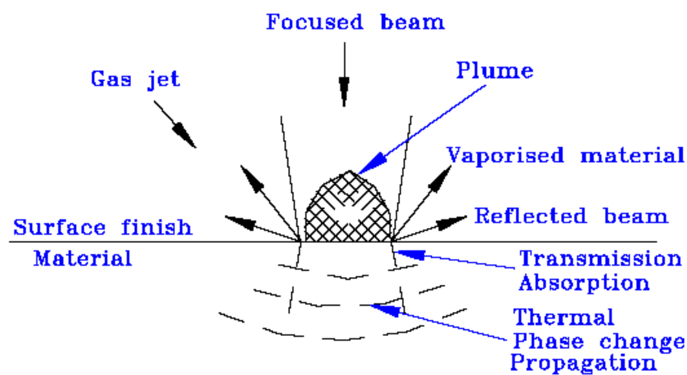

Fig. 1 – Physical phenomena implied by laser marking.

2.1. Foaming and Microcracking

Foaming involves the formation of gas bubbles in surface regions at low temperatures. It is a common marking method for polymers. The bubbles are surrounded by molten material, which may provide sufficient contrast for the mark to be formed. If the temperature is raised slightly, the bubbles may break the surface, thus improving contrast. The laser intensity is low, since no thermal degradation or ablation is required; only the microstructure of the surface is changed. Microcracking results from shallow surface melting (to about 20 μm). Resolidified material contains many microcracks that scatter light and provide contrast with the substrate. Glass is marked using the CO_2 laser in this manner – soda glass marks more easily than thermally resistant types. If fine detail is required, a shorter wavelength excimer laser is used.

2.2. Discoloration

Discoloration occurs when the absorbed beam energy heats the material to a temperature at which thermal degradation is induced. In polymers and woods, the mechanism is referred to as charring, and normally results in a black mark. This method does not affect the surface typography, and is mainly used on specially pigmented plastics and high alloy steel or brass. It is used when the surface must remain flat.

2.3. Bleaching

Colored pigments in special polymers can be changed by a photochemical reaction. Radiation of sufficiently short wavelength, such as that from an excimer laser, dissociates molecules to cause a color change and a permanent mark–Fig. 2.

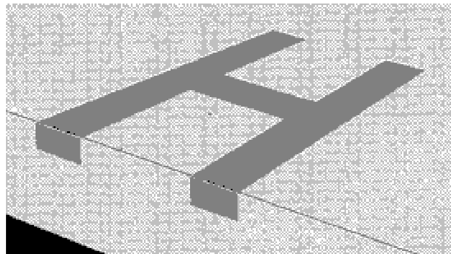

Fig. 2 – Marking by the bleaching technique.

2.4. Engraving

Engraving involves localized melting or vaporization of the surface, typically to a depth of about 0.1 mm. Contrast is provided by the different optical properties of the resolidified/vaporized regions and the substrate. This mechanism is commonly used to mark thermoplastics with CO_2 lasers. Marks may be produced by rastering the beam or by direct vector engraving. Engraving is desirable when an abrasion-resistant mark is required. The image is converted into a matrix of dots in rows in raster marking. Each dot is assigned a value, *e.g. 0* representing white and *1* representing black. As the beam is scanned, it is pulsed when it encounters a dot assigned *1*, creating the image line by line. The resolution is determined by the number of dots per unit length.

Vector engraving involves tracing a line around an object – the beam acts as a pen. The image is converted into a series of coordinates to direct the beam. The conversion can be done electronically, thus saving time and increasing quality.

2.4.1. Engraving: Vaporization

The laser beam is focused to a small spot, which greatly increases the energy density. When the energy is high enough and the surface temperature is raised well above the melting point, most of the material on which the beam is

focused will vaporize. The efficiency of this vaporization process depends on the absorption of the wavelength of the laser radiation [6]. Organic materials and certain glasses have very good absorption of the 10.6 μm wavelength, often 100%. Metals absorb the 1.06 μm wavelength very well but a fraction of the laser energy will be reflected, which may be dangerous.

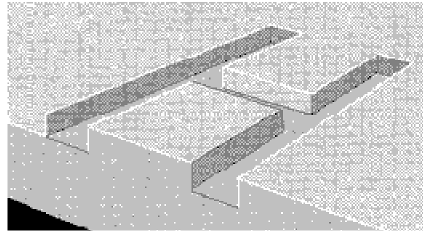

Fig. 3 – Marking through material removal.

2.4.2. Engraving: Melting

Some materials are melted by infrared laser radiation, e.g. metals, epoxies and glass. In the case of metals, mark contrast is achieved by oxidation or incorporation of impurities into the melt. In the case of plastics, the material melts and forms ridges. Depending on types of material, different colors may appear [7]. If the energy density exceeds the ignition point, carbonization occurs, which leads to black lettering. The durability is, however, not good since the carbonized material will wear off, impairing the legibility.

2.5. Ablation

Layer removal/ablation [5] is actually a form of controlled vaporization (Fig. 4). A thin layer of plastic film, paper, ink or paint is vaporized exposing the different colored under-layer. By controlling the heat input, the depth material removed can be controlled and the damage to the underlying surface minimized.

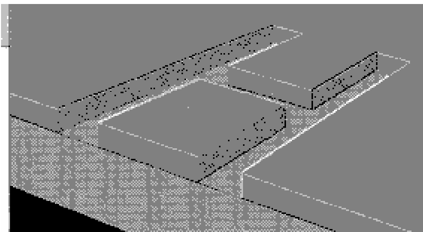

Fig. 4 Marking through layer removal.

Marking by ablating surface regions involves the highest temperature rise, since material must be raised above the vaporization temperature. Material is thus removed, often with little disruption to the surrounding surface [5]. The technique may be used on homogeneous materials, in which case the mark

arises as a result of the contrast between the substrate and the ablated regions. Alternatively, it may be applied to layered substrates; the ablated region reveals an underlying region that provides high contrast – a popular technique for marking polymers.

3. Process Selection

3.1. Characteristics of Laser Marking

Laser marking is flexible; a wide range of materials and components can be marked by selecting an appropriate laser beam. Numerically controlled beam motion provides opportunities to create marks directly from computer-generated images in an unlimited variety of patterns and fonts [8]. Recessed locations with difficult access can be marked, as can moving objects. Laser-marked characters have uniform contrast, good resistance, high resolution and good durability.

Laser marking is a clean process. No paints, inks or acids are used, which could contaminate the product. This also avoids the need to dispose of toxic solvents. Labels are not needed – the mark is made directly on the product. There is no material distortion and no tool wear since it is a non-contact process involving low levels of power. Productivity is high in comparison with conventional processes, especially for short production runs; changes in characters and fonts can be made through changes in software. A laser marker is readily integrated into high volume, high speed process lines. The initial investment cost is high, but in comparison with conventional marking operations, running costs are low.

3.2. Competing Methods of Marking

Ink jet printing is a strong competitor to laser marking, particularly when organic products that cannot be damaged by heat are involved. Dot matrix delivery of ink provides a flexible system of marking alphanumeric characters with high throughput. However, the permanence and legibility of the mark is dependent on the nature and topography of the substrate. The investment cost of ink jet printing is typically one quarter that of a transversely excited atmospheric (TEA)CO_2 laser, but the running and maintenance costs of ink jet printing can be ten times higher because of the consumable costs. Laser printing competes when high volumes are to be marked on substrates that can vary in topography and properties.

Metal stamping produces marks with high permanence that are difficult to remove without producing evidence of tampering. Dies are required, which limit the flexibility of the process if a large range of characters is to be marked. The cost of consumables is high because dies become worn. Worn dies can also cause problems for automatic vision systems. The mark is produced by plastic

deformation of the substrate, which presents no problems for labels that are to be applied to components, but which may be unsuitable for direct marking. Laser marking produces less deformation.

Dot peening (micropercution) and s*cratching* techniques, conducted by CNC-like machines, represent a strong alternative to laser marking, regarding the process flexibility (computer operated), and also the operating speed. The quality of the markings is close to the laser induced versions, while the initial investment is at 50%. The consumables (very few in number: stylus, springs) costs are relatively insignificant, but can become significant in case of intensive use. Furthermore, laser marking ia comparably a clean process (scratching leaves material residue), with a incomparable lower noise level.

Preprinted labels provide clear marks, but large quantities must normally be produced, resulting in high waste. Labeling is not a very flexible process if codes are changed regularly. Label making also involves an added production stage.

Chemical etching produces marks of high permanence, but relatively slowly. Since masking is often required, the flexibility of the process is also low. Of increasing concern is the environmental impact of chemicals.

Processes such as *embossing*, *silkscreen printing* and *pantograph printing* all suffer from high consumable costs, and are less clean operations than laser marking.

3.3. Practice

The choice of a laser marking system depends on many factors: the materials to be marked, the throughput, the permanence, the flexibility and the tolerance of the substrate to marking. There are no simple rules that can be applied to all cases; each must be considered on its own merit. Additional complications are introduced by the interactions between process variables.

3.4. Material Properties

Metals and alloys are good reflectors of the far infrared light of the CO_2 laser, and so Nd:YAG or excimer lasers are normally the sources of choice for marking bare metals [2]. The mechanism of marking is normally ablation or discoloration resulting from the deposition of metal compounds from the process gas. Alternatively, a coating can be applied to the surface, which is fused by the laser beam, leaving a permanent mark; the remaining coating is washed away. Aluminium can be anodized and colored – marks can then be produced by ablating the anodized layer (which absorbs infrared radiation well) to reveal the substrate. The gold-coated lids of electronics packages are marked using Nd:YAG lasers. The gold is present as a thin-plated layer on nickel, which is used to coat a Kovar substrate. A black mark, with good contrast against the gold background, is produced.

Many polymers, notably polyethylene and polypropylene, absorb the infrared radiation of CO_2 and Nd:YAG lasers poorly. The absorptivity of polyolefins can be increased by mixing in pigments, typically in quantities around 0.1 vol.%. Pigments such as metal oxides and mica in particle sizes about 2–3µmin diameter improve absorptivity without degrading the quality of the mark. Suitable pigments should not change the color or mechanical properties of the polymer, and be non-toxic if used in applications involving food packaging.

Glasses, which are used in transmissive optics with Nd:YAG laser output, cannot normally be marked using this laser. Pulsed CO_2 laser output is suitable for etching characters by ablating or microcracking the substrate. For high precision markings, the excimer laser can be used to generate microcracks in the surface without thermally disrupting the surrounding material.

Ceramics absorb light of a wide range of wavelength well, and so a variety of lasers can be used for thermal marking. However, the brittle nature of ceramics, particularly in the fused state, places limitations on the mechanisms of marking that can be used [9]. Silicon wafers can be marked by the Nd:YAG laser at the beginning of the semiconductor manufacturing process by melting a thin surface layer without thermally affecting the substrate.

3.5. Beam Characteristics

The pulsed TEA CO_2 laser is the most common source for marking non-metallic consumer products. A typical set of processing parameters would be: 50–100W average power; 1–2µs pulse duration; and 1–20 J cm−2. Slow axial flow and sealed CO_2 lasers are also used, typically with power levels in the range 10–25W in CW mode, and 3–5 J per pulse in pulsed mode. A CO_2 laser beam can be delivered using a mask, beam manipulation, and dot matrix rastering, discussed below. Optics are relatively expensive because of the far infrared wavelength of the beam. Marks are produced principally by a thermochemical reaction (melting or vaporization). Far infrared light is particularly suitable for organic materials such as paper and otherwood products,many plastics and ceramics, and for removing thin layers of paint or ink from a substrate.Metallic surfaces can be marked using absorptive coatings, and polymers marked by colour changes induced by heating.

The Nd:YAG laser can also be used in CW or pulsed operation [5]. The average power level normally lies between 10 and 120W, while pulses of peak energy 10 mJ and peak power 60kW are produced in pulsed mode. Q-switching is used to develop high peak pulse energies. Marks are produced by a thermochemical reaction in a similar manner to the CO_2 laser, but because of the shorter wavelength of Nd:YAG laser light, finer detail can be marked. The beam is normally delivered via a scanning optical system [2]. Nd:YAG laser marking is suitable for the same materials as the CO_2 laser, but the light is absorbed more strongly by metals. Frequency-doubled output at 532nm can be

produced, which is suitable for marking by photochemical reactions such as bleaching.

The excimer laser is well absorbed by polymers and glasses because of its short wavelength. The output is pulsed, with energy in the range 150 to 400 mJ, and marking is normally achieved using masks. The longer wavelength excimer lasers (xenon chloride at 308nm and xenon fluoride at 351 nm) are used for surface marking of plastics because most polymers absorb well at these wavelengths. The short wavelength of the argon fluoride laser (193 nm) cleanly ablates glass by a photochemical mechanism with no peripheral damage.

4. Laser marking process parameters

4.1. Effects of average, peak power and pulse energy

The best marking results are obtained only when there is a proper combination of pulse energy, pulse duration, average and pulse repetition rate. The pulse duration (μs) is defined as the period during which the laser power intensity exceeds 50% of the maximum power intensity. The peak power is determined by:

$$P_p = \frac{E_{ov}}{\mu} \quad (1)$$

For a laser with high pulse repetition rate, the peak power is usually expressed in terms of average power:

$$P_p = \frac{P}{\mu \cdot PRR} \quad (2)$$

where *P* is the average power, and *PRR* is the pulse repetition rate.

A high peak power is often preferred in marking process for fast vaporisation. As described in equation (1), the peak power is determined by the pulse energy and the pulse duration. Shorter pulses have higher peak power. The thermal interaction time is also shorter, which lead to smaller heat-affected-zones, and thus better hole quality. However, it should be noted that the pulse energy is usually high for high order beam modes, which produce large divergence angles [6]. In the case of very fine marking, this situation is undesirable except for mask projection marking such as excimer laser marking.

4.2. Effects of beam focal position

A beam of finite diameter is focused by a lens to obtain a smaller beam spot, as shown in Fig. 5. If the diameter of the focused spot, d_0, is defined as the diameter which contains 86% of the focused energy, the focus spot size is determined by:

(3) $$d_0 = \frac{2f\lambda}{D}$$

where, f is the focal length of the focus lens, D is the entrance beam diameter, and λ is the wavelength.

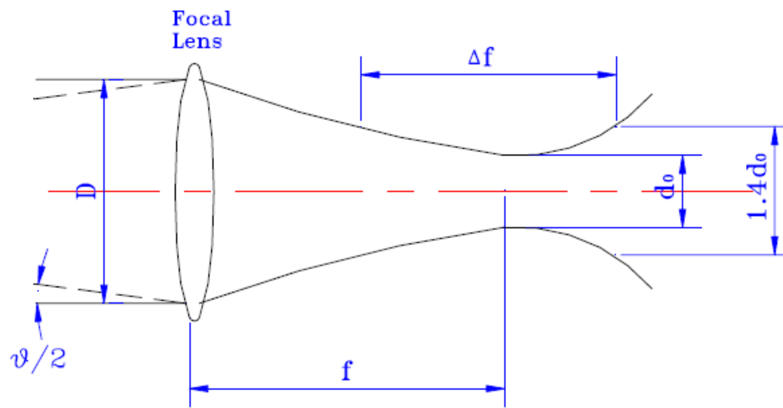

Fig. 5 – Focusing of a Gaussian beam.

If the total beam divergence angle θ is known, the diameter of the focus spot size is given by:

(4) $$d_0 = f \cdot \vartheta$$

As the Gaussian beam focuses from a lens down to a waist and then expands, there is a need to define a depth of focus. Normally, it is defined as the distance between the two d_0 spot size points or two times the Rayleigh range. It can be written as:

(5) $$\Delta f = 2Z_R \sim 2\pi\lambda F^2$$

or:

(6) $$\Delta f = \frac{2f^2\theta}{D}$$

where F is the f-number of a focusing lens, which is defined as:

(7) $$F = \frac{f}{D}$$

It is concluded from eqs. (3) to (7) that a lens with a longer focal length gives a greater depth of focus and a larger focus spot size than a lens with a shorter focal length. Thus the focal length of the focus lens should be selected properly according to the marking requirements.

4.3. Effects of Beam Mode and Spot Size

Because the order of the beam mode has great effect on both the focused spot size and the depth of focus [1], the beam mode structure plays an important role in laser materials processing. A laser beam with a higher-order mode structure diverges more rapidly, focuses to a larger spot and has a shorter depth of focus than a TEM00 Gaussian beam.

Because in laser marking it is generally desirable to achieve highest possible speed and therefore the highest possible power density, the lowest order mode is desirable (TEM00 or Gaussian mode for stable resonators). However, a low-order mode structure often means a lower conversion efficiency and thus less laser output power. Therefore the process must be optimized for good processing quality, proper processing speed, and laser output power.

4.4. Laser Wavelength

Generally, shorter wavelengths are much better absorbed by materials [3]. The wavelength also determines the theoretical minimum focused spot size. For a TEM00 laser with diffraction-limited optics, the focused spot size, s, is given by:

$$s = 1.27\lambda(f/d) \tag{8}$$

where λ is the laser wavelength, f is the lens focal length, and d is the diameter of the beam (entering the lens). It is obvious that the focused spot is proportional to the laser wavelength. When the laser wavelength is halved, the spot size is reduced by a factor of two. The wavelength also determines the interaction mechanism - thermal or photochemical; also, the reflectivity of a material is a function of the wavelength.

4.5. Material Properties

For any material, absorptivity, reflectivity, and transmissivity will satisfy:

absorptivity + reflectivity + transmissivity =1

In general, metals absorb the Nd:YAG laser beam energy well, while paper and most transparent materials (e.g. polymers and glass) absorb the CO_2 laser energy well. Almost all materials absorb well the short wavelengths of excimer laser beams [6].

Surface finish or coating affects the absorptivity. Bare metal surface will be difficult to mark by CO_2 lasers, but can be easily marked by Nd:YAG or

excimer lasers. Glass and transparent plastics are not suitable for Nd:YAG laser marking. Nearly all materials can be marked by excimer lasers with a shallow engraving.

4.6. System Requirements

In order to obtain the minimum linewidth and highest power density, laser beam shall focus on the work piece surface. Overlap is another important factor affecting mark depth, width, and continuity [2]. The *PRR* and the marking speed together determine the percentage overlap in the laser spots. A good deal of overlap can ensure that the engraving lines are continuous and that splattering will be kept small. If the percentage overlap (in %) is defined as $\mu = x/s$, then:

$$\mu = \frac{x}{s} = \left(1 - \frac{l}{s}\right) \times 100\% \tag{9}$$

where s is the spot size, x is overlap length, and l is the centre-to-centre spacing between the pulsed spots, which is given by:

$$l = \frac{v}{PRR} \tag{10}$$

where *PRR* is the pulse repetition rate in pps, and v is the engraving speed in m/sec.

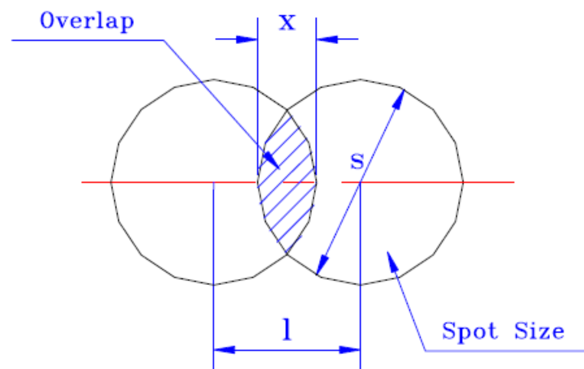

Fig. 6 – Spot overlap.

Therefore, the required spot size is related to marking speed and pulse repetition rate by:

$$s = \left(\frac{100}{100-\mu}\right)\frac{v}{PRR} \tag{11}$$

Generally speaking, the spot overlap is required around 70% to 90% to ensure a good marking.

5. Marking Quality Characteristics

The quality of a mark is assessed by its legibility characteristics such as mark contrast, mark with, mark depth, spattering and microcracks. The characteristics are usually evaluated using complementary techniques such as optical microscopy, ultrasonic microscopy, electron microscopy, surface roughness measurement, and contrast evaluation devices. The acceptance of level of each of these characteristics generally depends on the manufacturer's requirements.

5.1. Mark Width

Mark width refers to the width of the line segment that forms a character. With the mask image marking, the mark width in the characters is essentially determined by the mask geometry and the lens imaging quality. It can be as small as a few micro-meters, which can only be read under a microscope. In beam deflected marking, the line width is mainly determined by the focused beam spot size, which varies between 20 - 100 mm. Other parameters such as scanning speed, power density and material properties also affect the line width. A toolmaker’s microscope or Talysurf surface texture measuring equipment is used for the line width measurement.

5.2. Marking Depth

The depth of marking depends on energy density, types of materials and the beam/material interaction time. In mask marking, the vaporization depth is often determined by the thickness of paint or oxidation layer. It is typical of a few microns to several tens of microns. In beam deflected marking, greater depth of penetration into the material can be achieved varying between a few microns to several tens of a millimeter. A further enhancement of the effect on the material can be realized by the supply of gases such as oxygen or compressed air, which assist material removal [6]. A Rank Taylor Hobson surface analyzer or a laser beam scanning profiler can be used for depth measurement.

5.3. Mark Contrast

Marking contrast is the visual difference between the apparent brightness of the marked surface and unmarked surface of a workpiece. An Image Analysis System can be used for the contrast measurement. It comprises a PC, a 2-axis precision table, a CCD camera and monitor. The light source is a tungsten incandescent light bulb. A reference black and white background provides two extreme grey levels as references in computing the mark contrast, hence compensating for the difference in illumination conditions and the

variation of the electronic gain in the system. A histogram plot of the average gray level of the mark, the background material, and the black and white backgrounds are obtained. The marking contrast, c, can be defined as a percentage value as:

$$c = \frac{|g_{background} - g_{mark}|}{|g_{white} - g_{black}|} \quad (12)$$

The sharpness or resolution of the marked edges affects the marking contrast. This parameter is particularly important in marking “bar code”, as poor edge sharpness may fail bar code reader. High peak power or power density produces better edge resolution.

5.4. Scattering

Scattering is characterized by the presence of re-solidified droplets of surface material in the marking area. These scattering are undesirable as they distort mark boundary and producing poor line definition. Visual inspection with an optical microscope is often suffice to evaluate the effect.

5.5. Microcracks

Microcracks are created due to thermal stress generated during laser marking. The micro-cracks affects mechanical properties and may induce corrosion in metals. Scanning acoustic microscope and scanning electron microscope can be used for detection and analysis.

5.6. Continuity

When pulsed or Q-switched CW lasers are used, the repetition rate affects the continuity of the marking. Marking speed is another key factor. An optical scope is used to evaluate the effect.

6. Summary and Conclusions

Laser marks can be produced using both thermal and athermal modes of beam–material interaction. Each thermal mechanism is characterized by a temperature rise that ranges from heating (in the case of discoloration), melting (foaming and microcracking), and vaporization (engraving). Both CO_2 and Nd:YAG lasers can be used to induce thermal modes of marking. Athermal marking involves chemical change on the level of atomic bonds, for which excimer lasers are more suited. Since the capital cost of laser marking equipment is high in comparison with conventional methods, the technique is most suitable for high productions runs, applications in which flexibility is required, and where quality must be high. The capital cost can then be offset

against the relatively low running costs and the durability of the equipment. The number of industrial sectors that have adopted laser marking is testament to the advantages that it provides.

A c k n o w l e d g e m e n t. This paper was realized with the support of EURODOC "Doctoral Scholarships for research performance at European level" Project, financed by the European Social Found and Romanian Government.

Received: August 31, 2010

"Gheorghe Asachi" Technical University of Iaşi,
Faculty of Material Science and Engineering
e-mail: rusu.st@gmail.com

R E F E R E N C E S

1. Ready J.F., *Industrial Applications of Lasers*. Acad. Press, 1997.
2. Sintec Optronics Pte Ltd, *Laser Marking Mechanism and Quality Characteristics*, 2010.
3. Ion J.C., *Laser Processing of Engineering Materials*. Elsevier Butterworth-Heinemann, 2005.
4. ten Hompel M., Schmidt T., W*arehouse Management – Automation and Organisation of Warehouse and Order Picking Systems*. Springer, 179-220, 221-281 (2007).
5. Dowden J. (Ed.), *The Theory of Laser Materials Processing*. Springer Sci., Business Media B.V., 2009.
6. Kannatey-Asibu E. Jr., *Principles of Laser Materials Processing*. John Wiley & Sons, Inc. (2009).
7. Gu B., Schramm R., Gillespie J., Mezack G., Cunningham A., *Laser Wafer Marking at Die Level*. GSI Lumonics, 2003.
8. Dusser B., Sagan Z., Bruneel D., Jourlin M., Audouard E., *Laser Deep Marking of Metals and Polymers: Potential Interest for Information Coding*. IOP Publ. Ltd, 2007.
9. *Laser-Surface Interactions for New Materials Production*. Springer Series in Mater. Sci., 2009.

MARCAREA LASER A MATERIALELOR
I. Principii şi procese

Prevenirea si reducerea impactului actiunilor de falsificare reprezinta preocupari de maxima importanta pentru companiile moderne, scopul fiind de a pastra si proteja valoarea activitatilor lor. Marcarea cu laser a reprezentat o tehnologie de interes crescut in ultima decada, datorita compatibilitatii sale cu un numar de vast domenii aplicative industriale. Prezenta lucrare contine un compendiu complet al principiilor, proceselor si parametrilor aferenti marcarii cu laser.

BULETINUL INSTITUTULUI POLITEHNIC DIN IAŞI
Publicat de
Universitatea Tehnică „Gheorghe Asachi” din Iaşi
Tomul LVI (LX), Fasc. 4, 2010
Secţia
ŞTIINŢA ŞI INGINERIA MATERIALELOR

LASER TECHNOLOGY FOR APPLICATIONS IN MARKING

BY

ŞTEFAN RUSU and IOAN RUSU

Abstract. Direct laser engraving on a surface is a very flexible method that allows permanent marking of identification and traceability information via for instance 2D data matrix codes [1]. A wide range of applications can therefore be directly and efficiently addressed. The present paper comprises a complete analysis of laser marking technologies and applications.

Key words: laser, marking, technology, application.

1. Introduction

Laser marking is a rapid, non-contact means of producing permanent high resolution images on the surface of most engineering materials. The most popular sources are pulsed CO_2, Nd:YAG and excimer lasers, with average power levels of several tens of watts. The beam may be scanned or rastered over the material using computer-controlled mirrors, oscillating along orthogonal axes, or projected through a mask or stencil to generate the image [2]. Scanning provides flexibility in character generation, and allows the entire source output to be used. Mask marking is a more rapid method of producing a series of identical marks since the complete image is produced by a single pulse, at the expense of quality and versatility. Dot matrix marking, in which the beam is formed into a matrix of dots that can be turned on or off, allows characters to be generated ‘on-the-fly’.

Several distinct mechanisms of marking can be identified, but none is understood well enough to be modeled accurately. Trial and error testing is therefore the most common means of establishing processing parameters. Around 90% of industrial laser marking is carried out for product identification

in industries including domestic goods, microelectronics, automotive and aerospace – the remainder being for aesthetic applications such as decorative patterns and company logos. As the scale of marking decreases through the use of short wavelength lasers, opportunities for micromarking will grow; security marking and anti-counterfeiting features are large potential markets.

2. Marking Technologies

2.1. Masks

The mark may be formed by illuminating a mask, or reticule, that contains the desired pattern, as illustrated in Fig. 1. The mask may be a metal stencil, which contains connecting strips, or glass substrates covered with dielectrics. It may be positioned close to the workpiece, or the transmitted pattern may be focused to the desired size on the object using a lens. Mask marking is rapid if the mask does not need to be changed. Different masks can be mounted on a revolving wheel and positioned accordingly, although this reduces the marking rate. Since only a part of the beam is transmitted to make the mark, fairly high power lasers are needed. TEA CO_2 and excimer lasers are normally used in mask marking. This technique is popular for sequential coding, batch coding, and open or closed date coding, with a wide range of materials including paper, glass, plastics, coated materials and ceramics, which are marked by discoloration [3]. Masking is also the method of choice for complex patterns that do not change – it is considerably faster than beam scanning.

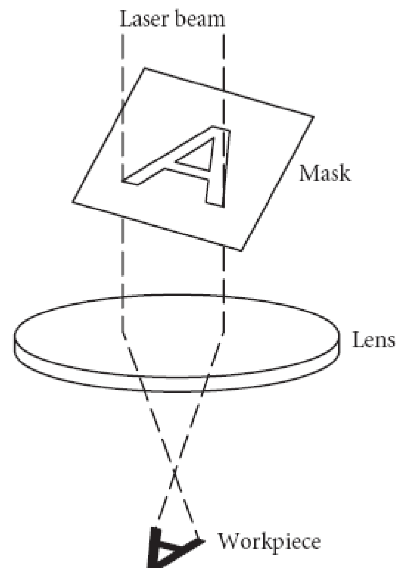

Fig. 1 – Marking using a mask.

2.2. Rastering

The laser beam can be guided using computer numerically controlled mirrors over a marking area, which is typically 100×100 mm. The beam is first expanded, to reduce divergence, and directed towards the galvanometer mirrors. It passes though a lens and is focused onto the workpiece, as illustrated in Fig. 2. Any desired image may be drawn using appropriate programming. Software is available in control systems, providing a flexible system capable of marking

with a variety of fonts. The mark is of very high quality, but the process is slower than single mask marking. The complex optics and the necessary shielding increase the system cost.

A Nd:YAG laser is normally used in CW or Q-switched mode since the narrower lines produced are suited to this technique. Raster marking is a popular replacement for acid and electro-etch marking, stamping and punching, ink jet and other printing systems. Slow axial flow and sealed CO_2 lasers can give higher throughput on non-metals, and these systems are generally cheaper than Nd:YAG systems. Scanning is typically used for serialization of plastic and ceramic products, and products requiring high quality graphics. One advantage is that the entire power of the laser beam is used for marking.

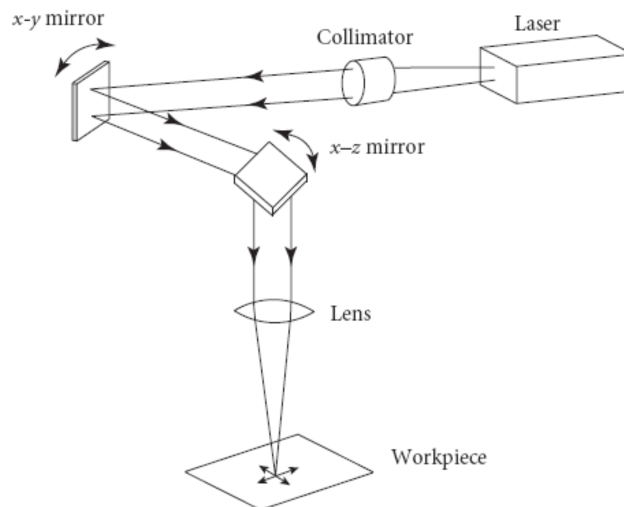

Fig. 2 – Marking using rastering mirrors.

2.3. Vector Marking

This type of marking (Fig. 3*a*) implies several vectorial combinations, which can potentially influence the substrate (Fig. 3*b*).

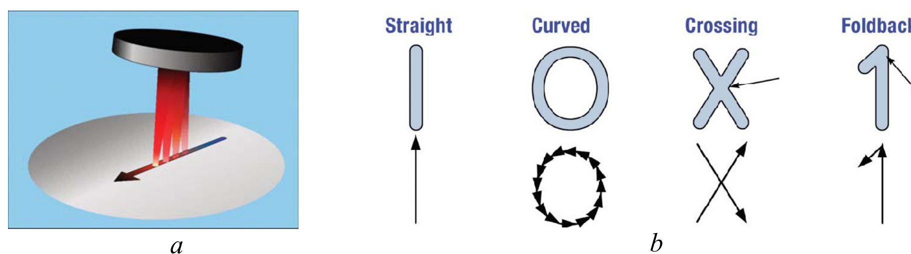

a *b*

Fig. 3 – Vector laser marking (*a*) and vector text features (*b*).

When laser beam hits the target, a heat-affected zone is generated due to thermal effects [4]. It is important to understand how deeply the laser energy would penetrate into the substrate, and what potential damage there might be to any of the device's internal structures. The mark depth is observed along with some partially ejected substrate material protruding above the original surface, and a heat-affected zone (melted and re-crystallized silicon) as illustrated in Fig. 4*a*.

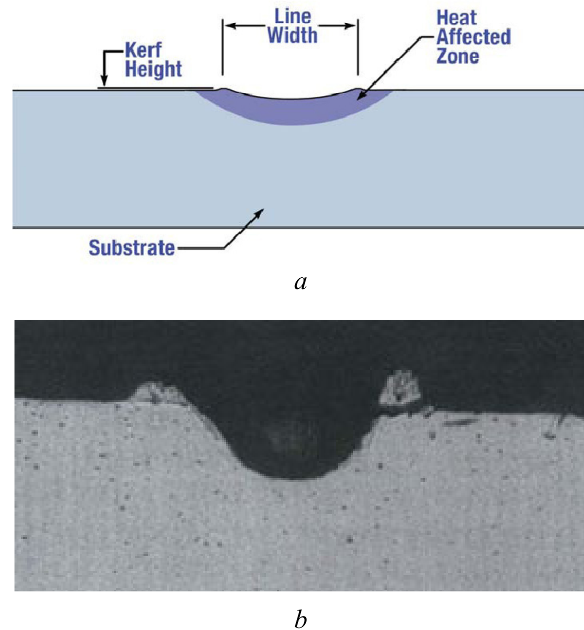

a

b

Fig. 4 – Transverse view through a (*a*) graphically modeled and (*b*) experimentally obtained vector marked substrate.

Another interesting note is that depth is not necessarily required to have a highly readable mark. In Fig. 5*a*, there is a definite disruption of the substrate and significant material removed to generate a deep mark. This is a very readable mark. In Fig. 5*b*, the depth of the mark is barely measurable within the normal texture of the back of the wafer. Nevertheless, it is also quite readable. It appears that the surface has been just slightly melted, and no significant amount of material removed. The apparent readability is the result of the difference in reflected light between the mark of one texture contrasting with a background of a comparatively rougher texture. This type of mark will be preferred as it does not create either excess debris that can be scattered over the wafer or much of a kerf height that may be chipped off at a later process step causing contamination. There is another reason for the shallow marks: consistently, micro cracking is observed when the depth is too high.

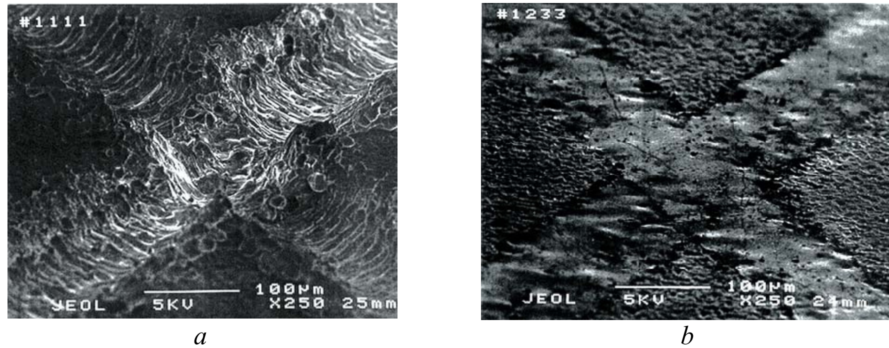

a *b*

Fig. 5 – Deep (*a*) and shallow (*b*) marking.

2.4. Dot Matrix

Dot matrix marking systems create characters by producing small dots in given patterns, in order to generate the required shapes. The beam is scanned over the matrix, and pulsed when a dot is required. The pulse is generated by a rotating polygon mirror, acousto-optical device, or piezoelectric scanning. Dot matrix printing is particularly suitable for producing characters in a well-defined series, such as alphanumeric codes.

2.5. Laser Marking Diagrams

Data for the various mechanisms of modeling can be displayed on the normalized overview chart shown in Fig. 6. The process parameters are normalized with the thermal properties of the materials.

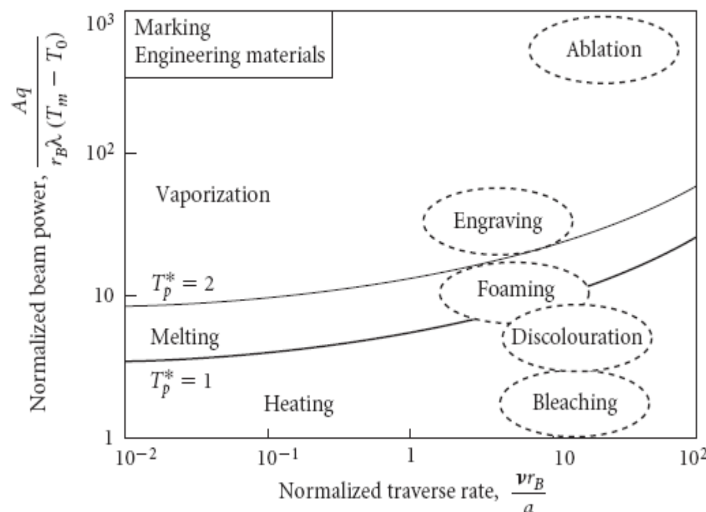

Fig. 6 – Normalized model-based diagram showing contours for the onset of surface melting and vaporization constructed from a surface heat flow model (solid lines); experimental data for various mechanisms of marking cluster into regions bounded by broken lines.

Data for the various thermal marking mechanisms cluster into appropriate regions of Fig. 6 with respect to the normalized surface peak temperature attained. Bleaching data (a photochemical mechanism) fall in regions of low surface temperature rise. The normalized traverse rate of all mechanisms is high – marking is a procedure that is carried out as rapidly as possible.

3. Industrial Application

Marking is now the major laser application in the electronics industries. Wires, substrates, devices, boards, packages and assembled instruments are all laser marked. Parts can be marked with logos and part numbers. Barcodes can be marked onto edge connectors, silicon wafers or boards. Diamond scribing – the previous process – was less flexible and sometimes resulted in wafers breaking. Rapid marking, and soft tooling, which can readily handle ever decreasing package sizes, are the principal attractions of laser marking. Few industrial applications appear in the literature; Table 1 contains a selection from industry sources and Fig. 7 holds a marking station example.

Fig. 7 Laser marking station.

Laser marking has known a broadening interest in the past decade because of its wide use in industrial applications [5]. Direct laser engraving on a surface is a very flexible method that allows permanent marking of information via for instance 2D data matrix codes [6]. A wide range of applications can be addressed, but industrial processes have to pay attention to the influence of the material on which the marking is done. In metals for instance, laser marking may modify the characteristics of the treated surfaces and thus the resistance to corrosion [7]. This property can be of crucial interest in the field of biomaterials to allow the identification of surgical tools as well as prostheses. In this field, marking with ultra fast laser pulses can be interesting despite the still high cost of femtosecond technology [8].

Femtosecond laser marking provides an electrochemical ennoblement. Moreover, the chemical composition is not affected so that the passive character of both stainless steels is maintained, even improved if we consider the susceptibility to localized corrosion [9].

Table 1
Industrial Applications of Laser Marking.

Industry sector	Product	Laser	Material
Aerospace	Control cables	Excimer	Polymer
Automotive	Windscreens	CO_2	Glass
	Vehicle identification numbers	CO_2	Metals
	Dashboard dispays	Nd:YAG	Polymers
	Windscreen edging	CO_2	Glass
Domestic goods	Product information	CO_2	Glass
	Etching	CO_2	Granite plaques
	Packaging	CO_2	Coated paper
Electronics	Tubes and panels	Pulsed CO_2	Glass
	Integrated circuits	CO_2	Semiconductors
	Keyboards	Nd:YAG	Pigmented polymers
Medical	Syringes	Nd:YAG	Polymers
	Containers	Excimer	Glass
Shipbuilding	Identification of sections	CO_2	Structural steel

3.1. Product Identification Codes

Allied Distillers, who manufacture such brands as Beefeater Gin, Ballantines Whisky and Kahlua, have installed a number of pulsed CO_2 laser systems for marking manufacturing information on bottles. Between 30 and 280 bottles are marked per minute, depending on the product and bottle size. Mumm also uses laser marking on its champagne bottles. Clairol (Stamford, CT, USA), a major producer of hair care products, uses pulsed CO_2 lasers to mark painted aluminium tubes and paperboard cartons with product information. Laser marking dispensed with the large inventory of adhesive labels required in the previous process. It was also a superior process to the competing ink jet method. At the Kraft Jacobs Suchard plant in Berlin, dot matrix pulsed CO_2 laser marking is used to code the polyethylene wrappers of chocolate bars at rates of up to 650 per minute.

3.2. Logistic Flows and Lasers

The lasers can be fully integrated into the production line, working 24 hours per day. The levers and thermostatic shower mixer covers come off the automatic chromium plating line in frames, and are then visually inspected and placed into pallets. Each pallet carries a memory chip that stores information on both the product and the pallet [1]. When the laser marking system receives the pallet, it reads the chip and checks the production database for the graphics required for that product. As well as handling all communication with the laser, this customized software then either loads the required graphic or uses a file already held in the laser. The software also controls the position of the laser marks via the pallet positioning system and generates production statistics. The typical

marking time is between 2 and 5 seconds for each item, depending on the product being marked. When the pallet is finished, a robot places the marked products in product-specific transfer boxes for removal to final assembly.

This technological flow belongs to the Finnish appliances manufactured Oras, for whom, since the introduction of laser marking, the use of conventional printing techniques has fallen from 100% to about1% of all marking applications. Only the color-printed levers are still tampo-printed, and that method will be replaced once a laser marking system is implemented (already developed, based on laser melting of certain colored powders or gells directly on the surface of the material, on a give pattern).

3.3. Ornamentation

Laser-based surface ornamentation is actively being developed. Marks are produced by growing discrete oxide layers; the thickness of the oxide layer determines the characteristics of the mark. By controlling the process in g parameters carefully, a variety of colors can be obtained. An Nd:YAG laser and a marking head with galvanometer mirror beam delivery is a suitable system for such an application. A laser is also used to optically transfer two-dimensional images to three-dimensional objects. By defocusing the beam, novel aesthetic effects can be produced. The laser system parameters for marking include pulsing at 5 kHz, a traverse rate of 100mms−1, and a 60% track overlap.

3.4. Barcodes

Printed circuit boards (PCBs) need to be identified by a code that can be read by machines, humans, or both. The reduction in size of electronic technology and the need for marking flexibility offers an excellent opportunity for laser markers.

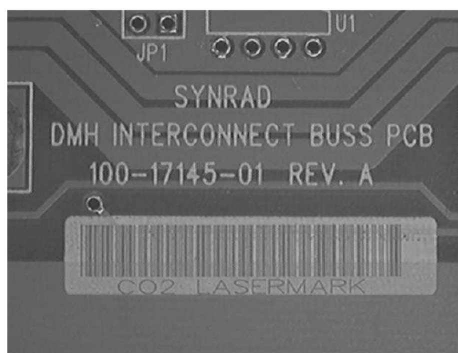

Fig. 8 – Barcode and text market on epoxy ink (ink area 32×6 mm), using a CO_2 laser with 9Wat 1.27ms−1 and a spot size of 180 microns.

Printed circuit boards are made up from a number of layers, with the central copper layer defining the boards’ conducting paths. When marking the board, this layer must not be exposed, otherwise board integrity is lost. Since this

covering layer is only tenths of millimeters in thickness, controlling input energy and thus mark penetration is critical. The contrast available by direct writing onto the board is relatively low, therefore inks are used to enhance the contrast of the marked barcodes. These inks are typically white or yellow. The laser may completely remove or darken the ink to provide contrast, as shown in Fig. 8.

3.5. Data Matrix Codes

Laser dot matrix marking combines the reliability of lasers with the flexibility of dot matrix markers. The process is cost effective and maintenance free. Like ink jet systems, it relies on product motion to provide one axis of mark positioning, with the pulsed laser being scanned vertically to produce a column of dots. Masks are not needed for imaging code information. Multiple lines of marked information can be produced. Direct marking on to PCBs is considerably more convenient, and with the introduction of the data matrix (DM) code, this is possible.

There are two differences between barcodes and data matrix codes: within the second, the information is coded redundantly eight times, so dirt and scratching do not affect the optical reading, as in the case of barcodes, when a simple line can completely cancel this possibility. The second difference refers to the level of contrast required for reading. Barcodes require at least 80% contrast, hence the need for ink, whereas the level of contrast can be as low as 20% with data matrix codes. In addition, an order of magnitude reduction in the space and marking time of the DM code can be achieved in comparison with the barcode. In the direct marking process the laser effectively thermally bleaches the surface of the board, with negligible material removal, as in Fig. 9.

Fig. 9 – 2mm square data matrix code containing 26 alphanumeric characters directly marked onto a printed circuit board marked with a 5W CO_2 laser beam and a 115 micrometer spot size, $0.38 ms^{-1}$.

3.6. 3D Data Matrix Codes

An interesting concept is to use the depth of a marked surface as a third data storage axis. The idea is to convert a performed depth in a gray level in the reading procedure. The exact relation between the obtained depth by laser ablation and the read gray level has to be carefully established. The marking

depth can be then used as a mean for coding. Ultra fast pulses are used since it has been previously established that a precise ablation can be performed using these pulses, with a depth precision of some hundred of nanometers [8]. Ultra short pulses are also known to ablate every kind of materials and are thus well adapted for a first work on both metals and dielectrics.

The laser system was a Ti:Sa laser chain which delivers 150 fs pulses at a repetition rate of 5 kHz. The overlapping of two marking lines was fixed to 10 μm.

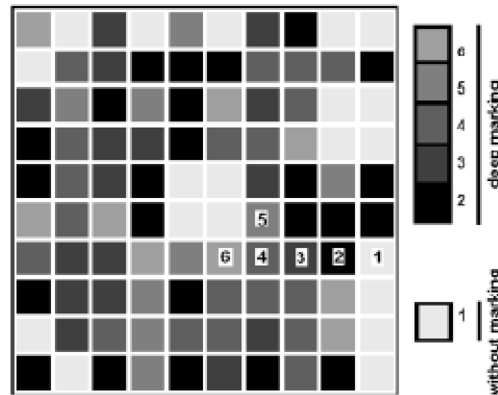

Fig. 10 – Test matrix with six levels of depth.

The basic step of deep marking (corresponding to a precise depth for each material) corresponds to four laser passes (one horizontal, one vertical and two crossed diagonal pass). This ensures a relatively smooth surface. To test the reading method, square features (0.5mm × 0.5mm) are performed at several depths, *i.e.* repeating several times the basic laser processing defined above. Six levels of depth are then chosen and a test matrix is defined (Fig. 10), to be marked on several materials like polymers and metals. Two types of reading procedures have been considered: image acquisition by transmission or reflection (Fig. 11).

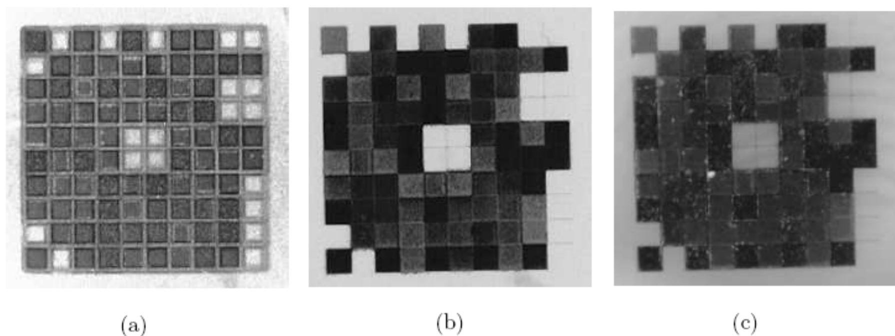

Fig. 11 – Deep marking on metal (stainless steel) with lightening by reflexion (*a*), on polymer lightening by transmission (*b*), on polymer with lightening by reflexion (*c*).

In Fig. 12, the 3D representation of the test matrix is presented, by means of optical techniques. The measurement allow for a precise depth calculation for each square composing the matrix and its correlation to the grey levels of the image, stored via the image acquisition devices. From this point, according to the gained data, one cam modulates the in-depth marking process so that the constructed matrix offers a top level of quality.

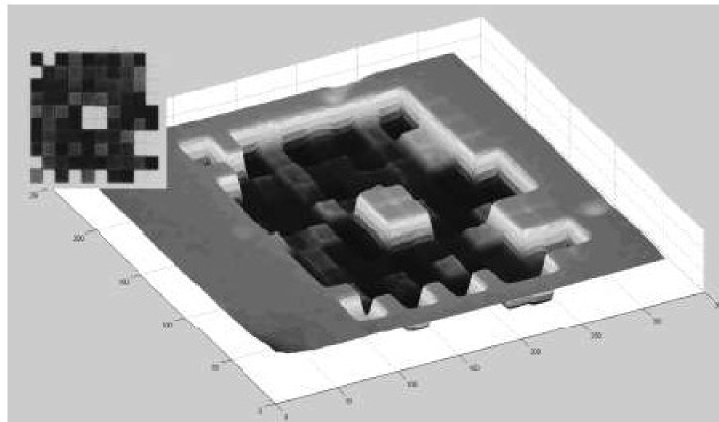

Fig. 12 – 3D representation of 3-dimensional Data Matrix.

4. Summary and Conclusions

Few materials cannot be laser marked [10]. The CO_2 laser is generally the more appropriate source for organic materials, the Nd:YAG laser produces better results with metals and alloys, and excimer lasers are used when high precision micromarking is required. Materials can be modified, e.g. by adding fillers that absorb light, to overcome problems of transparency that hinder marking. The lasers themselves may be modified to be more suitable for various classes of engineering material; the frequency of the Nd:YAG laser can be multiplied to improve its absorptivity, or the pulse energy increased through the use of Q-switching. The ability to make such modifications to materials and lasers will ensure that laser marking remains a competitive manufacturing technique, with a continuous and rapid evolution.

A c k n o w l e d g e m e n t. This paper was realized with the support of EURODOC "Doctoral Scholarships for research performance at European level" Project, financed by the European Social Found and Romanian Government.

Received: August 31st, 2010

"Gheorghe Asachi" Technical University of Iaşi,
Faculty of Material Science and Engineering
e-mail: rusu.st@gmail.com

R E F E R E N C E S

1. ten Hompel M., T. Schmidt, W*arehouse Management–Automation and Organisation of Warehouse and Order Picking Systems*. Springer, 179-220, 221-281 (2007).
2. * * * *Laser Marking Mechanism and Quality Characteristics*. Sintec Optronics Pte Ltd, 2010.
3. Gu B., Schramm R., Gillespie J., Mezack G., Cunningham A., *Laser Wafer Marking at Die Level*. GSI Lumonics, 2003.
4. Ion J.C., *Laser Processing of Engineering Materials*. Elsevier Butterworth-Heinemann, 2005.
5. Kannatey-Asibu E. Jr., *Principles of Laser Materials Processing*. John Wiley & Sons, Inc. (2009).
6. Dusser B., Sagan Z., Bruneel D., Jourlin M., Audouard E., *Laser Deep Marking of Metals and Polymers: Potential Interest for Information Coding*. IOP Publ. Ltd, 2007.
7. Dowden J. (Ed.), *The Theory of Laser Materials Processing*. Springer Sci., Business Media B.V., 2009.
8. Diels J.C., Rudolph W., *Ultrashort Laser Pulse Phenomena - Fundamentals, Techniques, and Applications on a Femtosecond Time Scale*. Elsevier, 2006.
9. *Laser-Surface Interactions for New Materials Production*. Springer Series in Mater. Sci. (2009).
10. Ready J.F., *Industrial Applications of Lasers*. Acad. Press, 1997.

MARCAREA LASER A MATERIALELOR
II. Tehnologii şi aplicatii

(Rezumat)

Marcarea laser directă pe o suprafaţă reprezintă o metodă foarte flexibilă ce permite realizarea de marcaje permanente, ce conţin informaţii de trasabilitate şi identificare, precum codurile 2D tip Data Matrix. Prin urmare, pot fi accesate direct şi efficient o multitudine de aplicaţii. Prezenta lucrare conţine o analiză completă a tehnologiilor şi aplicaţiilor corespunzătoare marcării cu laser.

BULETINUL INSTITUTULUI POLITEHNIC DIN IAŞI
Publicat de
Universitatea Tehnică „Gheorghe Asachi” din Iaşi
Tomul LVI (LX), Fasc. 4, 2010
Secţia
ŞTIINŢA ŞI INGINERIA MATERIALELOR

NEW PHOSPHATED LAYERS ON IRON SUPPORT WITH LUBRICANT PROPERTIES

BY

ANDREI VICTOR SANDU and COSTICĂ BEJINARIU

Abstract. The paper presents the obtaining by precipitation and the lubricant properties of phosphated thin layers. These layers offer a good prelucrability and anticorrosion protection. In order to determine the lubricant properties the behaviour of the phosphated layers was studied through the measurement of drawing force.

Key words: phosphatation, lubricant, iron support, drawing force.

1. Introduction

The known anticorrosion procedures of iron object surfaces by chemical phosphatation consist in precipitation in thin, continuous and uniform layer of some low soluble pyrophosphate, as Zn(II), Ni(II), Mn(II), Ca(II) and very rare Fe(II). More often is used zinc, singular or in mixture with the presented metals. These are applied after grease and oxides removal [1], [2].

The paper presents the lubricant properties of steel samples superficial phosphated by precipitation. The behaviour of the phosphated layers was studied. Through the determination of the necessary force of the drawing for non-treated sample compared with the treated ones.

2. Experimental part

2.1. The Obtaining of the Phosphated Layers

The microcrystalline phosphatation of iron objects [3],...,[8], by chemical passivation of the surfaces is made in order to obtain thin superficial

layers with high porosity, with multiple action of improvement of processing characteristics and corrosion protection. This layer is adherent to the metallic surfaces. After grease and oxides removal it is applied a chemical treatment in two steps:

- first it is deposed a thin layer, with high porosity, made of copper obtained by cementation or nickel by electrodeposition:

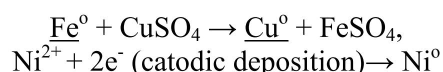

$$\underline{Fe^{o}} + CuSO_4 \rightarrow \underline{Cu^{o}} + FeSO_4,$$
$$Ni^{2+} + 2e^{-} \text{ (catodic deposition)} \rightarrow \underline{Ni^{o}}$$

- second is the copper pyrophosphate precipitation, respectively of nickel, by immersion in two acid aqueous solutions, one low oxidizing of phosphate and cations of Zn^{2+}, in presence of permanganate anion, as surface moderator and other solution based on orthophosphoric acid with Zn powder, at room temperature on the cleaned surfaces.

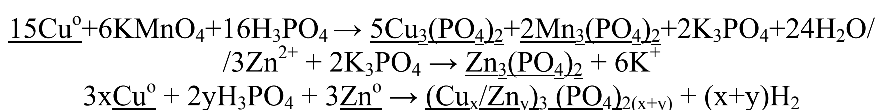

$$\underline{15Cu^{o}}+6KMnO_4+16H_3PO_4 \rightarrow \underline{5Cu_3(PO_4)_2}+\underline{2Mn_3(PO_4)_2}+2K_3PO_4+24H_2O/$$
$$/3Zn^{2+} + 2K_3PO_4 \rightarrow \underline{Zn_3(PO_4)_2} + 6K^{+}$$
$$3x\underline{Cu^{o}} + 2yH_3PO_4 + 3\underline{Zn^{o}} \rightarrow \underline{(Cu_x/Zn_y)_3\,(PO_4)_{2(x+y)}} + (x+y)H_2$$

2.2. The Drawing Force Determination System

In order to determine the drawing force we used an dinamic aquisition system, composed of a master unit, force and movement transducers (Fig. 1). The master unit is a Traveller 1 system, model MUT-1 type 1016-S.

Fig. 1 – The data acquisition system with the PHC 20 Hydraulic Press.

3. Results and Discussions

The equipment presented in Fig. 1 allows the acquisition of the data provided by the force and movement transducers with the help of the E.S.A.M. (Electronic Signal Acquisition Module) software. The aquisition rate is 1000/second.

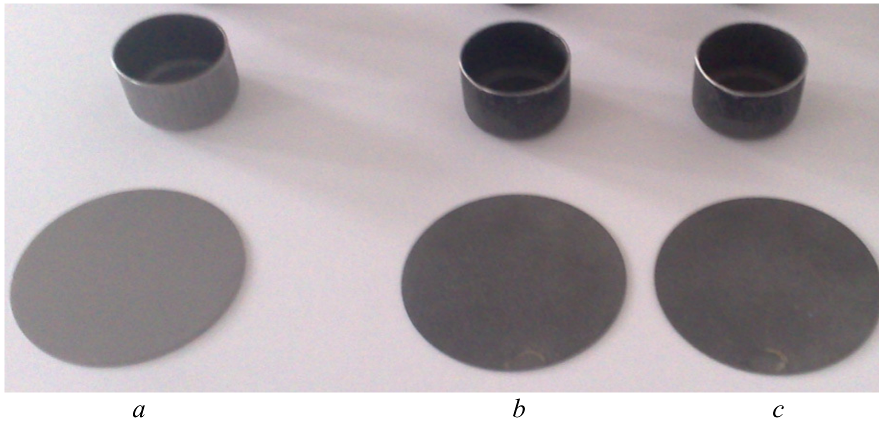

a *b* *c*

Fig. 2 – The samples, initial and after drawing:
a – non-treated samples; *b* – additive/substractive system with zinc cations;
c - additive/substractive system with metallic zinc.

The dependence of the drawing force of the non-treated samples is presented in Fig. 3.

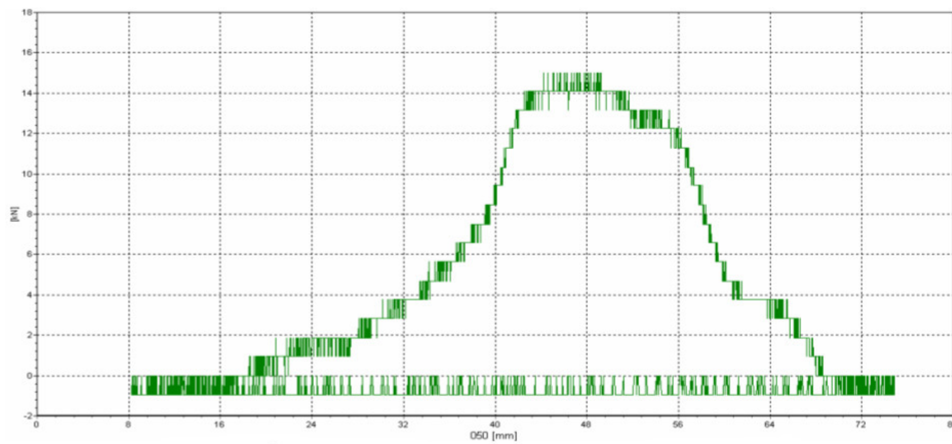

Fig. 3. The drawing force according to the movement of the non-treated samples.

In Figs. 4 and 5 are presented the dependence of the drawing force according to the movement of die for the sample phosphated in aditive/substractive system with zinc cations, and respectively with metallic zinc.

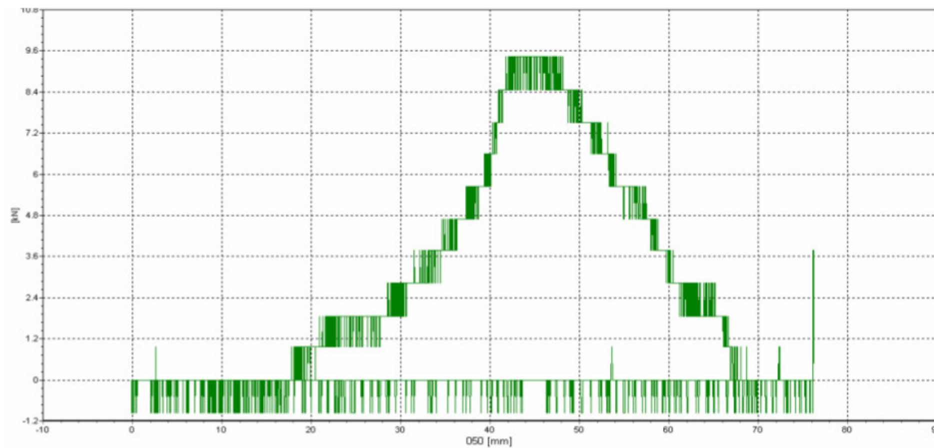

Fig. 4 – The drawing force according to the movement of the phosphated samples through the additive/substractive system with zinc cations.

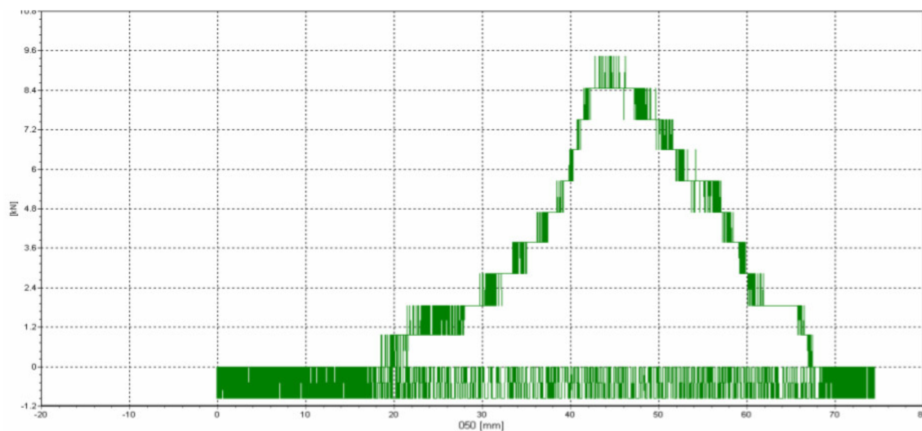

Fig. 5 – The drawing force according to the movement of the phosphated samples through the additive/substractive system with metallic zinc.

4. Conclusion

The involvement of the chemical phosphatation processes allows the obtaining of superficial layers with multiple action, lubricant and anticorrosion

in the case of plastic volume and surface deformation.

The phosphatation allows obtaining of continuous, adherent to substrate layers with controlled physical-structural and chemical properties. The treated samples can be easier plastically processed at low temperatures.

It is obvious that the drawing force in the case of phosphated samples decreases with 35% compared to the non-treated samples (the force decreases from ≈14 kN to ≈9 kN).

A c k n o w l e d g e m e n t. This paper was realized with the support of EURODOC "Doctoral Scholarships for research performance at European level" Project, financed by the European Social Found and Romanian Government.

Received: August 25, 2010

"Gheorghe Asachi Technical University" of Iaşi,
Faculty of Material Science and Engineering
e-mail: andrew_viktor@yahoo.com

R E F E R E N C E S

1. Marinescu A., Andonianț Gh., Bay E., *Tehnologii electrochimice şi chimice de protecție a materialelor metalice*. Edit. Tehnică, Bucureşti, 1984.
2. Oniciu L., Grüwald E., *Galvanotehnica*. Edit. Şt. şi Enciclop., Bucureşti, 1980.
3. Sandu I.G., Dima A., Sandu I., Roibu L., Sandu I.C.A., Roibu L.O., Sandu A.V., *Process for Obtaining Artistic Patina by Chemical Passivation of Iron Parts Surfaces*. Brevet *RO122303*/30.03.2009.
4. Bejinariu C., Sandu I., Predescu C., Vasilache V., Munteanu C., Sandu A.V., Vasilache V., Sandu I.G., *Procedeu de fosfatare microcristalină a pieselor metalice pe bază de fier.* Dosar OSIM *A/01022*/29.12.2008.
5. Bejinariu C., Sandu I., Predescu A., Sandu I.G., Baciu C., Sandu A.V., *New Mechanisms for Phosphatation of Iron Objects*. Bul. Inst. Politehnic, Iaşi, **LV(LIX)**, *1*, s. Ştiința şi Ingineria Materialelor, 73-76 (2009).
6. Bejinariu C. Sandu I.,Vasilache V., Sandu I.G, Bejinariu M.G., Sandu A.V., Sohaciu M., Vasilache V., *Procedeu de fosfatare cristalină lubrifiantă a pieselor metalice pe bază de fier*. Dosar OSIM *A/01023*/29.12.2008.
7. Bejinariu C., Sandu A.V., Ionita I., Sandu I., Vasilache V., Sandu I.G., *New Procedures for Lubricant Phosphatation*. Edit. Univ. „Dunărea de Jos", Galați Univ. Press, Lucr. Conf. Internat. UGALMAT 2009, 321-324.
8. Bejinariu C., Sandu I., Predescu A., Sandu I.G., Baciu C., Sandu A.V., *New Mechanisms for Phosphatation of Iron Objects*. Bul. Inst. Politehnic, Iaşi, s. Ştiința şi Ingineria Materialelor, **LV(LIX)**, *1*, 73 – 77 (2009).
9. Sandu A.V., Bejinariu C., *Obtaining and Characterization of Superficial Phosphated Layers on Iron Support*. Bul. Inst. Politehnic, Iaşi, s. Ştiința şi Ingineria Materialelor, **LVI (LX)**, *2*, 113-116 (2010).

NOI STRATURI FOSFATATE PE SUPORT DE FIER
CU PROPRIETĂȚI LUBRIFIANTE

(Rezumat)

Lucrarea prezintă obținerea prin precipitare şi proprietățile lubrifiante a straturilor superficiale fosfatate. Aceste straturi ofera o bună prelucrabilitate şi protecție anticoroziv. Pentru a determina proprietățile lubrifiante a fost studiată comportarea straturilor prin determinarea forței de ambutisare.